

Alma Mater Studiorum – Università di Bologna

DOTTORATO DI RICERCA IN
INGEGNERIA ELETTRONICA, TELECOMUNICAZIONI E
TECNOLOGIE DELL'INFORMAZIONE

Ciclo XXXII

Settore Concorsuale: 09/F1

Settore Scientifico Disciplinare: ING-INF/02

TERAHERTZ AND MILLIMETRIC RECTENNAS

Presentata da: Mazen Al Shanawani

Coordinatore Dottorato

Prof.ssa. Ing. Alessandra Costanzo

Supervisore

Prof. Ing. Diego Masotti

Esame finale anno 2020

ALMA MATER STUDIORUM
UNIVERSITÀ DI BOLOGNA

TERAHERTZ AND MILLIMETRIC
RECTENNAS

MAZEN SHANAWANI

*A thesis submitted in fulfillment of the requirements
for the degree of Doctor of Philosophy*

CICLO. XXXII

SETTORE CONCORSUALE DI AFFERENZA: 09/F1

SETTORE SCIENTIFICO DISCIPLINARE: ING-INF/02

Programme Coordinator:

PROF. ENG. ALESSANDRA COSTANZO

Supervisor:

PROF. ENG. DIEGO MASOTTI

FEBRUARY 15, 2020

Declaration of Authorship

I, Mazen Shanawani, declare that this thesis titled, “Terahertz and Millimetric Rectennas” and the work presented in it is my own. I confirm that:

- This work was done wholly or mainly while in candidature for a research degree at this University.
- Where any part of this thesis has previously been submitted for a degree or any other qualification at this University or any other institution, this has been clearly stated.
- Where I have consulted the published work of others, this is always clearly attributed.
- Where I have quoted from the work of others, the source is always given. With the exception of such quotations, this thesis is entirely my own work.
- I have acknowledged all main sources of help.
- Where the thesis is based on work done by myself jointly with others, I have made clear exactly what was done by others and what I have contributed myself.

Signed:

Date:

Licence Notice

The thesis text has been written using a L^AT_EX template downloaded from <https://www.latextemplates.com/template/masters-doctoral-thesis> by Vel and Johannes Böttcher. The template is licensed under **CC BY-NC-SA 3.0**.

According to this license **it is allowed to**:

- Share, copy and redistribute the material in any medium or format.
- Adapt, remix, transform, and build upon the material for any purpose.

However, it is **not allowed to** reuse the template for commercial purposes.

I, Mazen Shanawani, declare that the aforementioned template is not used for commercial purposes and is *only* used for the sake of writing the doctoral thesis.

I, further, declare that there has been some modifications both on the `main.tex` and `MastersDoctoralThesis.cls` files in order to add some further functionalities and change the text color in accordance with the rights granted under the **CC BY-NC-SA 3.0** license.

The L^AT_EX code used to produce this work is licensed under Creative Commons Attribution-NonCommercial-ShareAlike 4.0 International license.



*For my daughter Zeina,
and the memory of my father Mansour...*

“Avoid the unhappy and unlucky.”

Robert Greene, *“The 48 Laws of POWER”*

Abstract

This thesis represents the results of the research activity that took place at the University of Bologna within the 32nd Ph.D program cycle in Electronics, Telecommunications and Information Technologies Engineering at the University of Bologna, Italy. The work regarding the tunnelling diode optimisation has recently won the ENABLES project support to produce a diode based on the output of the optimization process presented in this work.

In recent years, the energy market has witnessed increasing demand on green energy resources to meet the increasing requirements of modern lifestyle without increasing reliance on oil reserves. In addition to this, the blooming battery-less distributed sensor applications are becoming a driving force in the market to invent energy harvesting power supplies. Out of the available energy sources, the electromagnetic energy is drawing more attention thanks to the ease of integration with subsequent circuitry and the available frequency range that extends into the terahertz band.

While energy harvesting in the lower gigahertz band has witnessed many improvements leading to market-ready solutions, the terahertz harvesting is, still, in an immature state.

The electromagnetic energy harvesting problem can be regarded as an optimisation issue, and hence optimising all of the receiver, the propagation medium, and the transmitter will lead to an efficient harvesting system. In this thesis, the reason why it is beneficial to categorise rectifiers based on their operation frequency will be explained. As will be demonstrated later, the electromagnetic radiation frequency identifies the theory of operation and so the rectifiers are categorised, frequency-wise, into lower and upper frequency bands.

While the theoretical framework for the lower frequency band rectifiers is more "uniform" with wide consensus on semiconductor physics and Maxwell's equations, there is a multitude of theories to explain the rectifier operation for upper frequency bands. For the latter case, Simmons and the transfer matrix method models are chosen and elaborated in more details. An optimisation framework that deploys the transfer matrix method to calculate the voltage-current relationship of a tunnelling diode and improve the relevant figures of merit will be also suggested.

Similarly, new and novel techniques that lead to optimized wireless energy transmission will be elaborated. In this context, the time-modulated array technique will be considered and studied, for a range of frequencies extending to 28 GHz, as a possible substitution to the linear phased array control circuits already known for their high losses. The novel frequency-diverse array technique, leading to distance-dependent radiation pattern behaviour, will be also discovered. In the end, an account of the strengths and weaknesses of both approaches will be presented.

In the end, a market-ready solution for an *efficient* energy-harvesting device working in the 2.4 GHz band is presented and tailored to work with battery-less and wireless networking terminals in harsh electromagnetic environments. Starting from a simple and generic rectifier model, the design is upgraded to reach an end-product prototype together with its measurements in a real world scenario.

To, further, provide a market-ready design suite for near-future energy harvester, an efficient and fast simulation method capable to calculate the received power by wireless sensors is also presented. Thanks to the integral solver simulation, the results are more accurate than typical finite difference simulation and are obtained much faster as demonstrated in the corresponding chapter.

Acknowledgements

It is really difficult to acknowledge all the people who have helped me out during such an eventful experience within few lines. Therefore, I apologize to everybody worth the acknowledgment that has not been mentioned here.

Firstly, all the current work, entire scholarship, and my living experience would not reach a good end without the fatherly support of my supervisors Prof. Diego Masotti, and Prof. Alessandra Costanzo to whom I owe a lot for all the types of academic, practical and spiritual support they have offered. I Would like also to send many thanks to our colleague Dr. Martino Aldrigo for all the insightful, and useful discussions we have had for many shared work.

I am puzzled how to thank my office colleagues for not just offering academic help, but for being also an extended family sharing food, and many extracurricular activities. You have been great both as family members and academic support!

Special and distinct thanks go the Institute of Advanced Studies (ISA) of the University of Bologna and its staff represented by its Director Prof. Dario Braga for the invaluable help and support presented during the course of study. Their aid has granted me many privileges over other Ph.D colleagues.

The contribution of Dr. Mohammed Khaled Chahine is unforgettable as he has been my motivation to apply to the PhD scholarship programme at the University of Bologna. Equal special thanks go to all Arab International University (AIU) directors, and teaching board for supporting my decision for the scholarship.

I shall not forget the contribution of my wife Nour Alshamas during this demanding period whose unrivaled presence has, and would continue to impact my academic and future career. Words can hardly express my gratitude to my mother Qamar Albahra for being an invaluable and great support and

having the strength to accept my travel to another country for my Ph.D studies. Also, many special thanks go to Eng. Jacopo Aslo for helping me out during the settlement in Bologna and the cozy and generous support he has always offered.

In the end, I wish to dedicate this work to my father Mansour who has been my inspiration and who died earlier before my Ph.D studies. In remembrance of the profound effect he has had and will continue to have on my life and development.

Contents

Declaration of Authorship	iii
Licence Notice	iv
Abstract	ix
Acknowledgements	xi
Acronyms	xxv
1 Introduction	1
1.1 Overview	1
1.2 Historical Notes	3
1.2.1 Energy Harvesting from Natural Sources	3
1.2.2 Systematic Wireless Power Transfer	5
1.3 Motivation of Work	6
1.4 Thesis Outline	8
2 Receiving Part	11
2.1 Preface	12
2.1.1 Nonlinearity Depolyment	12
2.1.2 Basics of Tunnelling	15
2.2 Rectifier Design	21
2.2.1 Design for Lower Frequencies	21
2.2.2 Design for Higher Frequencies	23
THz Radiation Characteristics	24

	Overview of Charge Carrier Models	28
	Rectenna Under Illumination	35
2.3	Simmons Model	40
2.3.1	Overview	40
2.3.2	Potential Barrier Formula	40
2.3.3	Tunnelling Current	42
2.3.4	Modelled Circuit And Results Discussion	46
2.4	Transfer matrix method	50
2.4.1	Overview	50
2.4.2	Transmission Matrix Formalism	52
2.4.3	Current Density Calculation	55
2.4.4	Transmission Probability Calculation Using Fixed Step	57
2.4.5	Transmission Probability Calculation Using Adaptive Step	60
2.5	Structure Optimization	62
2.5.1	Overview	62
2.5.2	System Description	64
2.5.3	Simulation Results	66
	Input Parameters	66
2.5.4	Results	68
2.6	Conclusion	72
3	Transmitting Part	77
3.1	Preface	77
3.2	RF Link Power Losses	78
3.3	Time-modulated Arrays	81
3.3.1	Mathematical Formalism	81
3.3.2	Co-Simulation of Time Modulated Array. (TMA)	84
3.3.3	Millimetre Wave Agile TMA System	87

	The Nonlinear Diode Device	88
	16-Element Array for TMA	90
	Nonlinear/EM Co-Simulation Results	92
3.4	Frequency-diverse Arrays	95
3.4.1	Mathematical Concept	95
3.4.2	Co-Simulation of Frequency-diverse Arrays (FDA)	100
	Harmonics Generation	100
	Far Field Database Organization	101
	Simulation Procedure	101
3.4.3	Results	103
3.5	Conclusion	106
4	Low Frequency Energy Harvester Design	109
4.1	Introduction	109
4.2	Nonlinear Device Choice	111
4.3	Initial Prototype Model	114
4.4	Matching Circuit Design	115
4.5	Efficiency Equation And Calculation	117
4.6	Circuit Optimisation And Realisation	120
4.7	Measurements and Results	124
4.7.1	Free Space Loss (FSL) Calculation And Link Budget	125
4.7.2	Rectifier Measurement Settings And Results	126
4.8	Conclusion	128
5	Efficient Wireless Power Transfer (WPT) Simulation	131
5.1	Preface	131
5.2	Introduction	131
5.3	Theoretical Background	134
5.4	Simulated Prototype	136
5.4.1	Model Description	136

5.4.2	Simulation Results	139
5.5	Measurements	140
5.6	Conclusion	142
6	Conculsion	145
A	Source Codes	149
A.1	MATLAB Codes	149
	Bibliography	155

List of Figures

1.1	Conceptual diagram of an energy harvesting system.	1
1.2	Generic circuit diagram for a rectenna system. (Developed from [12].)	4
1.3	Chronological evolution of rectennas' frequencies and the corresponding efficiency. Colour of circles correspond to efficiency η based on the colour bar, numbers in brackets correspond to references in the bibliography. M refers to measured results, and ? means that the reference does not say.	7
2.1	Comparison between original, 2 nd order, and 4 th order Taylor expansion values (a), and their corresponding error value ϵ from the original function (b).	13
2.2	An electron having energy E moving in the $+x$ direction towards a barrier formed by the difference between the corresponding metal work function Ψ_{met} , and the insulator affinity function χ_{ins}	16
2.3	Real and imaginary wave function $\psi(x)$ components (a), and the corresponding probability $p(x)$ (b). In both figures the rectangular barrier is shown.	18
2.4	Probability function $p(x)$ with respect to x (a), and the transmission coefficient T value with respect to total energy E (b).	20

2.5	Common rectifier schematics for low-frequency energy harvesting. (a) Single-diode rectifier, and (b) Two-diode rectifier.	22
2.6	Black body radiation law curves for different temperatures.	25
2.7	EMCF function curve for the quasi monochromatic light for wavelengths $\lambda = 1.3 \mu\text{m}$, $0.9 \mu\text{m}$, $0.5 \mu\text{m}$ and for solar black body radiation. (Reprinted by permission from Springer Nature: [61].)	28
2.8	Categorisation of theory of operation	30
2.9	Energy band diagram of a metal-insulator-metal MIM tunnelling diode. (Reprinted by permission from Elsevier: [37].)	31
2.10	Schematic representation of the ballistic rectifier. (Reprinted by permission from IOP Publishing: [78].)	32
2.11	Impact of changing the oscillation (illuminating wave) frequency on tunnelling current (a). Impact of changing the oscillation amplitude V_ω on the tunnelling current (b).	39
2.12	Potential barrier for a Nb/Nb ₂ O ₅ /Au structure with $L = 5 \text{ nm}$ insulator thickness assuming different image forces values.	42
2.13	The $I(V)$ relation according to Simmons model using the parameters shown in Table 2.1. A rapid current discontinuity occurs as shown.	45
2.14	The THz rectifier equivalent circuit	46
2.15	The dynamic resistance of the modelled diode.	49
2.16	Continuous, discrete constant, and discrete linear potential barrier profile for the Nb/Nb ₂ O ₅ /Au diode example demonstrated in section 2.3.	51
2.17	laminated insulators with different dielectric constants. The potential difference on the structure is subject to the displacement conservation vector \mathbf{D}	56

2.18	Energy diagram, potential profile, image forces lowering, and the total potential for a Al/NbO ₅ /Al ₂ O ₃ /Al metal-insulator-insulator-metal (MIIM) diode.	59
2.19	Tunnelling probability for a Al/Nb ₂ O ₅ /Al ₂ O ₃ /Al MIIM diode for E_x level ranging from 12 eV to 15 eV.	60
2.20	Potential profile, for an adaptive mesh simulation system for a Al/NbO ₅ /Al ₂ O ₃ /Al MIIM diode.	61
2.21	Tunnelling probability for a Al/Nb ₂ O ₅ /Al ₂ O ₃ /Al MIIM diode for E_x level ranging from 12 eV to 15 eV using adaptive steps for both the energy level and the potential profile.	62
2.22	Schematic diagram of the optimization program used.	64
2.23	$J(V)$ response of a Nb/Nb ₂ O ₅ /NbN single insulator diode as explained in Scenario 1. Restored curves are reproduced from [37] while the simulated results are the output of the optimization process.	69
2.24	Responsivity γ and nonlinearity χ Figure of Merit (FOM)s response of a Nb/Nb ₂ O ₅ /NbN single insulator diode as explained in Scenario 1. Restored γ and χ curves are reproduced from [37] while the simulated results are the output of the optimization process.	70
2.25	$J(V)$ response of a double insulator diode as explained in Scenario 2. Continuous curves are $J(V)$ curves of the restored results of [102]. The inset figure shows the solid and dashed curves of the restored response for responsivity γ and nonlinearity χ , respectively.	70
2.26	Responsivity γ and nonlinearity χ FOMs response of a Nb/Nb ₂ O ₅ /NbN single insulator diode as explained in Scenario 1. Restored γ and χ curves are reproduced from [37] while the simulated results are the output of the optimization process.	71

3.1	Details of the wireless link with the involved power contributions.(Reprinted by permission from John Wiley & Sons: [107].)	79
3.2	Schematic representation of a linear n_A element TMA. [109]©[2018] IEEE	81
3.3	Frequency-dependent radiation pattern with harmonics $f_0 \pm hf_M$ for a 16-element linear TMA [112] © [2016] IEEE.	84
3.4	A system made of linear elements (shadowed in grey and yellow) and nonlinear diodes (shadowed in green)[110]©[2013] IEEE.	85
3.5	Examples of periodical switches excitation sequences (in blue), modulating the RF carrier waveforms (in gray), for three different switching patterns [112].	86
3.6	Schematic cross-section of the proposed Nb/Nb ₂ O ₅ /Pt metal-insulator-metal (MIM) diode and its integration with the transmission line.	89
3.7	Electromagnetic (EM) design of the 28 GHz single monopole as array element for the proposed TMA. In the inset, a cross-section of the structure is provided [109] © [2018] IEEE.	89
3.8	Simulated input impedance of the 28 GHz single monopole.	90
3.9	Radiation pattern of the excited array by excitation of the two central elements.	91
3.10	Radiation pattern of the proposed array by the excitation sequence shown in [116]© [2011] IEEE.	92
3.11	Current waveforms for ideal switches, and simulated nonlinear switches.	94
3.12	Schematic of a FDA antenna array system with respective elements, and variables.	95
3.13	Suggested schematic for FDA system signal generation.	96

3.14	Three Dimensional (3D) plot of the FDA array factor (AF) response as a function of azimuthal angle θ and distance r	97
3.15	The FDA array factor for $\Delta f = 1$ MHz, 5 MHz and 10 MHz . . .	99
3.16	Geometric structure of the FDA array element spacing and a snapshot of the entire array[120]© [2019] IEEE.	103
3.17	Simulation results for $\Delta f = 5$ MHz, and $P_{av} = 10$ dBm.	104
3.18	Simulation results for $\Delta f = 10$ MHz, and $P_{av} = 15$ dBm	104
3.19	Simulation results for $\Delta f = 10$ MHz, and $P_{av} = 10$ dBm	105
4.1	Conceptual design of the energy harvesting wireless solution.	110
4.2	The adopted Schottky diode model with the parasitic components.	111
4.3	The responsivity f_{RES} , and dynamic resistance R_D FOM curves for the HSMS-7630 diode.	112
4.4	The responsivity f_{RES} , and dynamic resistance R_D FOM curves for the HSMS-7630 diode.	112
4.5	A single diode rectifier model to measure its performance. . .	113
4.6	Schematic model of the simulated rectifier circuit using ADS. .	115
4.7	Spectral analysis of the input voltage v_{in} and current i_{in} signals of the initial rectifier design.	116
4.8	Rectifier matching circuit schematic and the corresponding S Parameters response.	117
4.9	Real antenna equivalent circuit where the available power, together with the antenna internal impedance forms a whole block as shown in the dashed grey square.	118
4.10	Photo of the utilized antenna for the harvester.	119
4.11	Magnitude and phase of the measured S Parameters.	120
4.12	Schematic of the optimized circuit using the real components as modelled on ADS®.	122

4.13	Spectral analysis of the v_{in} , and i_{in} signal to the optimised rectifier.	122
4.14	Analysis of the rectifier efficiency across $P_{in} = -20$ dBm to 0 dBm for a range of frequencies from $f = 2.4$ GHz to 2.5 GHz.	123
4.15	Image of the circuit layout and the realised circuit on FR4 board.	124
4.16	Sketch of the calibration and measurement scenario.	124
4.17	Spectrum analyzer reading of the received signal by the dipole antenna.	126
4.18	Rectenna measurement setting.	126
4.19	Efficiency and voltage output comparison as a function of input power between initial, optimized, and measured circuit.	127
5.1	Conceptual comparison between the Finite Difference (FD) and Integral Equation (IE) meshing techniques.	132
5.2	Snapshot of the simulated scenario. The Transmitter (Tx) antenna is shown ahead of the propagation medium. There are two positions for the the receiving antenna points (P1) and (P2). Detailed spacing is shown in Table 5.1	133
5.3	Conceptual representation of the chosen surface Σ , and the theoretical model used.	134
5.4	Snapshot of the patch antenna used for the Tx and Receiver (Rx) antennas, and the corresponding parameters.	137
5.5	Snapshot of the realized testbed.	141
5.6	Comparison of the received power P_{out} between measurements (MEasurements), IE-based model (IE model), and the Time Domain (TD) solver results (TD solver).	142

List of Tables

2.1	Used parameters in Simmons model.	44
2.2	Circuit optimization results using a diode with rescaled R_D and C_j values.	49
2.3	Input parameters used for the potential profile calculation. . .	60
2.4	Input parameters used for the Genetic Algorithm (GA) optimizer.	67
2.5	Targeted FOM and the corresponding weights used for the GA optimizer.	68
2.6	Initial and final states of the GA run for the optimized scenarios.	69
3.1	P_R/P_T in dB for various spaces and frequencies	78
3.2	Design parameters of the circular patch array shown in Figure 3.7.	91
3.3	Azimuth angles corresponding to maximum AF values for $\Delta f = 5$ MHz and 10 MHz.	99
3.4	Contents of the radiation pattern database generated for each $f_n = f_0 + (n - 1)\Delta f$ and for each array element.	101
3.5	Comparison between co-simulation, and modelling values of the azimuth angles θ corresponding to maximum AF.	105
4.1	Chosen simulation configuration, component values, and device models for the initial circuit model.	114
4.2	Real components that replace the ideal ones to be included in the optimisation process.	121

4.3	Initial and final values for the optimised components.	123
4.4	Parameters used to calculate the FSL of the measurement scenario	125
5.1	location of objects and antennas in the simulated scenario, and patch antenna characteristics	138
5.2	Comparison between calculated values by IE and TD methods.	139
5.3	Comparison between simulation time taken by IE and TD methods.	140

Acronyms

1D	One Dimensional
2.5D	Two And A Half D
2DEG	two-dimensional electron gas
3D	Three Dimensional
5G	fifth generation
AF	array factor
BAN	Body Area Network
CAD	Computer-aided Design
EM	Electromagnetic
EMCF	Equal time Mutual Coherence Function
FD	Finite Difference
FDA	Frequency-diverse Arrays
FET	Field Effect Transistor
FFT	Fast Fourier Transform
FOM	Figure of Merit
FSL	Free Space Loss
GA	Genetic Algorithm
HB	Harmonic Balance
IE	Integral Equation
IF	Intermediate Frequency
IFFT	Inverse Fast Fourier Transform
IoT	Internet of Things
ISM	Industrial, Scientific, and Medical

LCM	Least Common Multiple
LO	Local Oscillator
LoRa	Long Range Wireless
LPF	Low Pass Filter
MFPL	mean-free path length
MIIM	metal-insulator-insulator-metal
MIM	metal-insulator-metal
mm-wave	Millimetre Wave
NEGF	Non Equilibrium Green Function
PAN	Personal Area Network
PAT	Photon Assisted Tunneling
PEC	Perfect Electric Conductor
QTBM	Quantum Tunnelling Boundary Method
RAM	Random Accessible Memory
RT	Resonant Tunneling
Rx	Receiver
SoC	System on Chip
ST	Step Tunneling
TD	Time Domain
TMA	Time Modulated Array.
TMM	Transfer Matrix Method
Tx	Transmitter
VBA	Visual Basic for Applications
WAN	Wide Area Network
WKB	Wentzel, Kramers, and Brillouin
WPT	Wireless Power Transfer

Physical Constants

Speed of light	$c_0 = 2.997\,924\,58 \times 10^8 \text{ m s}^{-1}$
Planck constant	$h = 6.626\,070\,04 \times 10^{-34} \text{ m}^2 \text{ kg s}^{-1}$
Reduced Planck constant	$\hbar = 1.054\,571\,817 \text{ m}^2 \text{ kg s}^{-1}$
Electron charge	$e = 1.602\,176\,62 \times 10^{-19} \text{ C}$
Electron mass	$m = 9.109\,383\,56 \times 10^{-31} \text{ kg}$
Vacuum permittivity	$\epsilon_0 = 8.854\,187\,812\,8 \times 10^{-12} \text{ F m}^{-1}$
Boltzmann constant	$K_B = 1.380\,648\,52 \times 10^{-23} \text{ m}^2 \text{ kgs}^{-2} \text{ K}^{-1}$
Richardson constant	$A^* = 1.201\,73 \times 10^6 \text{ Am}^{-2} \text{ K}^{-2}$

Chapter 1

Introduction

1.1 Overview

In the recent years there has been an increasing demand to reduce the pollution of the environment to meet the stringent measures posed by the governmental bodies throughout the world. In 2020 the cut back on greenhouse gas should be 20% less compared to 1990 levels [1].

At the same time, the growth of the Internet of Things (IoT) has witnessed unrivalled rates as the number of devices connected to the internet is expected to go beyond six times as many as the world population [2]. This coincides with the bottleneck experienced by modern computer processors to dissipate the energy resulting from the nano-scale switching circuits [3] and necessitates a less central computation techniques such that more computation at the terminals is preferred.

Consequently, it becomes necessary to look for natural and more efficient

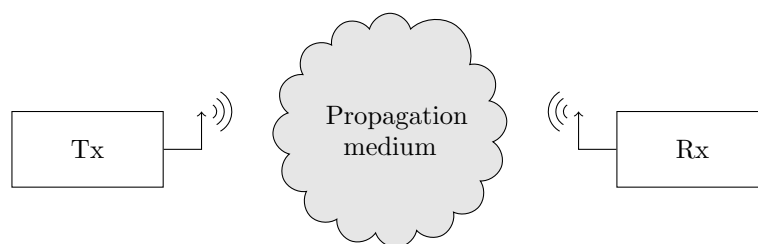


FIGURE 1.1: Conceptual diagram of an energy harvesting system.

energy sources that can stand up to these measures within this relatively limited time. In fact, there has been many trials to deploy mechanical systems such as nonlinear oscillators to harvest energy from natural and random vibrations [4]. These systems managed to reach efficiency levels six times higher than the linear mechanical oscillator systems as in [5]. However, having an electric system completely integrated on the same substrate with other circuits would offer high flexibility both at the transmitter and receiver side as will be explained later. In a generic sense, one may consider the electric energy harvesting system according to the conceptual diagram shown in Figure 1.1 which sets the outline of this thesis:

- The Rx which needs to collect as much RF energy from the ambience as possible and convert it to DC current with minimum losses. From this point on, this system as represented in Figure 1.2, will be referred to by **rectennas** as a shorthand of the words **rectifying antennas**. Figure 1.2 shows the generic diagram of a rectenna system where the signal received by the antenna is directed to the diode for which we deploy its nonlinearity to rectify the AC waveform into a DC signal. The Low Pass Filter (LPF) unit will clearly restrict all components higher than the DC from passing into the load R_L . Thus keeping the AC part separated from the DC one. The letters η_a, η_c, \dots refer to the efficiencies of the respective parts [6].
- The Tx which needs to *intelligently* send the energy such as to minimize the power losses in idle times, and to better shed the RF power in narrower and more defined angles. Therefore, optimizing its transmission time, transmission signals, circuitry, etc.
- The propagation medium which needs to be appropriately modeled. The right modelling choice, as will be explained later in chapter 5, helps to have both shorter simulation times and more accurate results.

The aforementioned categorization, including Figure 1.2, remains valid for all the radio frequencies extending from a few GHz up to the THz range. Having said that, a frequency-based categorization may be beneficial as the circuit topology and signal nature are frequency-dependent [6]:

- Lower frequencies up to tens of GHz in this range the receiver circuitry is more like the classical circuitry using the typical rectification practices such as [7]. The sender is also man made, with highly-controllable radiation characteristics.
- Higher frequencies extending to the THz range. The receiver circuitry deploys semi-classical or completely quantum approach. The sender, on the other hand, is usually a less controllable or a natural source (e.g. sun radiation, hot surfaces, etc.) which follows the black body law.

1.2 Historical Notes

Due to the diverse nature of energy harvesting applications, I will showcase them in a categorized way as follows:

1.2.1 Energy Harvesting from Natural Sources

The idea of harvesting sun or light radiation into electricity is not new, and it may be traced back in time to the nineteenth century in 1839 when Edmond Becquerel [8] noticed the effect of illuminating silver chloride inside an acidic solution which resulted into generating voltage and current. From that point on, many contributions took place to optimise the system paving the way for a more efficient solar cell prototype by Bell Labs in 1954 [9]. Although solar cells mechanism is simple, a critical power efficiency limitation is imposed because the required incident photon energy should be *exactly* equal to

the energy required just to free the electron-hole pair. Otherwise, the wide-band nature of the solar radiation will yield sub optimal efficiencies below the 44% Shockley-Queisser limit [10] calculated for a 1.1 eV energy gap. In practical terms this limitation is considered the major reason [11] as to why single junction solar cells have efficiency figures around 20%. This frequency-dependent behaviour is not only limited to p-n junction solar cells, but also affects the rectennas behaviour in modelled prototypes.

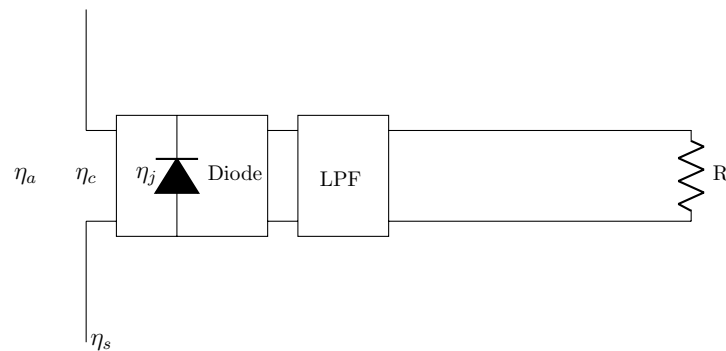


FIGURE 1.2: Generic circuit diagram for a rectenna system. (Developed from [12].)

Notwithstanding all of the aforementioned facts, commercial systems are getting more widespread and some novel designs managed to exceed 20% efficiency [13]. Thanks to multijunction solar cells [14], efficiencies up to 40% may be reachable. Although current commercial systems can reach up to 20% of power efficiency -which is technically a poor figure-, their production costs are still high with the current lowest production cost for a GaAs substrate reaching \$150 for a 6-inch wafer [15]. It should be pointed out, however, that other alternatives, such as perovskite, may replace the typical solar cells with reported efficiencies in excess of 20% and much cheaper production costs [16]. Nevertheless, their lifetime is much shorter than that of their typical counterparts.

The use of rectennas to rectify signals in the THz range dates back to the experiment of Habbal et al. [17] in 1983. A rigorous study of THz signal rectification was conducted by [18] in 1998. The antenna will be responsible to

receive the electromagnetic radiation from the difference between rectennas and p-n junction solar cells lies in the fact that rectennas receive the radiation in its wave form as opposed to solar cells that deploy the quantum nature of light. However, quantum mechanics are frequently deployed in explaining the theory of operation of the rectifying diode as it will become clear later on. Thus, paving the way for what is referred to as *semiclassical* models [19]. In these models, the radiation is perceived as an oscillating wave that interacts with the charge carriers whose behaviour may be explained by quantum mechanics.

1.2.2 Systematic Wireless Power Transfer

The concept of rectifying an electromagnetic wave into DC power in an end-user system may be attributed to William C. Brown who proposed a rectenna system in the first paper submitted to The Journal of Microwave Power in 1966 [20]. In his paper, Brown deploys “An array of Half-Wave Dipoles Terminated in a Bridge-Rectifier Array of Point-Contact Silicon Diodes.” Although the diodes that Brown uses are assembled in a bridge form, the diagram of Figure 1.2 may be considered as a generic representation of rectennas based on its simple structure and the expandability of the model to higher frequencies.

In a later trial, Brown managed to increase the efficiency of his rectenna system to 92% [21]. This very good figure may be attributed to a) the use of a Schottky barrier diode that features a fast switching time as well as relatively low voltage drop, b) the use of a filter between the dipoles and the diode network which suggests that matching has been achieved between the two and c) the use of a high power level to feed the parabola that was used to wirelessly feed the helicopter over it.

This work has drawn attention to the possibility of reaching significantly

high efficiencies at high frequencies in the microwave region. For example, the work of Koert et al. [22] proved experimentally that an efficiency up to 72.5% is reachable at 35 GHz. Also, more than 35% efficiency has been reported in the experiment of Chiou & Chen [23] in 2010 at the 94 GHz band for a dual-band design thanks to using filtering and matching techniques to a pair of Schottky diodes at the circuit termination points. Having said that, the best efficiency experimentally achieved in the THz range has been always around 1% for the reasons that will be clarified later. The interested reader may refer to [24] for a detailed representation of the work in this field.

1.3 Motivation of Work

In order to identify the strengths and weaknesses of the energy harvesting systems studied in the research, the relationship between the achieved efficiency and the operation frequency is analysed. Figure 1.3 shows that with the progress of time, there is a trend to realize circuits that work at higher frequencies. However, there is an opposite trend in terms of the efficiency. That is, for higher frequencies the achieved rectification is lower. For example, while Brown managed to achieve an efficiency around 90%, the value in the study of Fumeaux is down to $< 1\%$ [18] for a measured experiment on 10.6 μm CO₂ laser. This justifies why still the majority of THz applications are confined to detection and sensing [25], [26].

With respect to these efficiencies, Corkish [29] suggests that the maximum theoretical limit for efficiency is in excess of 80% for sun radiation harvesting based on thermodynamics rules. In fact, Brown [21] has already exceeded the 90% limit for a 2.45 GHz system. If such high figures are achievable in the THz range, with high radiation intensity from sun radiation, or natural thermal radiation from earth surface with intensity around 70 W m² [30], then a major turnover would happen in the solar energy harvesting industry.

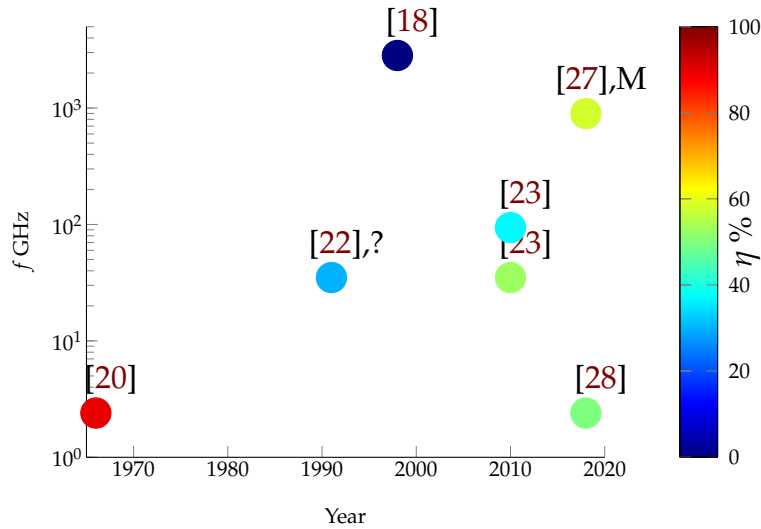


FIGURE 1.3: Chronological evolution of rectennas' frequencies and the corresponding efficiency. Colour of circles correspond to efficiency η based on the colour bar, numbers in brackets correspond to references in the bibliography. M refers to measured results, and ? means that the reference does not say.

The motivation of this work is to search for the possible reasons why the efficiency figure is low and try redesign the rectifier system accordingly. This would, primarily, entail revisiting the design of the rectifier diode and suggest other possible and realizable designs to improve this efficiency figure. By doing so, the generic and most frequently used theories will be revisited and briefly explained, and in the end, choose the theories that offer the best compromise between accuracy and computer complexity.

The output of this study will be a process that can be used to improve the performance of rectifying diodes in the THz range. This improvement will not reflect just for the higher frequency band, but it will also improve the diode performance for the millimetre band.

Similarly, the losses that happen in traditional phased array systems working in the mm range -which will be used in fifth generation (5G) networks- are mainly attributed to losses in the combiner circuitry [31], and gain/attenuation blocks [32]. Therefore, it is important to think of novel systems that redesign the synthesiser array circuit and/or generate a radiation

pattern that focuses the power more accurately. In this regard the time-modulated and frequency-diverse array techniques are presented and simulated to showcase their potential benefit for future wireless systems.

1.4 Thesis Outline

The following sections are organised such that the next section will be dedicated to the rectenna receiving part. In the following section, the mechanism of how nonlinearity can lead to signal rectification and hence harvest energy will be explained. As most of the Ph.D research has been dedicated to high frequency issues, there would be more focus on high frequency design than on low frequency leaving the treatment of the latter to a separate section. In chapter 2 I will also elaborate on why it is necessary to replace classical charge carrier movement models with quantum ones for higher frequencies. Then, the major quantum models will be visited. Out of these models, Simmons [33] model will be discussed in details with the experiments we made on its original, and enhanced forms drawing conclusions on its development aspects. The more robust Transfer Matrix Method (TMM) method will be also discussed in details focusing on its computation features. In the end, a framework to optimize the rectifier diode structure will be suggested and tried on realisable examples.

On the other hand, the power transmitter main design approaches will be overviewed. Instead of adopting the traditional approach in which gain and/or attenuation blocks are utilized, a new approach -namely TMA- exploiting the time/frequency characteristics of the excitation signal will be presented. The potential benefit of this approach lies in that it does not need any steering or attenuation circuits. Thus, offering potential power savings for circuit losses. Another novel technique, that is FDA, which results in

dimension-dependent radiation patterns will be also demonstrated. For both approaches, the co-simulation results will be demonstrated to identify possible enhancements and future work applications for both.

a simple design example is given in chapter 4 .

In the last two chapters, an exemplification of near-future battery-less sensors working at $f = 2.48$ GHz is given to showcase how the theory is deployed to move from a conceptual design to a market-ready application. Also, a helpful modelling platform specifically tailored for mid-range wireless powering scenarios in harsh electromagnetic environments will be presented in the following chapter.

Chapter 2

Receiving Part

In the previous section, it was demonstrated that the optimization of the receiving part efficiency is very important. However, due to the design frequency dependence [6], both the device and the optimization problem would be frequency-dependent.

To facilitate the design problem, I will start off laying out some mathematical concepts which would be applicable for all optimization problems. A brief review of the tunnelling-relevant theory will be demonstrated to explain the basics of tunnelling and quantum models utilised in the literature.

Based on the frequency value, the rectifier design approach will be categorised into low and high frequency design. The low frequency design approach is briefly reviewed and a real-world design example is given in chapter 4 from another activity relevant to the main Ph.D topic.

The problems that accompany higher frequencies -and are mainly analysed in this Ph.D work- will be demonstrated in the following section where I will explain why the Simmons model [34] is less likely to be adopted for future tunnel diode models. Then, I will explain the TMM model and the several trials made and lead to its current state.

As the previous models apply to a dark tunnelling current, a simplified representation of the $I(V)$ current relationship under illumination will be demonstrated.

In the end, I will explain how the TMM method is adopted in an optimisation process based on the FOM identified for nonlinear devices.

2.1 Preface

2.1.1 Nonlinearity Depolyment

The main functionality of this part is to convert the AC-received power, EM radiation, into a DC signal that supplies electric energy to subsequent parts. Be it for high or low frequencies, the rectifier exploits the nonlinear current-voltage relationship to transfer the power from the main frequency and its harmonics to the DC harmonic. The first analysis of the rectification and detection of the nonlinear behaviour may be attributed to Torrey and Whitmer [35] as they described the $I(V)$ relationship using Taylor's expansion as shown in (2.1). This approximation is very useful as it simplifies the nonlinear function to a summation of derivatives such that the mathematical analysis is greatly simplified. In fact, the function may be represented by more than two terms. However, the expansion beyond the second derivative depends on the swinging range of the voltage signal, and so having higher swinging range necessitates more terms, hence more harmonics, to have a more accurate approximation of the original function.

$$i = f(e_0) + \frac{df}{de} \delta e + \frac{d^2f}{de^2} (\delta e)^2 \quad (2.1)$$

where f is the $I(V)$ function, e_0 is the DC voltage level at which the expansion is found, δe is the swinging of this voltage due to the received AC signal. To explain how more terms mean more accurate approximation, let us assume an $I(V)$ relationship such that $I = f(V) = \cos(0.5V^2 + C)$ where $C = 0.5$ is a constant. The 4th order Taylor's expansion for this function is $\tilde{I} = \cos(C) - \sin(C)x^2/2! - 3 \cos(C)x^4/4!$ and the 2nd order expansion is the

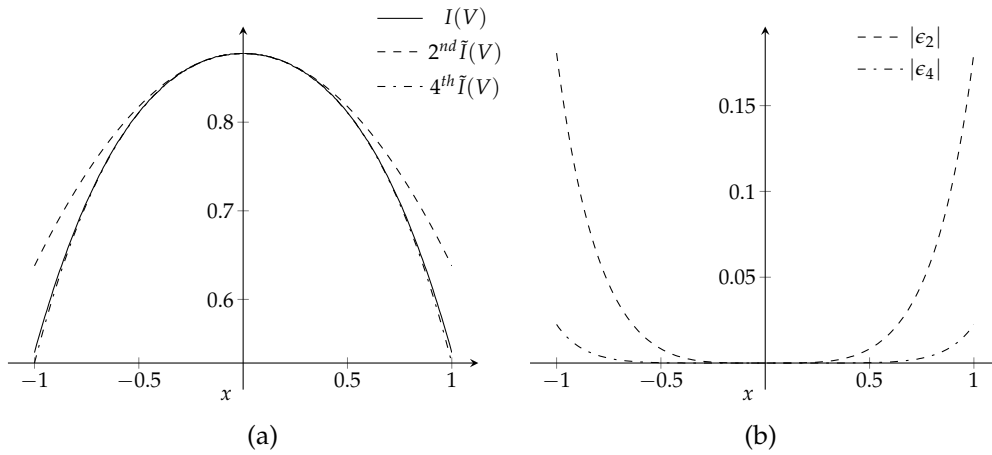


FIGURE 2.1: Comparison between original, 2nd order, and 4th order Taylor expansion values (a), and their corresponding error value ϵ from the original function (b).

same except the $-3 \cos(C)x^4/4!$ term. If we compare the original, 2nd order, and 4th order, we get the figures shown in Figure 2.1.

From Figure 2.1a, it is evident that the 4th Taylor's expansions $\tilde{I}(V)$ around $C = 0.5$ shows much better approximation to the original function compared to the 2nd expansion for a wider range of values. The more precise approximation is also reflected by the minimised error values corresponding to the 2nd and the 4th error values ϵ_2 and ϵ_4 in Figure 2.1b respectively. Having said that, both expansions exhibit approximate error values for input range $x < 0.35$. Therefore, both functions may be used to approximate the original as long as the error value is small.

This yields that *if the input voltage variation for the nonlinear device is small, then fewer terms of the Taylor's expansion may be used to represent the original function without compromising the accuracy of the approximation.* This concept explains why for the majority of nonlinear devices higher order harmonics become more important for signals that experience large variations. Therefore, it is common practice to approximate the $I(V)$ response curve with a many-order polynomial to get as similar response as possible [36], [37].

Having said that, the nonlinearity remains by far a subjective issue. That

is, the existence or the stability of a solution can greatly differ from one system to another based on input power level, harmonic content, and the detailed curvature of the $I(V)$ response. Fortunately, there is a good agreement [24], [38], and [39] to quantitatively characterise the diodes using specific criteria that a diode should satisfy to be considered a rectifier. The rectifier FOM are asymmetry $f_{asym}(V)$, nonlinearity $f_{NL}(V)$, and responsivity $f_{RES}(V)$. They can be calculated using (2.2), (2.3), and (2.4), respectively. In these equations the current is represented as a function of voltage $I(V)$, forward and reverse current values for the same voltage absolute value are $I_F(V)$, and $I_R(V)$, respectively. The minimum FOM values required are shown next to the respective equations, but, again, these ruling figures are just for guidance and each device design would have its own characters.

In addition to the aforementioned FOMs, it is useful also to include the dynamic resistance value (2.5) at a specific voltage v_0 to the FOM list. It is identified as the rate of change of the diode resistance at a specific voltage v_0 and has a major impact on the functionality of the diode as a nonlinear device. The recommended dynamic resistance values are subject to design as it will be demonstrated later.

$$f_{asym}(V) = \left| \frac{I_F(V)}{I_R(V)} \right| \qquad f_{asym}(V) > 1 \qquad (2.2)$$

$$f_{NL}(V) = \frac{dI(V)}{dV} \bigg/ \frac{I(V)}{V} \qquad f_{NL}(V) > 3 \qquad (2.3)$$

$$f_{RES}(V) = \frac{d^2I(V)}{dV^2} \bigg/ \frac{dI(V)}{dV} \qquad f_{RES}(V) > 7V^{-1} \qquad (2.4)$$

$$R_D(V) = \frac{dV}{dI} \qquad (2.5)$$

Looking at (2.1), it can be noticed that a sine voltage signal, will be raised

to the n^{th} power for the corresponding term. That is, the n^{th} term will contribute to the overall equation with the n^{th} harmonic. As the nonlinear device will be connected to other external devices -could be linear, nonlinear, or both-, it will exchange the power content of all harmonics with them. Therefore, the overall result will be a *balance* between the power content of all these harmonics. This formulates the basis of one of the most widely used steady state systems simulation process. That is, the Harmonic Balance (HB) which has been reviewed in [40], and is used in the NONLIN program [41].

2.1.2 Basics of Tunnelling

Before getting into further details, its important to pave the way by focusing on the terminology that will be used in the subsequent sections. In this preface I will start of with the generic and more theoretical concept, and will gradually narrow the theory to reach the practical aspects of tunnelling devices.

The difference of quantum mechanics, with respect to the classical picture, lies in the *uncertainty* whether a particle, an electron for example with a specific energy, would go through a specific barrier or not. While it is a yes/no approach from the classical view, it follows a *probability* function according to quantum mechanics.

From this aspect the Schrödinger wave equation is nothing but a probability-based function that describes the presence/absence of a particle at a specific place in a specific moment in a probabilistic manner. Therefore, the wave function has been developed based on the following assumptions:

- Conservation of energy before and after a quantum physical process.
- Quantization of energy such that particle energy levels are quantized as observed at the atomic scale.

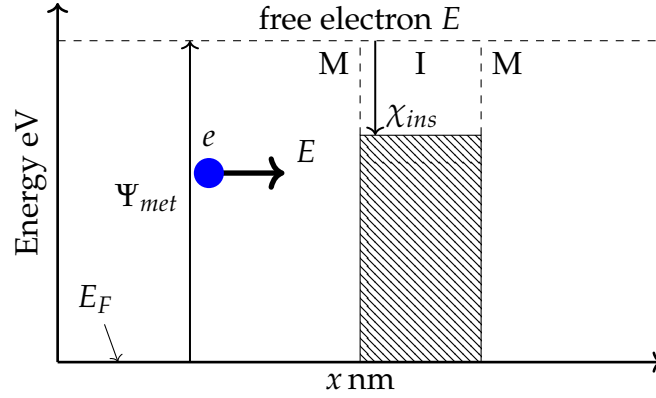


FIGURE 2.2: An electron having energy E moving in the $+x$ direction towards a barrier formed by the difference between the corresponding metal work function Ψ_{met} , and the insulator affinity function χ_{ins} .

- Particles can behave as waves as observed in electron and neutron diffraction experiments.
- Normalization of the wave function such that V includes all the space.

Presumably, the reader knows the time-dependent Schrödinger wave equation in a 3D space as shown in (2.6). Tunnelling category represents the quantum mechanism that describes the transition of charge carriers based on Schrödinger wave equation, which can be written in its generic form as follows:

$$i\hbar \frac{\partial \Psi}{\partial t} = -\frac{\hbar^2}{2m^*} \frac{\partial^2 \Psi}{\partial x^2} + V\Psi \quad (2.6)$$

$$\begin{aligned} \hat{H} &= \hat{T} + \hat{V} \\ &= \frac{\hat{\mathbf{p}} \cdot \hat{\mathbf{p}}}{2m^*} + V(\mathbf{r}, t) = -\frac{\hbar^2}{2m^*} \nabla^2 + V(\mathbf{r}, t) \end{aligned} \quad (2.7)$$

In (2.6) \hbar stands for Planck's constant divided by 2π , m^* is the particle

effective mass¹, i is the imaginary number, V is the potential energy the particle has, and Ψ is the wave function. The \hat{H} shown in (2.7) represents the Hamiltonian operator which consists of both the static energy $V(\mathbf{r}, t)$, and the kinetic energy operator represented by \hat{T} .

The solution of a time and space-dependent differential function is cumbersome. Fortunately, it is common practice to assume a separable form of the wave function such that $\Psi(\mathbf{r}, t) = \psi(\mathbf{r}) \cdot f(t)$ [42], hence the generic time-dependent formula can be solved based on the time-independent one using a variety of techniques [42], [43], [44]. Accordingly, in a 3D space, the wave function may be written as shown in (2.8).

$$\frac{-\hbar^2}{2m} \nabla^2 \psi(\mathbf{r}) + V\psi = E\psi(\mathbf{r}) \quad (2.8)$$

As most of the work here involves tunnelling in just one direction, we will simplify the formula of (2.8) into that shown in (2.9) which helps to describe the behaviour of an electron in a metal lattice when it faces an interface with a metal oxide or an insulator.

$$\frac{-\hbar^2}{2m} \frac{\partial^2 \psi(x)}{\partial x^2} + V\psi = E\psi(\mathbf{r}) \quad (2.9)$$

If a metal oxide layer is grown on a metal surface and then by another metal (e.g. by sputtering techniques [45]), the resulting structure may be regarded as a MIM one). Figure 2.2 shows a simplified scenario of a conduction electron inside a structure of this type. In this case, all conduction electrons will have an energy above the Fermi level E_F .

Considering just those which move towards the junction (i.e. in the positive x direction), they will be faced by the insulator which has a limited ability to host new electrons due to the tight bonds between insulator atoms

¹The effective mass represents an empirically-adjusted physical mass to account for the forces that neighbouring particles have on the studied electron in a lattice as opposed to its behaviour in vacuum.

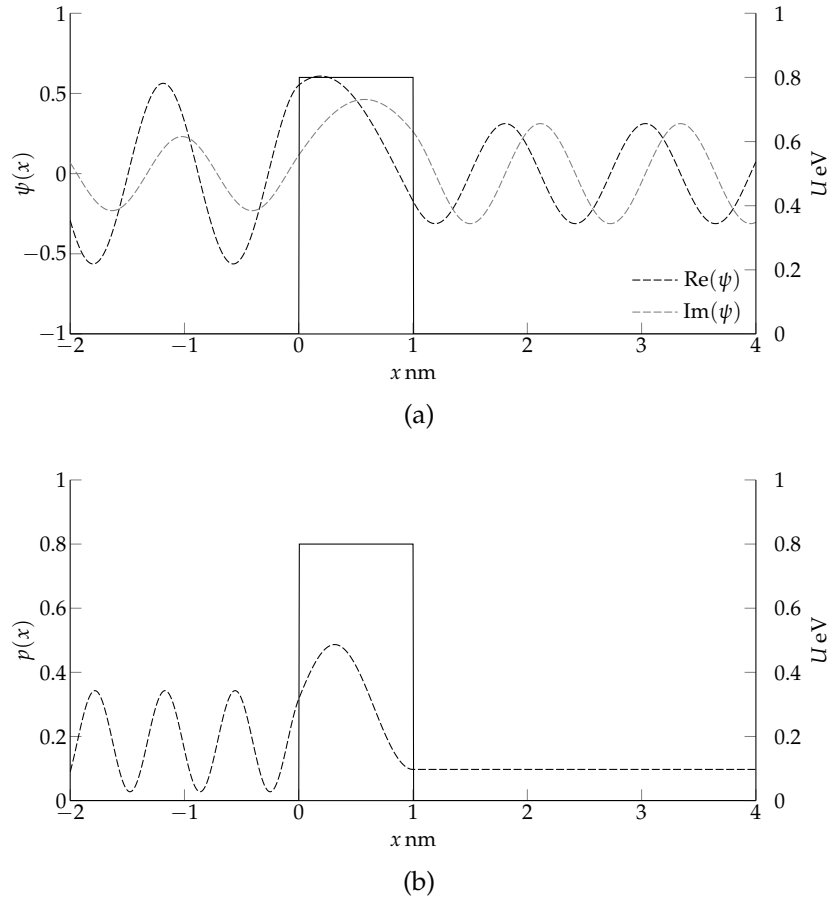


FIGURE 2.3: Real and imaginary wave function $\psi(x)$ components (a), and the corresponding probability $p(x)$ (b). In both figures the rectangular barrier is shown.

and their own electrons. From the electron point of view, this is a *potential energy transition* between the metal and the insulator mediums.

In classical mechanics, the electron can move into the lattice *if and only if* it has an energy E equal or greater than this potential energy transition. However, the quantum mechanics will explain its behaviour differently as will be shown later on. Conventionally, the aforementioned potential energy transition is identified by the difference between the metal work function Ψ_{met} and the insulator affinity function χ_{ins} . That is, the energy required to *free* an electron from the conduction band and the insulator ability to host a *free* electron into its lattice, respectively.

To solve the $\psi(x)$ equation shown in (2.9) for the scenario of Figure 2.2,

boundary conditions can be applied on the transition between metal and insulator layers in a way that guarantees the assumptions made for the wave equation mentioned earlier. This means that $\psi(x)$ should be continuous, smooth, and normalized such that $\int_{-\infty}^{\infty} \psi(x) \cdot \psi^*(x) dx = 1$. It is, therefore, common practice to assume a generic solution of the wave function as shown in (2.10) for the j^{th} layer of the medium.

$$\psi_j(x) = A_j e^{ik_j x} + B_j e^{-ik_j x} \quad (2.10)$$

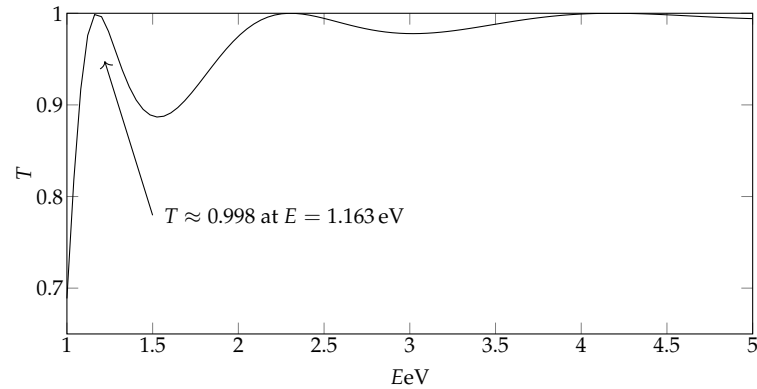
$$k_j = \sqrt{\frac{2m(E_j - V_j)}{\hbar^2}} \quad (2.11)$$

Such that the wave number k_j depends on the difference between the energy E_j and the potential energy V_j for the j^{th} layer, be it metal or insulator. In practice, it is difficult even for this simplified formula to accurately calculate the wave function when numerical computation methods are used to solve the boundary conditions.

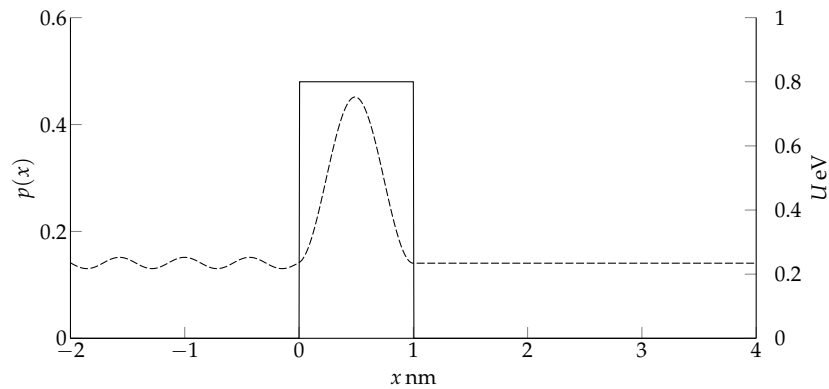
An introductory model developed by [46] which deploys transmission T and reflection R coefficients might be used as a starting point to model a simple tunnel with One Dimensional (1D) wave function.

To simplify the calculations, we assume a Fermi level at 0 eV for a MIM structure. In this case the electron will have zero potential energy $V = 0$ eV if it is inside the metal.

In classical physics, if the potential barrier ahead of it is 0.8 eV high and is 1 nm thick, then an electron with $E = 2$ eV energy will *certainly* be able to traverse the junction. However, the wave function gives a different result. Using the MATLAB model of Pujol [47], the MATLAB script in section A.1 calculates the $\psi(x)$ value as well as the probability $p(x)$ and puts the values in the `psi` and `rho` variables, respectively.



(a)



(b)

FIGURE 2.4: Probability function $p(x)$ with respect to x (a), and the transmission coefficient T value with respect to total energy E (b).

Figure 2.3a shows the output of the previous script for the real and imaginary parts of $\psi(x)$. The probability of the electron being at x is found from $\psi(x) \cdot \psi^*(x)$ and is shown in Figure 2.3b. The previous model solves the boundary conditions between the different layers and assumes normalization of the probability function just inside the limited simulated distance which extends from -2 nm to 4 nm. This justifies why the probability curve does not nullify to zero at the interval ends.

A special case happens when the transmission coefficient T has a value very close to one at a specific energy level E , at the same time R will be almost zero. That is, when an electron comes, it will almost surely get transmitted to the other side of the tunnel. This behaviour is seen with a wave function whose amplitude $|\psi(x)|$ remains almost constant with respect to x as shown

in Figure 2.4.

In Figure 2.4a the transmission probability experiences its first peak at $E = 1.163$ eV. Similarly in Figure 2.4b an electron with energy $E = 1.163$ eV is assumed and the corresponding probability function $p(x)$ is shown to experience very little swings before the barrier with a peak value inside the barrier region. Outside the barrier region, the swinging average is about 0.16 and the normalization to one is conserved.

2.2 Rectifier Design

To clarify the rectifier design process, the approach will be explained based on the frequency value such that low frequency-based applications would have a different design process from high-frequency counterparts. As will be explained in the next section, the threshold between low and high frequency design approaches may be considered to be around a few hundreds GHz, where some quantum effects begin to appear.

2.2.1 Design for Lower Frequencies

As explained earlier, the device nonlinearity is exploited to exchange the power content between different harmonics. As rectification is mostly wanted, then the power exchange should be in favour of maximizing the power output of the DC component. To achieve this, there are many widespread rectifier design schematics [7]. However, the following two approaches as shown in Figure 2.5 are the most frequent [28], [48].

In Figure 2.5a, the diode plays the role of the nonlinear device. The overall efficiency of the system (i.e. how much power is converted from the AC input to DC) is identified as shown in (2.12).

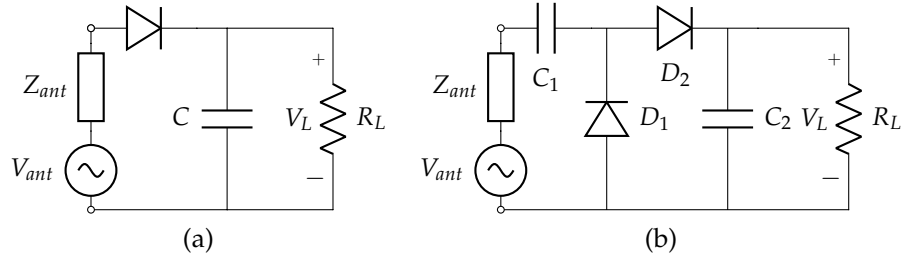


FIGURE 2.5: Common rectifier schematics for low-frequency energy harvesting. (a) Single-diode rectifier, and (b) Two-diode rectifier.

$$\eta = \frac{V_L^2}{0.5R_L \cdot \sum_{k_{f,1}}^{k_{f,max}} v_{k,in} \cdot i_{k,in}^*} \quad (2.12)$$

where V_L is the DC voltage output on the load resistor R_L . Assuming that the input signal contains a range of frequencies from $f = f_1$ to $f = f_{max}$ and that it is periodic, the corresponding input power will be the summation of the product of all the voltage harmonics $v_{k,in}$ with the current harmonics' conjugate $i_{k,in}^*$ multiplied by half to account for the effective power factor for each harmonic.

Based on this description the optimization problem will be to increase η . And so, there are some frequently-used techniques as voltage output maximisation [7] according to which the V_L is maximised by looking for the best values of C and R_L in Figure 2.5a circuit to maximise $V_L = f \cdot \int_0^{1/f_1} v_{out}(t) dt$.

Furthermore, in [49], the authors consider the transmitted signal for the optimization problem and so, they look for the best relationship between harmonics amplitudes and phases to maximize η . Their technique also takes into account applicability to multi-diode-rectifier circuits as shown in Figure 2.5b.

A more holistic approach for optimization is taken by [50], [51], and [52] in which a total simulation, accounting for both linear components, their mutual coupling, and nonlinear components are all accounted to in one simulation. And then the optimization is performed on the overall performance of

the system using one of the widespread techniques such as inexact Newton optimization [53].

According to the latter two approaches, the optimisation problem includes also the generator parameters. That is, V_{ant} and Z_{ant} . As mentioned earlier, a real world example available in chapter 4 to optimise a two-diode rectifier at $f = 2.48$ GHz explains the whole process starting from the theoretical model to a completely-realised prototype with the reported measurements.

Almost all nonlinear devices, including Schottky devices, are based on *classical* drift/diffusion theories that explain their behaviour. While p/n junction devices experience high charge carriers lifetime, Schottky devices feature improved performance due to almost zero minority carriers, and so minimised carrier lifetime which dramatically improve their performance even beyond 100 GHz [54].

However, the drift and diffusion theories which explain the behaviour of the aforementioned devices are based on classical treatment of particle movement [55], [56]. And so, their application is confined to lower frequencies, say, tens of GHz. If higher frequencies are targeted, then different theoretical treatment must be done. Regardless of the type of carrier generation or transition mechanism, the use of Schrödinger's wave equation is essential at higher frequencies where the carrier tunnel traversal time becomes close to the signal oscillation frequency [44].

2.2.2 Design for Higher Frequencies

As mentioned in subsection 2.2.1, ~~necessary to approach high frequency devices differently~~ it is important to consider different factors for higher frequencies rectification. This does not only hold true for carrier mobility, but also for the nature of the harvested signal at high frequencies. Therefore, I

will approach the design problem here from a) the nature of the radiated signal, and b) the available charge carrier models. In fact, five factors have been identified in [6] as design rules for THz rectennas. The following subsection overviews the main characteristics which identify the THz electromagnetic signal.

THz Radiation Characteristics

- THz radiation is wide band:

For such frequencies, there is usually little control over the radiating object such that the radiation may come out from any object around the rectenna device, be it walls, floor, hot surfaces, or maybe the visible light. And the reason for this radiation is just because the object has a temperature above 0K where the matter particles are agitated and so they radiate energy at very high frequencies. It is, therefore, convenient to assume all surrounding objects to follow the black body radiation law. It is out of the scope of this paper to discuss the theoretical details of this physical phenomenon and the reader may consult [57] for further information about its equation. Figure 2.6 shows the radiation intensity functionality -regardless of the values- with respect to wavelength λ . As the root locus of the intensity peak shows, when the radiating body temperature rises, the intensity peaks rise in amplitude and shift to the left which represents an increase in the corresponding frequency f . For a radiating body whose temperature is 7000 K, the intensity has a sharp peak at the highest visible wavelength -violet colour-. Conversely, a 3000 K body has a much lower intensity peak, much wider spectrum, and the peak occurs within the invisible infra red range.

While harvesting energy from the sun can be very rewarding based on

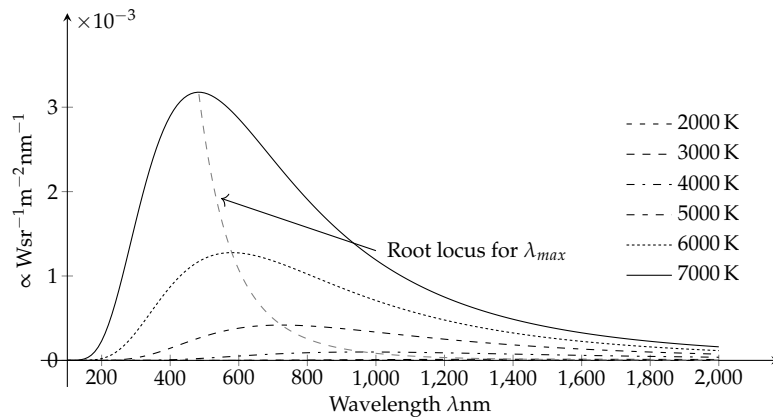


FIGURE 2.6: Black body radiation law curves for different temperatures.

its high intensity, attempting frequencies as high as 800 THz is quite challenging with the available technology. On the other hand, there are many other sources that provide a good deal of energy at lower temperatures -hence lower radiation frequencies-, and have more realistic designs to attempt. For example, the radiated heat from hot surfaces such as those of hot engines, motors, chimneys, etc. is better harvested than get wasted into the space and they are quite abundant. This energy source is usually referred to in the literature as *waste heat* energy source [12].

Having said that, they have some challenges such as their wideband nature as seen on the Figure 2.6, very low power level that requires very low opening voltage for rectifying diodes, as well as their proximity to the harvesting rectenna in any future design which in turn may lead to diminishing returns. In practical terms, if waste heat sources are assumed to have temperatures around 373 K, their radiation intensity peak will be around 30 THz according to Planck's radiation formula [57] and the corresponding wave length $\lambda = 10 \mu\text{m}$.

The dielectric constant values reported for many oxides used today in

THz diodes fabrication have contradicting values reported in the literature. For example, the niobium oxide Nb_2O_5 , has different reported values in each of [58], [59], and [60]. Among many other factors the frequency under which the material was tested, the frequency plays a major role in its value.

- THz radiation is random:

While RF antennas have a certain relationship that controls the radiated electromagnetic field from all the antenna aperture points, THz black body radiation, no matter at which frequency occurs, has a wide band nature, is radiated by the whole *surface* it comes from, and can be considered randomly polarized. Accounting for these factors will lead to a significant impact on the rectified wave efficiency, the best size for an antenna array to achieve optimum efficiency, and of course the expected signal amplitude at the rectifier input.

Mashaal & Gordon [61] have conducted a rigorous study to account for this impact for sunlight. In this work, Mashaal & Gordon have conducted a study on the solar light to identify the coherence of the incident ray in addition to the optimal antenna size to maximise the received power.

In their publication Mashaal & Gordon utilise the Equal time Mutual Coherence Function (EMCF) which is identified in (2.13) based on van Cittert-Zernike theorem. This work assumes that higher coherence factor $EMCF$ between $\mathbf{E}(\mathbf{r}, t)$ and $\mathbf{E}(\mathbf{r}', t)$ would result in higher likelihood for a higher power at the antenna output.

Although this occurs at much higher frequencies, the results might be extended to lower frequencies as far as the EM wave theory and black body radiation are concerned.

$$EMCF = \langle \mathbf{E}(\mathbf{r}, t) \cdot \mathbf{E}^*(\mathbf{r}', t) \rangle_t = 2\eta \int_{\sigma} I(s) \cdot \frac{e^{ik(\mathbf{r}-\mathbf{r}')}}{\mathbf{r} \cdot \mathbf{r}'} ds \quad (2.13)$$

According to van Cittert-Zernike theorem, the time-averaged product of two fields emanating from a radiating source on two different points of an aperture antenna is given by (2.13) where: η is the vacuum impedance, $I(s)$ is the irradiance of the source, r and r' are the coordinates of the different points of the aperture antenna, and k is the wave vector of the incident wave. The integration is performed over the entire radiating source surface σ .

Mashaal & Gordon [61] have found significant results by running this integral for monochromatic and wideband sources in the visible range. That is, the intercepted power by the antenna is proportional to the aperture area if the aperture radius is much smaller than the average wavelength $\bar{\lambda}$.

However, when the aperture is much larger than the wavelength, the intercepted power by the antenna is independent of antenna size and relies only on the wavelength and the source irradiance. This sets limits as to how large the aperture should be.

A more realistic approach might be reached by integrating the EMCF function over the entire bandwidth after introducing the frequency-dependent terms into (2.13). This has led to the EMCF curves shown in Figure Figure 2.7 which show that the situation is not much different for the wideband nature of light as compared to the quasi monochromatic cases represented on the same graph.

For waste heat sources, the distance between the source and the rectenna array is very small. When integrating over the radiating surface, the

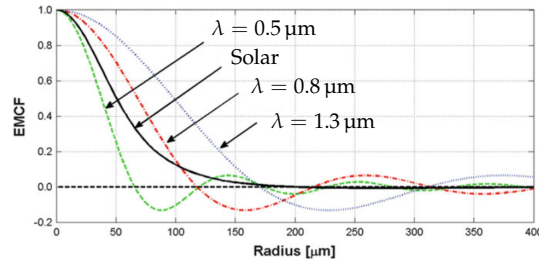


FIGURE 2.7: EMCF function curve for the quasi monochromatic light for wavelengths $\lambda = 1.3 \mu\text{m}$, $0.9 \mu\text{m}$, $0.5 \mu\text{m}$ and for solar black body radiation. (Reprinted by permission from Springer Nature: [61].)

aperture radius values which yield higher EMCF values will be considerably smaller than those obtained for the sunlight as in Mashaal & Gordon study [61]. This aspect should be accounted for in future THz rectenna design.

From Figure 2.7 it can be concluded -except for the lowest wavelength $\lambda = 0.5 \mu\text{m}$ - that for any aperture radius below $100 \mu\text{m}$ quasi monochromatic light is more likely to deliver higher power to this aperture than the complete bandwidth of the solar light.

This result has been pronounced also by Divit & Novotny [62] suggesting that splitting the whole solar bandwidth into smaller sub bands would yield higher efficiencies as the case for multi junction solar cells. This solution can be extended to be applied also to rectennas as this defect relies merely on the wideband nature of light and has nothing to do with the successor stages.

Overview of Charge Carrier Models

Although increasing the operation frequency opens up a new range for applications, the process is hampered by many challenges. For example, the classical physics approach used for describing charge transition in semiconducting material fails to explain their behaviour at extremely high frequencies when

the radiation wave oscillates at much higher speeds than those of charge carriers. Also, there is no consensus on the relationship between tunnelling traversal time and the oscillation frequency. While Büttiker and Landauer [63] argue an inverse relationship between the tunnelling traversal time τ and the oscillation frequency ω , Truscott [44] considers that “the onset of frequency dependence is not a general property of the barrier”. This means that tunnelling at higher frequencies is still expected to happen with more efficiency than expected by Büttiker-Landauer’s approach. Indeed, Liu’s experiment [64] supports this finding where he states that “the tunnelling time consideration is only an estimate.”

At these speeds, quantum approaches extend to explain the behaviour based on Schrödinger equation. Equally importantly, the effect of photon assisted tunnelling [65] which explains the behaviour of electrons crossing a potential barrier illuminated by a radiation with frequency f . This effect starts to get noticed even before reaching the 1 THz frequency as stated by Habbal et al. [17].

The literature review reveals many modelling techniques based on the carrier transmission mechanism as well as the nature of the modelled device. To facilitate the process, I have categorized the different models as shown in Figure 2.8 with the corresponding reference numbers next to each model type.

Generally speaking, they can be divided into three main categories. That is, tunnelling, geometric, and a hybrid mode which shares some features of the previous two. For brevity, I will focus only on two models which have been tried in this Ph.D work and the interested reader may get further details about other models from [6].

- THz Tunnelling:

For this category and regardless of the tunnelling theory, the procedure is the same such that the Schrödinger equation is used to calculate the

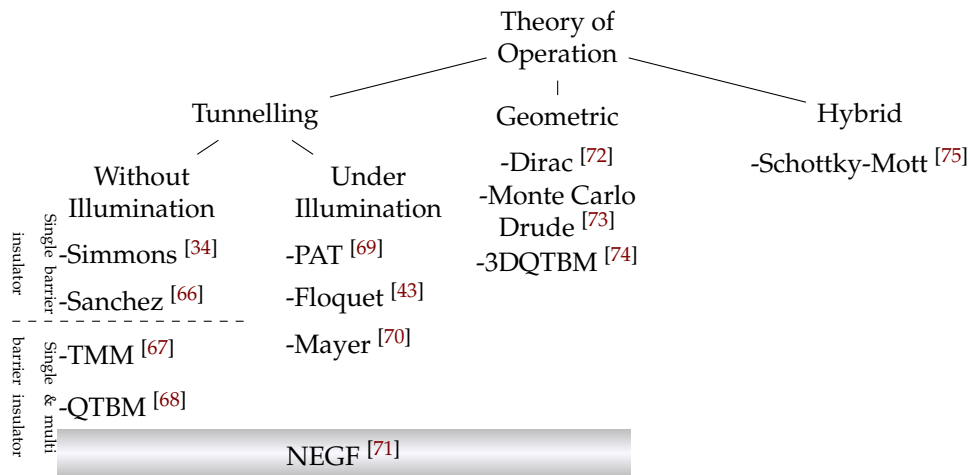


FIGURE 2.8: Categorisation of theory of operation

transmission probability of the electron and then the current density can be found from multiplying this probability by the number of available electrons. This theoretical framework is well explained in [34], and [66]. The current is then simply the current density multiplied by the contact surface area.

This represents the mainstream approach for tunnelling-based current although Heiblum et al. [76] argue that the tunnelling effect happens at the surface edges rather than the centre part of the junction. The experiment result of [18, Fig. 29(b)] supports this assumption where the polarisation-dependent response component V_p seems to level out with increasing the contact area in an asymptotic approach

Following in Figure 2.9, the diagram shows the energy band of one type of tunnelling diodes -MIM diode-, when the diode is forward biased, the electron will tunnel from the higher barrier region identified as Φ_L , to the lower barrier region identified as Φ_R . This is an asymmetric diode where the barrier heights are different at both ends, and this happens when two metal types are used.

Conversely, a symmetric diode utilises electrodes of the same metal at

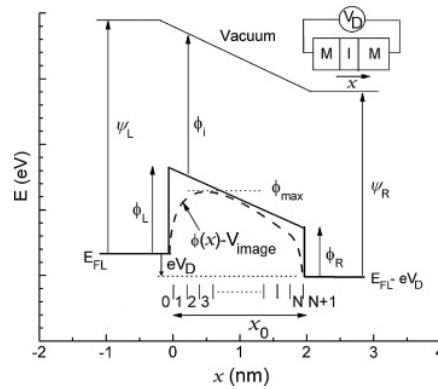


FIGURE 2.9: Energy band diagram of a metal-insulator-metal MIM tunnelling diode. (Reprinted by permission from Elsevier: [37].)

both ends. It is important to notice that the tunnelling will occur anyway, with or without an illuminated junction, as long as there is enough forward bias represented as displacement between Fermi levels of the left and right regions by eV_D and in the same direction shown in the figure. Illumination of the junction would affect the tunnelling phenomenon differently as experimentally represented [17].

- Geometric Devices:

While most of the THz-rectifying diodes' behaviour can be explained only with quantum physics, geometric diodes seem to have comparably accurate simulation results, using the classical Drude model, to those obtained through quantum simulations without their complexity [73]. Geometric diodes are structurally different from other types, and have some beneficial modelling features as it will be explained.

These devices depend on physical asymmetry to simplify the movement of charge carriers into one direction more than the other. They are primarily ballistic devices that use long mean-free path length (MFPL) material to achieve this goal [77]. The recent development in graphene industry and properties has fostered its use for this goal such that a tapered graphene structure, as that shown in Figure 2.10, would facilitate

the movement of electrons from the wider side to the narrower side.

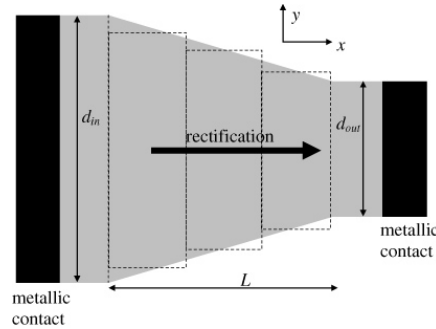


FIGURE 2.10: Schematic representation of the ballistic rectifier.
(Reprinted by permission from IOP Publishing: [78].)

Technically, graphene devices have a very special feature compared to metals and semiconductors due to linear energy dispersion relation near the Dirac point [79]. Modelling a device with this special energy and carrier transport features has also many approaches. However, there seems fewer theoretical frameworks and little agreement between experiment results and theoretical models output.

For example, Dragoman & Dragoman [78] have developed a model for the two-dimensional electron gas (2DEG) nanodevice based on Dirac equation [72] of the wave equation for the relativistic particles. Their model is based on Figure 2.10 where the device is sliced up into N cells and the solution is found for each slice based on the boundary conditions.

Although this method accounts for relativistic occurrences, the output results do not agree with measurements. This has been reported by Dragoman et al. [80] where they reported that the rectification region is less compared to that indicated by the simulation, and the measured current is a bit higher.

On the other hand the Monte Carlo simulation assumes electron movement and collision in geometric diode according to Drude model. In his work, Zhu [73] has developed a model where the electron collides

with the structure boundaries, phonons, other electrons,... such that the electron moves within the device with velocity v_{tot} which is a composite of Fermi and current drift velocities. Stellingwerff [81] has also tried the Monte Carlo method to simulate of his model.

Although there has been some important results from the work of Zhu [73], no agreement has been obtained between the modelled and measured current values. The work of Stellingwerff [81] does not deliver fundamentally different results where he argues that the simulation results provide expectation of the measured results without directly comparing them.

To sum up on the current state-of-the-art for this algorithm, the output accuracy is disputed and it can be used for knowledge of the general behaviour of the device. Having said that, the simplicity of this method and avoidance of the more complicated quantum description is interesting.

- Hybrid Devices:

The reason we name them hybrid is because they have both features of geometric devices -with large MFPL- and junction diodes where a voltage drop is present at the junction between the graphene layer and the doped semiconductor substrate. They have earned recent interest based on their features [82]. The thermionic emission in conjunction with Schottky-Mott model gives surprisingly good description of their electrical properties as stated by Tongay, et al. [82].

Dragoman & Aldrigo have recently modelled this device and obtained efficiencies in excess of 58% at 897 GHz for a graphene antenna on a n-doped GaAs substrate [27]. The Schottky-Mott model equation used in their study is Equation 2.14.

$$I(T, V) = A_{sub}^{gr} \cdot A^* \cdot T^2 \cdot \exp\left(-\frac{e\phi_{SBH}}{k_B T}\right) \cdot \left[\exp\left(\frac{eV}{\eta k_B T}\right) - 1\right] \quad (2.14)$$

Where $I(T, V)$ is the current response of the device with respect to voltage and temperature, A_{sub}^{gr} is the contact surface area between the graphene and the substrate, A^* is the Richardson constant, T is the temperature in Kelvin, ϕ_{SBH} is the Schottky barrier potential height, V is the applied voltage value, η is the ideality factor and k_B is the Boltzmann constant.

Although the tried frequency is below the THz band, the modelling for this device results in *exceptional efficiencies* compared to all the experiments reviewed in this paper. The structure, also, takes benefit from the small capacitance of the graphene-substrate junction. However, no measured data is provided for this model to compare to in the THz band. It is also expected to obtain different response at higher frequencies due to the increasing impact on the wave/Dirac function waveforms.

- Non Equilibrium Green Function

In the Non Equilibrium Green Function (NEGF) the algorithm attempts to solve the wave function, without involving directly the Schrödinger equation, using the following definition for Green function as shown in (2.15) taken from [83].

$$(E - \hat{H})G(E) = \mathbb{I} \quad (2.15)$$

Assuming a wave function, the time independent Schrödinger equation can be expressed as:

$$\hat{H}\Psi(\mathbf{r}) = E\Psi(\mathbf{r}) + V \quad (2.16)$$

Where V is the small perturbation introduced to help finding a solution to this equation according to perturbation theory [84]. Now, the wave function can be found directly from (2.17)

$$\Psi(\mathbf{r}) = -G(E)V \quad (2.17)$$

The theoretical framework is rigorous and will not be attempted here. The algorithm is frequently quoted for its accuracy [85], [86]. An outstanding feature of this modelling scheme is that it can be applicable to “uniform illumination” as stated by Datta & Anantram [71] where the oscillating field is expressed such as $V(z, t) = V(t) = V_0 \cos(\omega t)$ or if it takes a phase-dependent form with respect to space such that $V(z, t) \sim V_0 \cos(\omega t - qz)$.

More importantly, it is applicable to other devices than tunnelling ones such as the geometric diode simulated by Zhu et al. [77]. Yet further, the algorithm can account for time-modulated potentials, and so it becomes extendible for time dependent equations [71] as shown in Figure 2.8.

On the contrary, its complicated math makes it computer intensive since it can be used to describe tunnelling, non-tunnelling, and time dependent voltage scenarios.

Rectenna Under Illumination

In any of the previous cases, the barrier can be either considered constant with time, for which case the models of Simmons, Sanchez, TMM, and Quantum Tunnelling Boundary Method (QTBM) are applicable. On the other hand, an oscillating barrier entails the use of the Photon Assisted Tunneling

(PAT) [69], Floquet [43], or Mayer [70] models, as shown in Figure 2.8, if the barrier oscillates with extremely high frequency compared to the tunnelling traversal time [87].

The latter case entails the assumption that a phase change in the oscillating barrier may happen during tunnelling. A rigorous study has been made early in 1963 by Tien & Gordon [69] to find out a relationship between the barrier oscillation frequency and the tunnelling current assuming a time-space separable form of the wave function as shown in (2.18).

$$\Psi(\mathbf{r}, t) = f(\mathbf{r}).e^{\frac{-iEt}{\hbar}} \quad (2.18)$$

Where $\Psi(\mathbf{r}, t)$ is the modelled wave function, $f(\mathbf{r})$ is a spatial function, E is the quasi-particle energy, i is the imaginary number, and \hbar is the reduced Planck's constant. The introduction of an oscillating perturbation into the Hamiltonian results in the following equation (2.19).

$$\hat{H} = \hat{H}_0 + eV \cos \omega t \quad (2.19)$$

Tien & Gordon [69] support their space-independent perturbation approach by the assumption that the wave function drops very sharply at both ends of the tunnel, so the interaction with the electric field is so small that it happens just inside and around the very thin insulation (oxide) layer. Based on that they put the following form for the wave equation as shown in (2.20).

$$\Psi(\mathbf{r}, t) = f(\mathbf{r}).e^{\frac{-iEt}{\hbar}} \left(\sum_{n=-\infty}^{n=+\infty} B_n . e^{in\omega t} \right) \quad (2.20)$$

Working out some math, they find the coefficients B_n to be $B_n = J_n \left(\frac{eV}{\hbar\omega} \right)$ where J_n represents the n^{th} order Bessel function of the first kind. Without delving too much into the math, the current value for a tunnelling device

under illumination is found to be dependent on both the photon energy represented by its frequency ω and the oscillation amplitude V_ω .

The illumination current is found out from Tien & Gordon [69] model as shown in (2.21) and is frequently used to explain the experiments outputs up to a few THz [88], [65].

$$I_{illum} = \sum_{n=-\infty}^{n=+\infty} J_n^2 \left(\frac{qV_\omega}{\hbar\omega} \right) \times I_{dark} \left(V_D + n \frac{\hbar\omega}{q} \right) \quad (2.21)$$

Where the I_{illum} is the resultant illumination current, q is the particle charge -the electron charge in this case-, V_D is the DC voltage across the tunnel. The terms are summed from $-\infty$ to $+\infty$ to scan all the possible wave function modes.

In physical terms, the illumination current is the composite result of emitting and/or absorbing photons with frequency ω such that the $n < 0$ terms represent the absorption of photons and $n > 0$ represents their emission. The amplitude of the Bessel function for each term represents the *likelihood* of the corresponding occurrence (i.e. a photon gets absorbed/emitted).

Another issue is how many terms shall be included in a calculation? This by far depends on the value of the n^{th} Bessel function with respect to the fundamental one where the voltage amplitude has a major impact. Empirically, Joshi & Moddel [88] use values $n = -1, 0, 1$ in their model.

To represent this impact, Let's assume an ideal 2^{nd} order nonlinear diode as shown in (2.22). Assuming a rapidly oscillating AC signal with hundreds of GHz frequency, and an oscillation amplitude $V_\omega = 2.48$ mV the term $\frac{qV_\omega}{\hbar\omega}$ will have a significant value about 1.5 which makes the contribution of Bessel function significant with their values around 0.56, 0.51, and 0.56 for J_{-1} , J_0 , and J_{+1} respectively. Furthermore, the $\frac{q}{\hbar\omega}$ term will result in displacing the $I(V)$ response through the $\left(V_D + n \frac{\hbar\omega}{q} \right)$ term to the right or left with respect to the applied DC voltage value depending on whether a photon absorption

$n = -1$ or emission $n = +1$ occurs. In other words, we will have a non-zero current at zero bias and the direction of the current flow depends on the $I(V)$ DC functionality.

$$I(V) = \begin{cases} 0 & V \leq 0 \\ V^2 & V \geq 0 \end{cases} \quad (2.22)$$

In the following model we simplify the photon-particle interaction to just first order in the sense that just one photon emission/absorption is allowed at a time. The overall result, in this case, will be a raised $I(V)$ curve around zero. The value how much it gets raised depends on the oscillation frequency, oscillation amplitude, and the resulting Bessel function's values. As the frequency increases and so the impinging photons have higher energy, the contribution of PAT in this always-increasing function is a raised *knee* particularly around zero.

Figure 2.11a shows how the increased impinging illumination frequency even for the same amplitude V_ω increases the current value at zero due to the assisted tunnelling process with respect to the dark tunnelling current. For an illumination at 1 THz the simulated current value is 1.407 μA at 0 V biasing. Also, increasing the oscillation amplitude will result in a corresponding increase in the tunnelling current as shown in Figure 2.11b.

Of course, this approach tends to take the *classical* view when the photon energy (i.e. oscillation frequency) is smaller. The return to the classical approach may be obtained from the aforementioned dynamic resistance FOM shown in (2.5), which takes the form shown in (2.23) in this PAT semi classical picture [89]. In this form, the $\frac{\hbar\omega}{q}$ term has been replaced by V_{ph} to simplify the mathematical notation.

$$R_D^{PAT}(V_D) = \frac{2V_{ph}}{I_{dark}(V_D + V_{ph}) - I_{dark}(V_D - V_{ph})} \quad (2.23)$$

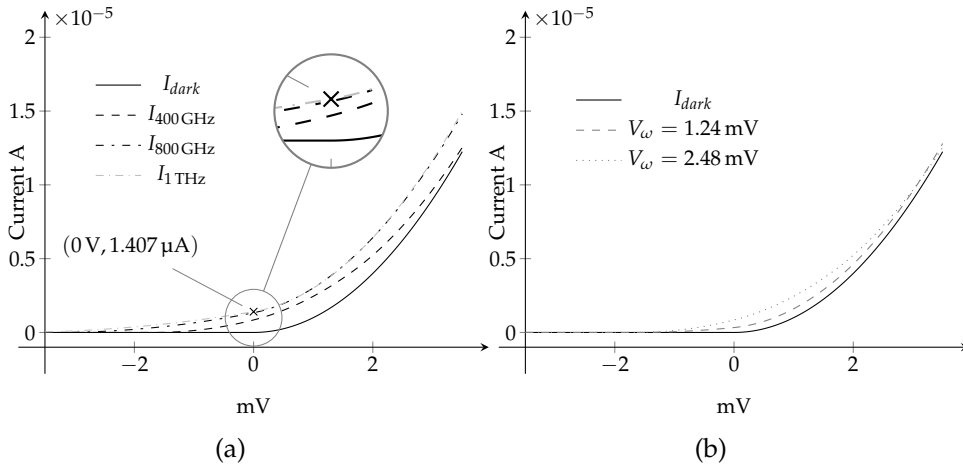


FIGURE 2.11: Impact of changing the oscillation (illuminating wave) frequency on tunnelling current (a). Impact of changing the oscillation amplitude V_ω on the tunnelling current (b).

As the frequency drops, the photon energy and hence the V_{ph} value is reduced. For small enough values, we can consider V_{ph} to be dV and so $R_D^{PAT}(V_D)$ can be written as shown in (2.24) which properly represents the inverse of the derivative of current with respect to voltage at V_D .

$$R_D^{PAT}(V_D) = \frac{2dV}{I_{dark}(V_D + dV) - I_{dark}(V_D - dV)} = \frac{2dV}{2dI_{dark}(V)} \Big|_{V_D} \quad (2.24)$$

Contrary to the easier approaches of tunnelling under no illumination, this concept results into a *nonlocal* functionality of current to voltage where the notation $I(V)$ becomes no longer accurate because it represents an instantaneous dependency; whereas the current I depends on the current and previous values of voltages in this model. The functionality represented in (2.21) is in the frequency domain such that the current harmonics are found instead of its time dependent value which is attempted by Tucker & Feldman [65] and takes a more complicated form.

Nevertheless, they assume that higher order nonlocal harmonics of this

system are less important as the frequency gets extremely high and the extremely high reactive effect of the linear components minimise their impact to negligible levels.

2.3 Simmons Model

2.3.1 Overview

This model has been proposed by John Simmons [34] to find the $I(V)$ curve of a diode consisting of a thin insulating film between two metal electrodes. In his paper, Simmons assumes a potential barrier which takes into account the image forces [90] and formulates its approximation using a continuous function. The resulting current of the applied voltage is calculated by finding the probability of an electron passing through the tunnel -using Wentzel, Kramers, and Brillouin (WKB) approach [91]-, and multiply it by the number of the available free electrons. The likelihood function is developed from the Schrödinger equation assuming that the electrons transfer happens only in the x direction.

While it is a frequently cited model in the literature, there seems to be many limitations to be used in an accurate diode modelling. In this section I will briefly explain how the model was developed starting from the potential barrier formula, and the WKB approach and will show the results of some simulations of this models and their important outcomes.

2.3.2 Potential Barrier Formula

As shown in subsection 2.1.2, a potential barrier would formulate when a thin oxide layer is grown on metal surface. If another metal layer is created on the opposite oxide surface, the thin oxide layer will play a barrier role in front of metal electrons. Assuming that each metal has a different work

function value, the potential barrier height² may be described according to (2.25) which works for both symmetric and asymmetric diodes³.

$$V(x) = \phi_1 - (\phi_1 - \phi_2 + e|V|) \cdot \frac{x}{L} \quad (2.25)$$

Such that:

$$\phi_i = \Psi_i - \chi_{ins} \quad (2.26)$$

Where ϕ_i represents the difference of the i metal work function from the insulator affinity function χ_{ins} . The Simmons model takes into account the image forces lowering effect in the potential barrier model. That is, due to the presence of an electron cloud in the metal lattice next to the junction with the insulator, new charge carrier positions are evacuated in the insulator lattice and hence giving more room to the metal electrons to move into the insulator lattice.

The impact is basically a lowered potential barrier to facilitate the move of electrons throughout the tunnel. According to the model used in [58] and [39] an image force lowering term may be added to (2.25) such that it becomes:

$$V(x) = \phi_1 - (\phi_1 - \phi_2 + e|V|) \cdot \frac{x}{L} - \frac{0.288L}{Kx(L-x)} \quad (2.27)$$

In (2.27) x refers to the position at which the potential is evaluated, L is the oxide thickness, and K is the relative dielectric constant. Assuming a Nb/Nb₂O₅/Au MIM diode such that the potential barriers of the left and right metals are $\phi_1 = 0.75$ eV and $\phi_2 = 0.275$ eV respectively [39, Table II], a potential barrier is generated as shown in Figure 2.12.

When the diode electrodes are zero biased, the resulting potential barrier without image forces is that shown in black trapezoid in Figure 2.12. Adding

²The potential here has an eV unit not V

³When the two metals are the same the diode is called symmetric, and vice versa.

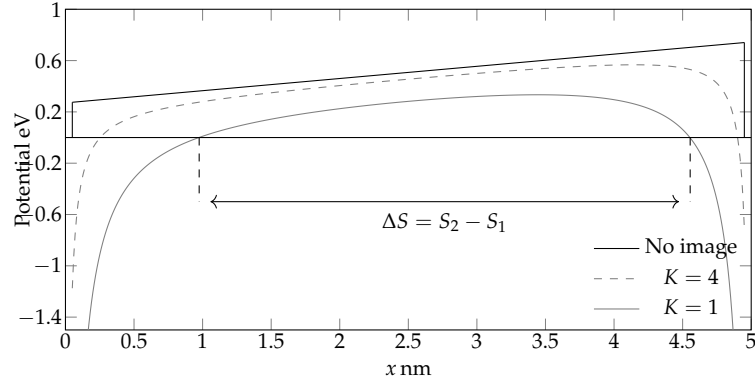


FIGURE 2.12: Potential barrier for a Nb/Nb₂O₅/Au structure with $L = 5$ nm insulator thickness assuming different image forces values.

image forces to the calculation will directly drop the barrier and will reduce the distance of the positive potential value ΔS above the higher Fermi level. The lowering is more for smaller dielectric constant values as shown in the same figure. This, in fact, has two outcomes:

- Physical outcome where the potential is reduced and the tunnelling current is increased.
- Mathematical outcome such that it is possible to have negative potential for all the tunnel width, and this leads to mathematical complications when realizing this model on computer.

2.3.3 Tunnelling Current

In order to find the tunnelling current, the following electron tunnelling probability is used based on WKB approach:

$$D(E_x) = \exp \left\{ -\frac{4\pi}{h} \int_{s_1}^{s_2} \sqrt{2m^*(V(x) - E_x)} dx \right\} \quad (2.28)$$

Where, E_x is the energy component of the incident electron in the x direction.

The current density value J_{tun} may be found based on the following integral:

$$J_{tun} = \frac{4\pi m^2}{eh^3} \int_0^{E_m} D(E_x) dE_x \int_0^{+\infty} [f(E) - f(E + eV)] dE_r \quad (2.29)$$

Where E_m represents the maximum electron energy available in the electrode, E_r is a *polar* energy component found in xy coordinates to calculate the electron distribution function, $f(E + eV)$, and $f(E)$ represent the Fermi electron distribution function values in the right and left electrodes, respectively.⁴ The calculation treatment will lead to the J_{tun} equation shown in (2.30) for low-voltage biasing.

$$J_{tun} = J_0 \frac{\bar{V} \cdot e^{-1.025\Delta S\sqrt{\bar{V}}} - (\bar{V} + |V|) \cdot e^{-1.025\Delta S\sqrt{\bar{V}+|V|}}}{(\Delta S)^2} \text{ Acm}^{-2} \quad (2.30)$$

Where:

$$J_0 = 6.2 \times 10^{-10} \quad \text{A}\dot{\text{A}}^2\text{V}^{-1}\text{cm}^{-2} \quad (2.31)$$

$$\Delta S = S_2 - S_1 \quad \text{\AA} \quad (2.32)$$

$$\bar{V} = \int_{S_1}^{S_2} V(x) dx \quad \text{eV} \quad (2.33)$$

In (2.30) the barrier height is considered for the whole tunnel based on an averaged value of the potential barrier shape in the form of an integral (2.33).

In addition to this value, there is the thermionic contribution of the electron thermal agitation which increases the overall current value based on the thermionic equation shown in (2.34).

$$J_{th} = A^* T^2 e^{(V_{\phi max}/k_B T)} \left(1 - e^{-eV/k_B T}\right) \quad (2.34)$$

⁴for further information about the calculus, the reader is advised to read from [33].

And the overall tunnelling current density value will be:

$$J_{tot} = J_{tun} + J_{th} \quad (2.35)$$

Where $V_{\phi_{max}}$ is the maximum value of the potential barrier with respect to the negative biased electrode, and V is the voltage applied to the diode. Using the MATLAB script available in Appendix A, and the parameters shown in Table 2.1, the $I(V)$ response is that shown in Figure 2.13.

Parameter	Value
T	300 K
ϕ_{Nb}	0.275 eV
ϕ_{Au}	0.75 eV
L	5 nm
K	8

TABLE 2.1: Used parameters in Simmons model.

As shown in Figure 2.13, the model experiences an abrupt change around $V = 2.4$ V. In fact, there is a sign change in the tunnelling current value but is represented here by this squint as we draw the absolute current value on a semi logarithmic scale. This happens when the $(\bar{V} + |V|)$ term becomes larger than the \bar{V} one in (2.30). The physical meaning of this change is disputable.

Moreover, the barrier potential for V values higher than 3 V does not intersect with the higher Fermi level, in which case we will have an unsolvable system in which $\Delta S = 0$ although physically it should be continuous. In fact, these mathematical aspects cause instability in the HB solver, and the subsequent optimization runs. Having said that, Simmons [34] argues that the model works only for small voltages, and another equation is found for higher differences.

However, for the reasons that will be explained in subsection 2.3.4 we are just interested in the realization around zero volt. Luckily, a possible

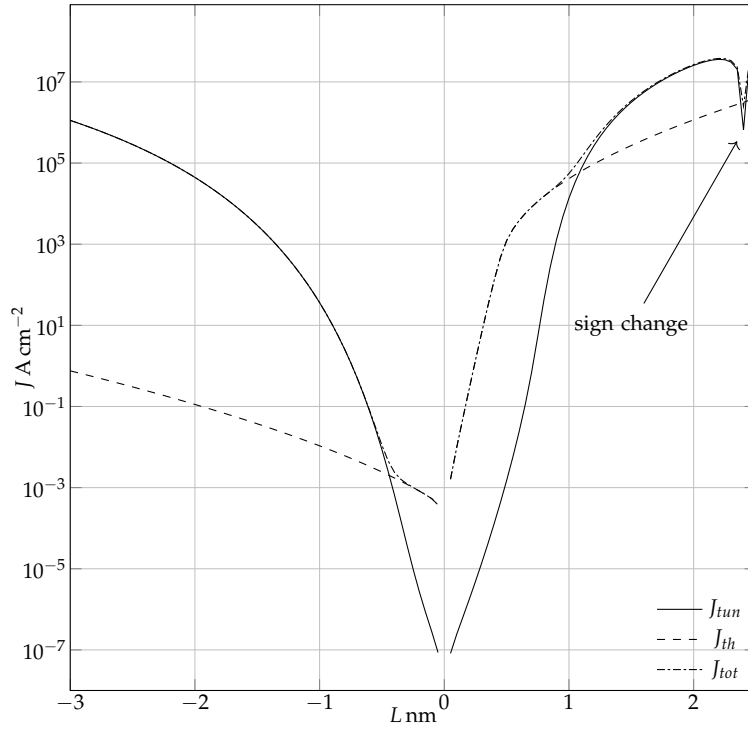


FIGURE 2.13: The $I(V)$ relation according to Simmons model using the parameters shown in Table 2.1. A rapid current discontinuity occurs as shown.

mathematical solution is suggested to limit the HB variation from going too far from the zero point.

Since the HB algorithm tries diverse and high voltage values during the search for a solution, a retro-fitted amendment has been introduced to the model to prevent the algorithm from directly imposing high voltage values on the $I(V)$ model. Equation (2.36) shows the relationship between the imposed voltage level by the HB algorithm - called state variable in the respective literature - and the voltage applied to the $I(V)$ model of the diode.

$$V = \begin{cases} x & : x \leq v_m \\ \tan^{-1}(Gx + D) + \beta & : x > v_m \end{cases} \quad (2.36)$$

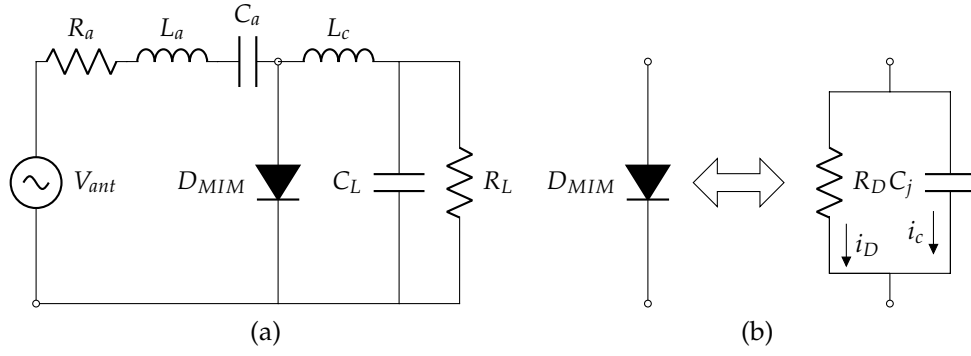


FIGURE 2.14: The THz rectifier equivalent circuit

In (2.36) x refers to the state variable imposed by the algorithm and the values of G , β and D variables are defined as follows:

$$\beta = 2v_m - \frac{\pi}{2} \quad (2.37)$$

$$G = \cot^2(v_m) + 1 \quad (2.38)$$

$$D = \cot(v_m) - (\cot^2(v_m) + 1)v_m \quad (2.39)$$

Where v_m is the value at which the function turns from linear to trigonometric relationship, and it is left to the developer to decide the value that results in the best performance for the algorithm. This amendment is designed such that continuity and derivability is guaranteed in order not to disturb the HB algorithm while solving, it further ensures that the applied voltage never exceeds $\pm 2v_m$ arctangent asymptote. The accuracy of the solution is also not compromised for small voltages because $V = x \forall x \leq v_m$.

2.3.4 Modelled Circuit And Results Discussion

After obtaining the DC response of the diode, an AC analysis of the system performance is important. Before getting to the details of the modelled circuit, we have to identify the expected voltage level at the rectifier input. Given the assumptions explained in section 2.2.2, then a surface whose

temperature is around 100 °C, will have a peak radiation intensity around $f = 30$ THz.

If a dipole is designed to resonate at such frequency, it will have an effective aperture:

$$A_{eff} = 13\left(\frac{c}{f}\right)^2 = 1.3 \times 10^{-9} \text{ m}^2 \quad (2.40)$$

According to Byrnes et al. [30] the earth thermal radiation power density is about $P_{earth} = 70 \text{ W m}^{-2}$ for a range of radiation from 8 μm to 13 μm . Therefore, the available electromagnetic power to the antenna is:

$$\begin{aligned} P_W &= \frac{\Delta f}{37.5 - 23.076} = \frac{\frac{f}{Q}}{37.5 - 23.076} \\ &= \frac{0.3}{37.5 - 23.076} = 1.4 \text{ W m}^{-2} \end{aligned} \quad (2.41)$$

Hence, for a lossless antenna, the available power to the antenna ports (i.e. rectifier input) is:

$$P_A = A_{eff} \times P_W = 1.82 \times 10^{-9} \text{ W} \quad (2.42)$$

The available power to the rectifier input according to (2.42) yields an extremely small voltage variation which has to operate the diode in the non-linear area. It could be argued that an antenna array will resolve this issue. However, according to the discussion made in section 2.2.2, there are limits as to how large an array is useful. Therefore, it is important to overcome the diode turn on voltage level issue to increase the overall efficiency yield of the rectenna system.

Figure 2.14a shows the modelled rectifier circuit on NONLIN [41]. The antenna that receives the radiation is represented by the voltage source V_{ant} oscillating at $f = 30$ THz and its resistive and reactive components are $R_a, L_a,$

and C_a , respectively. The tunnelling diode is referred to by D_{MIM} with the parameters shown in Table 2.1, has an $I(V)$ response as explained earlier, a parasitic junction capacitor C_j corresponding to an area $A_j = 6.35 \times 10^{-9} \text{ cm}^2$, and a parasitic inductive effect of the output leads L_c . The load of this diode is a capacitor C_L and a resistor R_L with values to be identified according to an optimization process. Assuming an almost ideal voltage source with the reactive and resistive values very small and that it has an oscillation amplitude of 20 mV the simulated circuit yields very small power output.

With further investigations it turned out that the diode, whose equivalent circuit is shown in Figure 2.14b, has very unbalanced linear and nonlinear impedance values. That is, while the calculated dynamic resistance according to (2.5) experiences high values as shown in Figure 2.15, the parasitic junction capacitor has a very low value at $f = 30 \text{ THz}$ such that:

$$C_j = \frac{K\epsilon_0 \cdot A_j}{L} = 9.066 \times 10^{-11} \text{ F} \quad (2.43)$$

At $f = 30 \text{ THz}$ the capacitive reactance is:

$$X_C = \frac{1}{\omega C_j} = 5.852 \times 10^{-5} \Omega \quad (2.44)$$

At the same time, the dynamic resistor for this diode around $V = 20 \text{ mV}$ is:

$$R_D = \frac{dV}{dI} = \frac{dV}{Adj} = \frac{36.44}{6.35 \times 10^{-5}} \approx 574 \text{ k}\Omega \quad (2.45)$$

In other words, there is a huge difference more than eight orders of magnitude between the nonlinear tunnelling current i_D and the linear reactive current i_c in Figure 2.14b. Consequently, the exploitation of the nonlinearity as explained earlier happens for just a very small portion of the AC current.

In order to prove this concept, a kind of scaling was done for both values by varying, independently, the surface area A in the $I(V)$ equation and

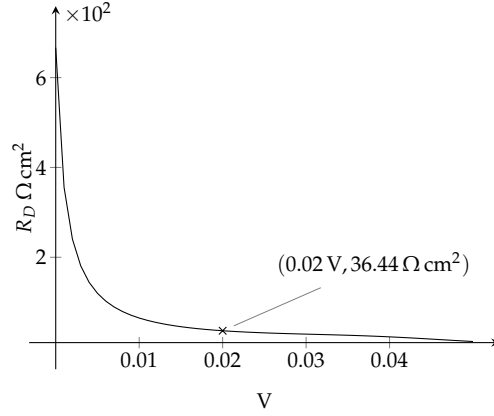


FIGURE 2.15: The dynamic resistance of the modelled diode.

C_j equation to bring them to closer order. Although not physically realizable but points out an important issue. Table 2.2 shows the rescaled R_D and C_j values and the output of circuit optimization targeting load resistance, antenna impedance, and oscillation amplitude. In Table 2.2 a return loss value of 9.17 dB is possible as shown in the highlighted row under these conditions.

Input V_{in} V	Performance		Optimization output*		
	P_{DC} dBm	RL^\dagger dB	R_L Ω	L_a nH	C_a aF
0.02	-7.22	1.71	9.99	3.79	7.49
0.02	9.07	9.17	4.54	4.16	6.81
0.03	8.48	4.69	Almost no change		
0.04	7.90	3.24	Almost no change		
0.05	7.406	2.49	Almost no change		

* After rescaling $R_D = 7.107 \Omega$, $C_j = 74.65$ fF

† Return Loss

TABLE 2.2: Circuit optimization results using a diode with rescaled R_D and C_j values.

the same band of frequency with quality factor $Q = 100$ is used to receive such radiation.

According to the calculation made in (2.44), this diode is structurally limited from operating in the THz range as the linear reactive current is many orders of magnitude higher than the nonlinear component. This limitation

is not for this very case and it actually extends to other MIM diodes as explained by Moddel [12, Chapter 3]. A possible workaround can be to go for multi insulator diodes referred to as MIIM diodes. This would yield twofold benefit as we will get:

- Higher degree of freedom for the oxide layer thickness and substance which will result in more control of the nonlinear current FOM. Hence, improved nonlinearity.
- Lower capacitive effect as two laminated insulators will reduce the capacitor value [92] and so reduce the reactive linear current flow.

Having said that, the dependence of Simmons model on the WKB approach makes it difficult to extend the model to multi-insulator structures. This suggests the use of other computation models even though they would be more complicated and computer intensive.

2.4 Transfer matrix method

2.4.1 Overview

In section 2.3 we have demonstrated the strengths of Simmons model and the shortcomings as for the difficulty to take on new approaches to correct the potential barrier profile. Also, some other models, rather more intricate, have been briefly demonstrated pointing out the difficulty to quickly model the tunnelling phenomenon.

Out of these models, the TMM seems to offer good compromise between accuracy, ease of implementation on computer, and simulation time [37]. In comparison with Simmons model which adopts the WKB approach, the TMM approach is centred upon the potential barrier profile that is sliced into smaller sub profiles. In this piece-wise-like approach the profile nonlinearity

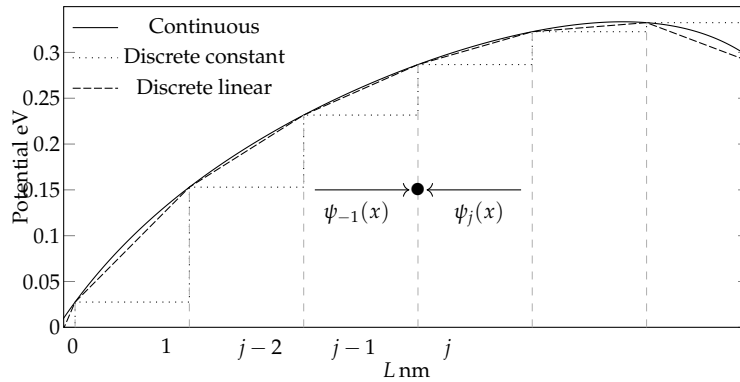


FIGURE 2.16: Continuous, discrete constant, and discrete linear potential barrier profile for the Nb/Nb₂O₅/Au diode example demonstrated in section 2.3.

inside each slice can be approximated by a linear profile without compromising accuracy very much.

In this case, a simpler model for the tunnelling problem described by a transfer matrix is found for each slice. The overall system behaviour is simply the product of these concatenated matrices and the tunnelling current density can be found from the overall tunnelling probability.

The strength of the TMM approach lies in its adaptability to the potential profile regardless of its eventual variations be they caused by substance lattice imperfection, or deliberately made by depositing different material. This makes the model fit for single, double, triple insulator diodes or even if a metal layer is deposited in between. However, there are many versions of the method and they behave differently as we will see shortly.

For example, as shown in Figure 2.16, the continuous potential barrier curve may be approached by a discrete piece-wise linear approach or by a simpler discrete constant approach. While the former approach yields the use of Airy functions [93], [67] it has been noted, that its performance is the same as the simpler constant approach (i.e. the dotted stairs plot in Figure 2.16).

In this section, I will start off laying out the theoretical background for the method. The theoretical background will be used in a fixed mesh technique

and simulation results will be given for a specific MIIM diode structure. In contrast, an adaptive mesh technique will be explained and applied to the same structure to monitor the differences. Finally, a transmission probability comparison between both approaches will be given in order justify the chosen model to adopt for the optimization process that will take place later on.

2.4.2 Transmission Matrix Formalism

The formalism here is based on the assumption made in subsection 2.1.2 when a travelling electron with energy E meets a barrier with a different potential energy V . That is, a *transition* in the potential energy value occurs as demonstrated in Figure 2.16. According to this paradigm, the potential profile is sliced into sub ranges, where inside each range the potential is assumed linear.

As a potential transition occurs between two neighbouring slices, it is important for the wave function to have a physical meaning not only inside each slice, but also at the interface with adjacent slices. And so it should be:

- Continuous at the interface so that it is equal if calculated from the left side or the right side even if it experiences a wave vector (2.11) value change.
- Smooth at the interface so that the derivation of the wave function is equal at both interface sides.

Therefore, based on the continuity condition at x of the $j - 1^{th}$ interface between $j - 1$ and j regions shown in Figure 2.16 one can write:

$$\psi_{j-1}(x_{j-1}) = \psi_j(x_{j-1}) \quad (2.46)$$

Similarly, the smoothness condition when applied leads to the following condition:

$$\frac{1}{m_{j-1}^*} \frac{d\psi_{j-1}(x_{j-1})}{dx} = \frac{1}{m_j^*} \frac{d\psi_j(x_{j-1})}{dx} \quad (2.47)$$

Assuming a general solution as shown in (2.10), the wave function at an interface point can be written as follows:

$$\psi_j(x) = A_j e^{p_j(x_j)} + B_j e^{-p_j(x_j)} \quad (2.48)$$

Where

$$p_j(x_j) = \kappa_j \cdot x_j \quad j > 0 \quad (2.49)$$

$$\kappa_j = j \sqrt{\frac{2m_j^*}{\hbar^2} (V_j - E)} \quad (2.50)$$

Therefore, for the continuity condition the following should be true:

$$A_{j-1} e^{p_{j-1}(x_{j-1})} + B_{j-1} e^{-p_{j-1}(x_{j-1})} = A_j e^{p_j(x_{j-1})} + B_j e^{-p_j(x_{j-1})} \quad (2.51)$$

As $p_j(x)$ is linearly dependent on x , its derivation is simply:

$$p_j'(x_j) = \left. \frac{dp_j(x)}{dx} \right|_{x_j} = \kappa_j \quad (2.52)$$

Based on (2.47) and (2.52) the derivation of the wave function at x_j gives:

$$\begin{aligned} \left. \frac{d\psi_j(x)}{dx} \right|_{x_j} &= A_j p_j'(x_j) \cdot e^{p_j(x)} - p_j'(x_j) B_j e^{-p_j(x)} \\ &= p_j'(x_j) [A_j e^{p_j(x)} - B_j e^{-p_j(x)}] \end{aligned} \quad (2.53)$$

And so, the derivability condition imposes the following:

$$\frac{1}{m_{j-1}^*} \left\{ p'_{j-1}(x_{j-1}) \left[A_{j-1} e^{p_{j-1}(x_{j-1})} - B_{j-1} e^{-p_{j-1}(x_{j-1})} \right] \right\} = \frac{1}{m_j^*} \left\{ p'_j(x_{j-1}) \left[A_j e^{p_j(x_{j-1})} - B_j e^{-p_j(x_{j-1})} \right] \right\} \quad (2.54)$$

Solving both (2.51) and (2.54) such that we isolate A_j and B_j with respect to A_{j-1} and B_{j-1} , the following matrix formula is reached:

$$\begin{bmatrix} A_j \\ B_j \end{bmatrix} = \begin{bmatrix} \frac{(\alpha+\beta)}{2e^{p_j(x_{j-1})}} & \frac{(-\alpha^*+\beta^*)}{2e^{p_j(x_{j-1})}} \\ \frac{(-\alpha+\beta)}{2e^{-p_j(x_{j-1})}} & \frac{(\alpha^*+\beta^*)}{2e^{-p_j(x_{j-1})}} \end{bmatrix} \cdot \begin{bmatrix} A_{j-1} \\ B_{j-1} \end{bmatrix} \quad (2.55)$$

Where

$$\alpha = \frac{m_j^* p'_{j-1}(x_{j-1})}{m_{j-1}^* p'_j(x_{j-1})} \quad (2.56)$$

$$\beta = e^{p_{j-1}(x_{j-1})} \quad (2.57)$$

The aforementioned relationships are mostly represented in the literature in terms of matrices where matrix M has the elements of (2.55) and that:

$$\begin{bmatrix} A_j \\ B_j \end{bmatrix} = \begin{bmatrix} M_{11} & M_{12} \\ M_{21} & M_{22} \end{bmatrix} \cdot \begin{bmatrix} A_{j-1} \\ B_{j-1} \end{bmatrix} \quad (2.58)$$

$$\begin{bmatrix} A_j \\ B_j \end{bmatrix} = \mathbf{M}_{j-1} \cdot \begin{bmatrix} A_{j-1} \\ B_{j-1} \end{bmatrix}$$

In fact most of the literature [46], [67], [94] presents a similar treatment framework to the one done here. The outcome of this approach is a series of transfer matrices multiplied by each other. Assuming a system of N slices, solving the whole system will lead to a relationship between the coefficients at the input of the tunnel A_0 , and B_0 which represent the wave

function in the metal lattice right before entering the tunnel, and the output coefficients A_{N+1} and B_{N+1} at the opposite metal side right after exiting the tunnel. Therefore, the system of equations will look like:

$$\begin{aligned}
 \begin{bmatrix} A_{N+1} \\ B_{N+1} \end{bmatrix} &= \mathbf{M}_N \cdot \begin{bmatrix} A_N \\ B_N \end{bmatrix} \\
 \begin{bmatrix} A_{N+1} \\ B_{N+1} \end{bmatrix} &= \mathbf{M}_N \cdot \mathbf{M}_{N-1} \cdot \begin{bmatrix} A_{N-1} \\ B_{N-1} \end{bmatrix} \\
 \begin{bmatrix} A_{N+1} \\ B_{N+1} \end{bmatrix} &= \mathbf{M}_N \cdot \mathbf{M}_{N-1} \dots \mathbf{M}_0 \cdot \begin{bmatrix} A_0 \\ B_0 \end{bmatrix}
 \end{aligned} \tag{2.59}$$

By solving these equations, an electron having energy E would have a transmission probability from the left to the right metal side as shown in (2.60).

$$T(E) = \frac{\kappa_{n+1} |A_{N+1}|^2}{\kappa_0 |A_0|^2} \tag{2.60}$$

Then, applying the boundary condition on the entire system will help us to minimize the number of unknowns. In other words, to avoid having an infinitely extending wave function in the $+\infty$ direction, we place $B_{N+1} = 0$. Similarly, from (2.60) only the ratio between A_{N+1} and A_0 is interesting and it cannot be any value as the normalization of the wave function is compulsory (i.e. $\int_x \psi(x) \cdot \psi^*(x) dx = 1$).

2.4.3 Current Density Calculation

After solving the matrix system in (2.59), the current density flowing from left to right is the difference between the two currents that flow in opposite

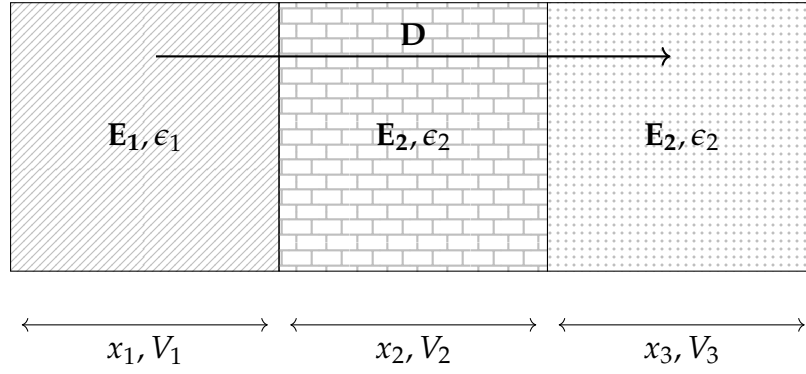


FIGURE 2.17: laminated insulators with different dielectric constants. The potential difference on the structure is subject to the displacement conservation vector \mathbf{D} .

directions. That is, $J(V) = j_{L \rightarrow R}(V) - j_{R \rightarrow L}(V)$ which may be found from:

$$J(V) = \frac{4\pi m_M^* e}{h^3} \int_0^\infty T(E_x) dE_x \int_{E_x}^\infty \{f_L(E) - f_R(E + V)\} \quad (2.61)$$

Where m_M^* is the effective electron mass inside the metal lattice⁵. Equation 2.61 means that the current density is identified by summing up (integral) the current values corresponding to the electrons that have energy E_x and manage to pass the tunnel with probability $T(E_x)$. The *population* of electrons which has this energy is identified by the Fermi distribution function for the left f_L and right f_R metals which is given by (2.62).

$$\begin{aligned} f_L(E) &= \frac{1}{1 + e^{\frac{E - E_{FL}}{k_B T}}} \\ f_R(E + eV) &= \frac{1}{1 + e^{\frac{E + eV - E_{FL}}{k_B T}}} \end{aligned} \quad (2.62)$$

For simplicity, in the aforementioned equations the Fermi level E_{FL} is considered constant even if the right and left metal substances are different. This treatment will be used to calculate the tunnelling current density. In fact, the current calculation remains constant regardless of how we calculate the transfer matrix.

⁵For simplicity, the left and right metals effective electron mass is considered equal in (2.61).

2.4.4 Transmission Probability Calculation Using Fixed Step

As mentioned in the overview, a simplified model using fixed mesh for slicing the potential profile is possible. This mechanism is a good introduction to understand the overall performance of the transmission matrix system. The potential profile equation may be found in a way similar to that done in (2.27), baring in mind that:

- Simmons model assumes a multi-charge effect when calculating the images forces lowering effect which leads to a complicated equation that needs curve fitting. However, as stated in [95] and used in [37], a simpler yet enough accurate image forces lowering model as in Equation 2.63 may be adopted with the impact of just one charge, assuming a good conductive metal in contact with the insulator.

$$V_{IF}(x) = -\frac{e^2}{16\pi\epsilon_0} \left(\frac{1}{\int_0^x \epsilon(\xi)d\xi} + \frac{1}{\int_x^L \epsilon(\xi)d\xi} \right) \quad (2.63)$$

- When two insulators with two different dielectric constants are in contact, the potential value inside each must be normalized to ensure conservation of the electric displacement field \mathbf{D} . In Figure 2.17, the overall potential applied to the structure is:

$$V = V_1 + V_2 + V_3 \quad (2.64)$$

According to Maxwell's equation, the displacement vector inside the insulator should remain constant. In other words, for adjacent insulator layers $E_j \cdot \epsilon_j = E_{j-1} \cdot \epsilon_{j-1}$. Or potential-wise $\frac{V_j}{L_j} \epsilon_j = \frac{V_{j-1}}{L_{j-1}} \epsilon_{j-1}$. Assuming a uniform \mathbf{E} inside each insulator and that $\epsilon_j = \epsilon_0 \cdot K_j$, the following

may be written starting from (2.64):

$$\begin{aligned}
 V &= V_1 + V_1 \frac{K_1/L_1}{K_2/L_2} + V_1 \frac{K_1/L_1 K_2/L_2}{K_2/L_2 K_3/L_3} \\
 &= V_1 + V_1 \frac{K_1/L_1}{K_2/L_2} + V_1 \frac{K_1/L_1}{K_3/L_3} \\
 &= V_1 \frac{K_1}{L_1} \left(\frac{1}{K_1/L_1} + \frac{1}{K_2/L_2} + \frac{1}{K_3/L_3} \right)
 \end{aligned} \tag{2.65}$$

This yields that for each layer we have V_j which is dependent on the dielectric constant K_j and the corresponding layer thickness L_j such that:

$$V_j = (V_{bias} + \Psi_L - \Psi_R) \frac{L_j/K_j}{\sum L_j/K_j} \tag{2.66}$$

It is worth noting that cumulative value of (2.66) is $V_{bias} + \Psi_L - \Psi_R$ where V_{bias} is the bias voltage applied to the structure.

To calculate the potential value $V(x)$ at x assuming an external bias V_{bias} , the linear potential energy drop proportional to x is calculated as shown in (2.67) where x_n refers to the the x value at the interface between the n^{th} (whose thickness is L_n) and $n + 1^{th}$ insulator layers. Applying the aforementioned equations, the potential profile may be found as shown in (2.67).

$$V(x) = \begin{cases} V_{bias} & : x < 0 \\ V_{bias} + \Psi_L - \chi_n - \sum_{j=0}^{n-1} V_j - V_n \frac{x - x_n}{L_n} & : 0 \leq x < L_n \\ 0 & : x \geq L \end{cases} \tag{2.67}$$

Where Ψ_L is the work function of the left side metal, and χ_n is corresponding affinity function. Now that the potential profile is developed for all the structure, taking into account the image forces lowering effect, the total potential is simply the addition of the voltage values in (2.63) and (2.67) as in (2.68). A further clarification of this calculation maybe found in the attached

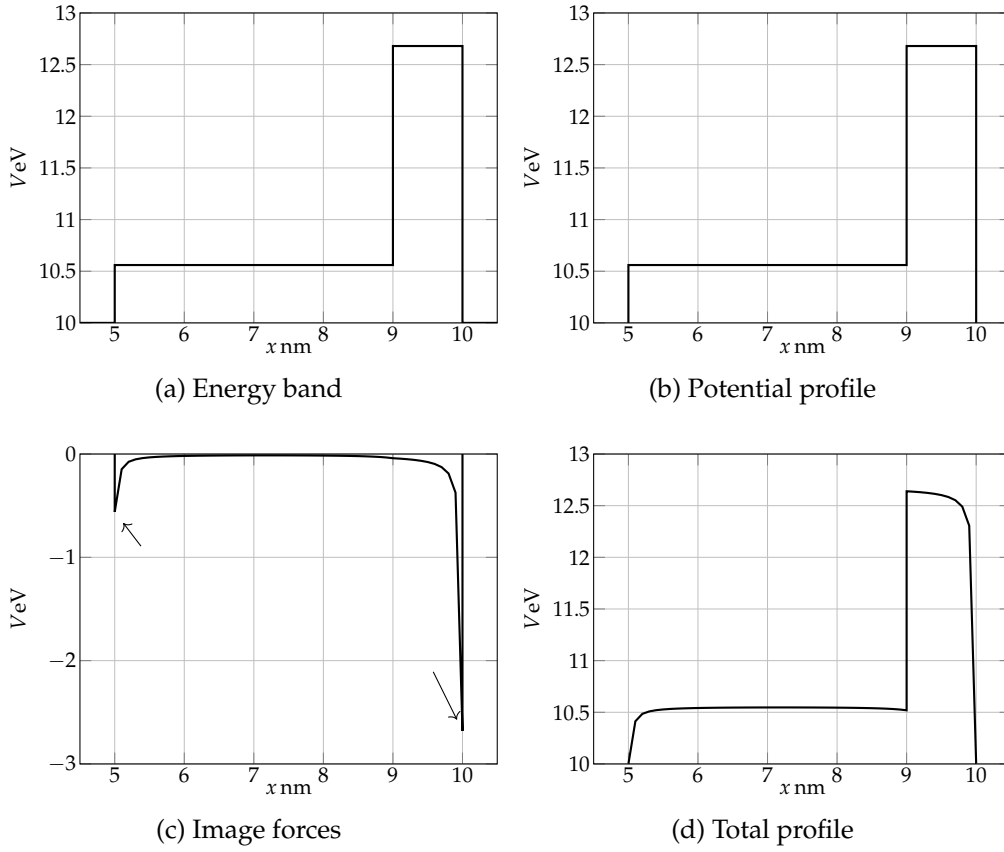


FIGURE 2.18: Energy diagram, potential profile, image forces lowering, and the total potential for a Al/NbO₅/Al₂O₃/Al MIIM diode.

source code in Appendix A.

$$V_{tot}(x) = V(x) + V_{IF}(x) \quad (2.68)$$

Assuming a multi-insulator diode made of Al/NbO₅/Al₂O₃/Al with all the work and affinity function values given in Table 2.3, it is possible to find the potential profile using (2.68), which gives the results shown in Figure 2.18 for a structure under $V = 0$ V potential.

It should be noted, that the image forces solution (2.63) also gives discontinuity right at the interfaces with side metals with value $-\infty$ V. To overcome this issue, it is assumed that the potential cannot go below 0 around the interfaces. When forcing this assumption, a rapid change in the lowering curve

Material	Property	Value
Al	Ψ	5 eV
Nb ₂ O ₅	χ	4.44 eV
	K	25
Al ₂ O ₃	χ	2.32 eV
	K	9.7

TABLE 2.3: Input parameters used for the potential profile calculation.

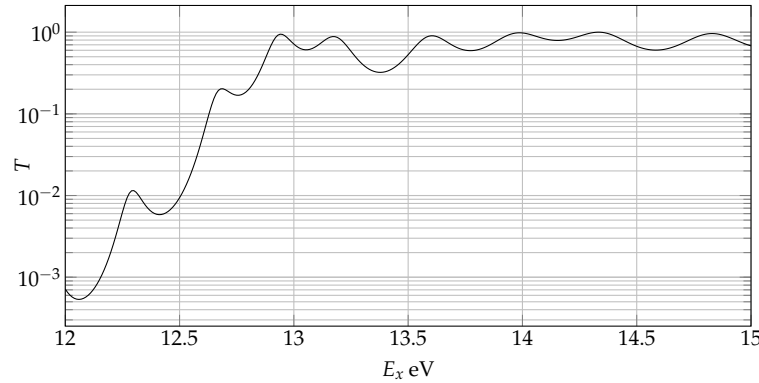


FIGURE 2.19: Tunnelling probability for a Al/Nb₂O₅/Al₂O₃/Al MIIM diode for E_x level ranging from 12 eV to 15 eV.

occurs (as shown with the arrows in Figure 2.18c) such that a minimum zero potential level is guaranteed

Assuming a constant energy step 1×10^{-3} eV to calculate the tunnelling probability $T(E_x)$, the tunnelling probability ranging from 12 eV to 15 eV is found from Figure 2.19.

2.4.5 Transmission Probability Calculation Using Adaptive Step

The demonstrated framework is viable as long as the method gives us accurate results and stable performance. It has been reported in [96], and [97] that the method may experience instabilities. In our case, these are represented by infinitely large numbers or not being able to identify singularities for the matrix effectively. A possible workaround might be as denoted in [98] where

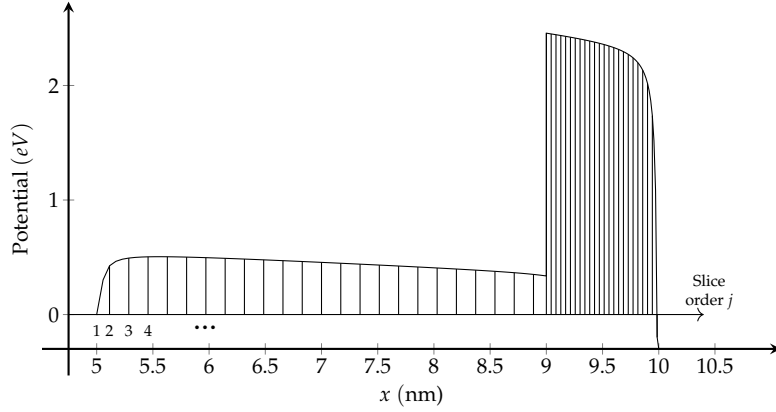


FIGURE 2.20: Potential profile, for an adaptive mesh simulation system for a Al/NbO₅/Al₂O₃/Al MIIM diode.

an adaptive energy step is used based on the ratio of the overall transfer coefficients for two adjacent energy values. The energy step is doubled or halved based on this ratio.

Another issue arises when a too large slice is adopted in the simulation. Probst [99] highlighted two boundary values for the slice thickness such that it should be:

- Small enough where its potential variation is $\propto 1/(dV/dX)$.
- Large enough to ensure a large wave decay proportional to the inverse of κ_j in (2.50).

Figure 2.20 shows how an adaptive mesh looks on the same potential profile presented earlier in Figure 2.18 where the slice width is different between the first and second insulator layer. In fact, solving the same problem using adaptive stepping for both energy integration and slice thickness seems to offer better accuracy in terms of matrix singular values as shown in Figure 2.21.

If relatively large step size = 0.2 nm is used together with $dE_x = 0.01$ eV, the transmission probability function curve is significantly different from the adaptive case. Reducing the energy step size does not seem to approach the all adaptive case.

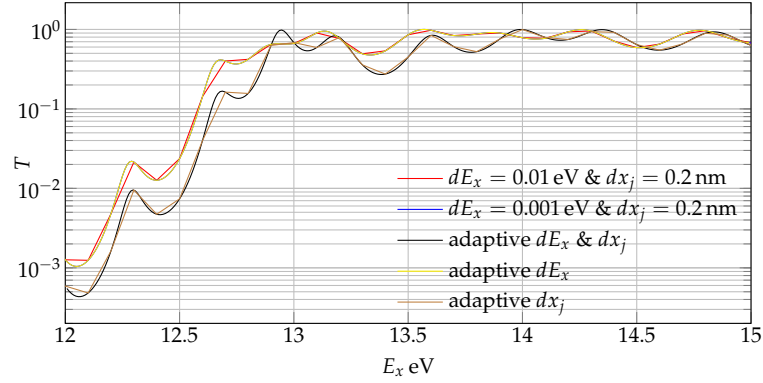


FIGURE 2.21: Tunnelling probability for a Al/Nb₂O₅/Al₂O₃/Al MIIM diode for E_x level ranging from 12 eV to 15 eV using adaptive steps for both the energy level and the potential profile.

On the other hand, hybrid cases, that result from fixing one variable step and adapting the other, behave differently. Fixing the mesh step and adapting the energy step does not significantly change the behaviour with respect to the all fixed case. However, fixing the energy step to $dE_x = 0.01$ eV and adapting the mesh step has a significant closeness to the all adaptive case as shown in Figure 2.21.

Furthermore, while the local maxima/minima are rather synchronised for fixed and adaptive cases for energies up to 12 eV, their behaviour is different for higher values. For example, at 14 eV the adaptive model gives a local maximum while the fixed mesh model almost gives a local minimum.

In the end, assuming the adaptive results as a reference model, they take a lot of time to simulate on a computer which renders considerable difficulty to optimize the structure in a sensible time.

2.5 Structure Optimization

2.5.1 Overview

We have also seen that the use of TMM method enables simulation of multi-insulator tunnelling structures which have manifold advantages as explained

in subsection 2.4.1. Thus, we get enhanced and better controlled nonlinearity, and decreased linearity resulting from the junction series-capacitor effect [92].

In light of that, it would be beneficial to systematically search for the best compromise between the used materials and the best performance as set by the user which can be achieved by an optimization algorithm. In fact, there are many optimization algorithms circulated in the academic literature, out of which I choose the GA because:

- It is a heuristic algorithm that does not depend on the derivative of the objective function to find the solution. This is important because of the complicated and less-predictable dependency of the wave function $\psi(x)$ on a series of integral/differential calculations starting from FOMs, and involving current density integrals, and complex inverse matrix calculations to solve the TMM system.
- The solution space is inherently *discrete* as types of metals and insulators are identified by indexes as well as their thicknesses which are assumed to be multiples of 0.1 nm. This assumption is based on the fact that atomic diameter for metals in many cases exceed 0.1 nm [100].

In this section, I will explain how to implement an automatic two nested loop procedure exploiting the TMM method and the GA algorithm as inner and outer loops, respectively. In the proposed approach, the GA searches for the best solution based on the MATLAB[®] optimization toolbox [101].

The developed program reads a list of possible solution metals and insulators names and parameters, targeted FOM values, their priorities based on a weighting value, and all the necessary information to control the functionality of the GA. The program, then, invokes another set of programs taken from [98] which utilizes the TMM to evaluate the tunnel diode $J(V)$ relationship.

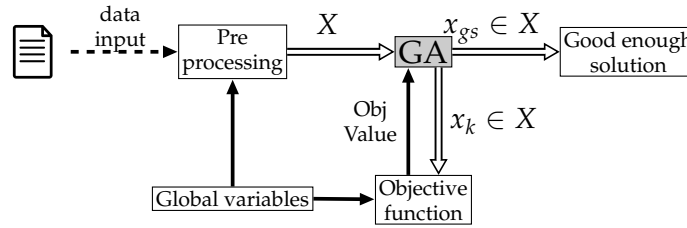


FIGURE 2.22: Schematic diagram of the optimization program used.

Based on the found $J(V)$ all FOMs are calculated as explained later. The novelty here is the introduction of a heuristic optimization technique on the TMM model to search for the best achievable FOM figures based on user's preferences.

2.5.2 System Description

As shown Figure 2.22, the optimizer system is made of several functions which communicate with each other to provide the required information to the GA that searches for the solution. The data is presented to the system in terms of a simple ASCII file. This file contains all the physical parameters needed to run the optimization such as metal work functions, effective mass, insulators electron affinities, dielectric constant, etc.

It is also responsible to define the possible solution space X to search for at least good enough solution.

This solution space is presented to the GA in terms of upper and lower boundary values to search within by the GA. In order to search for the solution the GA throws the k^{th} possible candidate solution to the objective function in the form of a vector $x_k \in X$. The objective function invokes the TMM for every voltage set by the user already imported from the data input file and gets the corresponding current value. The fitness value function is evaluated according to (2.69).

$$C(x_k) = \sum_{p=\{\alpha, \chi, \gamma, R_D\}} w_p \cdot \frac{|tr_p - P_{kp}(x_k)|}{tr_p} \cdot SF_p \quad (2.69)$$

where $C(x_k)$ is the objective function value output for the k^{th} instance, $\mathbb{P} = \alpha, \chi, \gamma, R_D$ is the set of FOMs targeted for optimization which are asymmetry, nonlinearity, responsivity, and dynamic resistance, respectively.

These values are a function of the corresponding voltage. However, the program takes just the maximum value and calculates the corresponding objective function shown in (2.69). For each optimization target $p \in \mathbb{P}$, the function will evaluate the cost by finding the value for the k^{th} instance of the p^{th} FOM $P_{kp}(x_k)$. The cost is simply the normalized absolute difference between the found value $P_{kp}(x_k)$ and the target value read from the optimizer input file tr_p . The contribution of this cost is then weighted by the value read from the optimizer input file w_p . SF_p represents a step function for the p^{th} FOM which always takes the value 1 until the corresponding target is equal to or larger than the target value tr_p (having higher FOM is even better), and so the objective function is minimized. The only exception is the value of the dynamic resistance R_D where SF_p is negated to favour lower resistance values.

The system is built to host for optimization process up to three intermediate layers between the metal electrodes (i.e., MIIIM diode). This necessitates a 9-dimensional space to search in for the solution. In other words, each vector instance x_k has nine components that identify:

1. the number of insulating layers.
2. the left electrode metal identifier.
3. right electrode metal identifier
4. first insulator identifier.
5. first insulator thickness.

6. second insulator identifier.
7. second insulator thickness.
8. third insulator identifier.
9. third insulator thickness.

All the components including thicknesses are integers as stated earlier. Identifiers and number of layers are necessarily integers.

Figure 2.20 shows the reproduced potential profile for the parameters taken from [102] for a Al/4 nm/Nb₂O₅/1 nm/Al₂O₃/Al MIIM diode after applying a 0.3V bias voltage. Evidently, the profile is not equally sliced across the whole range due to the adaptive mesh approach. Also, with respect to [102] the effect of image force lowering causes the chamfered corners of the profile as shown in Figure 2.20. This lowering effect reduces the average barrier thickness that the tunnelling electron has to traverse, and so increases the tunnelling current value subject to the solution of Schrödinger's time-independent equation.

Afterwards, the potential value at each slice interface -with the corresponding thickness of each slice- is fed into the TMM method to find the tunnelling electron transmission probability $T(E_x)$ along x which is used to evaluate the tunnelling current value as explained in subsection 2.4.3. Solving the TMM model is based on near-diagonal square matrix method [99] which is claimed to minimize the rounding errors and provide numerical stability.

2.5.3 Simulation Results

Input Parameters

Tab.2.4 shows two scenarios which have been tried in the process to evaluate the system performance. For each scenario, there is a group of metals which

	Material	Property	Value
Scenario 1	Nb	Ψ	4.33 eV
	NbN	Ψ	4.7 eV
	Nb ₂ O ₅	χ	4.23 eV
		K	25
Scenario 2	Al	Ψ	5 eV
	Nb ₂ O ₅	χ	4.44 eV
		K	25
	Al ₂ O ₃	χ	2.32 eV
		K	9.7

TABLE 2.4: Input parameters used for the GA optimizer.

consists of one or more metals and each metal is represented by its work function value Ψ . Similarly, the scenario also contains a group of one or more insulators which are represented by their electron affinity χ , and dielectric constant K .

The first scenario assumes a single insulator diode formed from niobium nitride NbN, and niobium metal electrodes, and in between a niobium oxide Nb₂O₅ layer is assumed and is based on the parameters used in [37]. The optimizer tries also different thicknesses ranging from 0.1 nm to 3 nm with 0.1 nm step size.

Scenario 2 is for an MIIM diode with aluminium metal electrodes: the choice of metals, insulators, and insulating thicknesses is made by the optimizer to minimize the objective function output.

It should be reported that Ψ and χ values are experiment-dependent and can considerably vary based on the experiment and the interfacing medium and hence can greatly affect the potential profile and the resulting response [37]. Therefore, the values of Scenario 2 have been set to reproduce the same voltage profile in [102] with the thickness varying from 0.8 nm to 2.8 nm with 0.1 nm step.

For each population of individuals the GA tries different combination of metals and insulators chosen from their corresponding groups, and varies

Scenario		α	χ	γ	R_D
1	tr_p	1.3	2.5	$5 V^{-1}$	$3 \times 10^3 \Omega \text{ cm}^{-2}$
	W_p	1	1	1	10
2	tr_p	10	6	$8 V^{-1}$	$500 \Omega \text{ cm}^{-2}$
	W_p	2	5	1	80

TABLE 2.5: Targeted FOM and the corresponding weights used for the GA optimizer.

the thickness of oxide layers in order to minimize the output of (2.69).

The model also adopts the target values tr_p and their respective weights w_p for both scenarios as shown in Table 2.5. The FOMs have been evaluated based on a straightforward approach using difference between subsequent $J(V)$ points to evaluate dJ . This approach results in reducing the number of points by one for each differentiation. When compared to their original values, averaging between successive points have been done to also reduce the number of total points by one.

Using the MATLAB[®] GA toolbox [101] with population size of 30 individuals, function tolerance of 10^{-4} , and elite count 5 for both scenarios provides the results shown in the subsequent section.

2.5.4 Results

In order to calculate the FOM, the equations in [103] are used where the diode junction area can be simplified from the equations of α , χ , and γ and so it is not necessary to have it to calculate them. As shown in Table 2.6 the optimization of Scenario 1 advises to use Nb(NbN) metals for the left(right) electrodes, respectively, with thickness of 2.4 nm of Nb₂O₅.

In order to compare the results, the $J(V)$ curve of [37] has been reproduced using 7th order fitted polynomial. Due to the long time taken for each simulation, the optimized design has been simulated using a voltage range from $-0.3V$ to $0.3V$ with $0.1V$ steps and the resulting $J(V)$ curve shown in

Scenario	Initial	Final
1	NbN/2 nmNb ₂ O ₅ /Nb [37]	Nb/2.4 nmNb ₂ O ₅ /NbN
2	Al/3 nmNb ₂ O ₅ /3 nmAl ₂ O ₃ /Al [102]	Al/2.7 nmNb ₂ O ₅ /2 nmAl ₂ O ₃ /Al

TABLE 2.6: Initial and final states of the GA run for the optimized scenarios.

Figure 2.23 has been fitted by a 7th order polynomial to obtain a simple analytic description of the $J(V)$ relation. Using the obtained polynomials the FOM figures for both cases can be easily reproduced as shown in Figure 2.24.

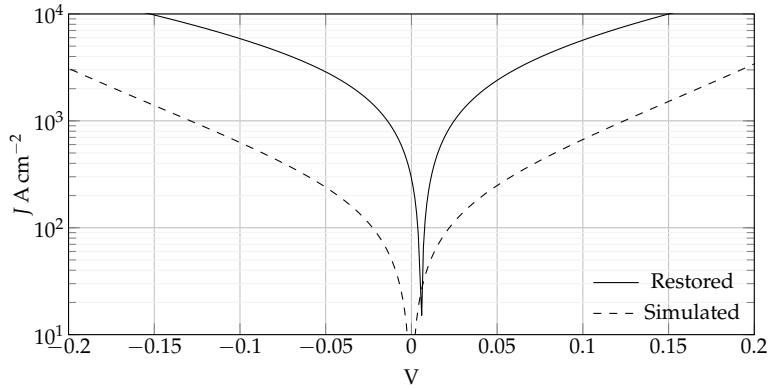


FIGURE 2.23: $J(V)$ response of a Nb/Nb₂O₅/NbN single insulator diode as explained in Scenario 1. Restored curves are reproduced from [37] while the simulated results are the output of the optimization process.

Although the reference case of [37] shows higher current density with respect to the reached model, Figure 2.24 clearly shows improved results both for nonlinearity -which is supposed to be the most important FOM- and responsivity for all the voltage range extending from $-0.3V$ to $0.3V$ except for the values just around zero. This is attributed to the rapid transition between the positive and negative parts. That improvement has been on behalf of reduced dynamic resistance value R_D which significantly increased. Having said that it remained well below the defined target in Table 2.5.

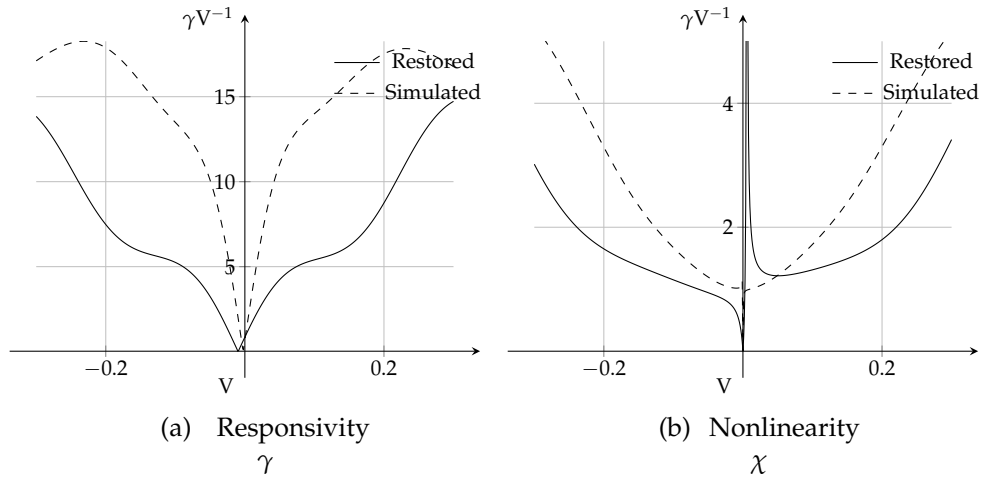


FIGURE 2.24: Responsivity γ and nonlinearity χ FOMs response of a Nb/Nb₂O₅/NbN single insulator diode as explained in Scenario 1. Restored γ and χ curves are reproduced from [37] while the simulated results are the output of the optimization process.

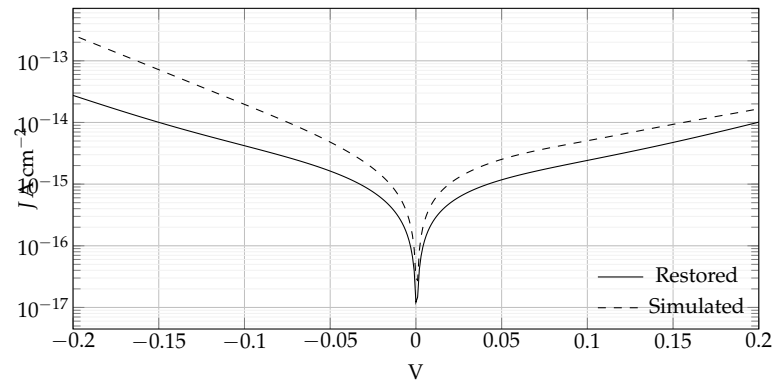


FIGURE 2.25: $J(V)$ response of a double insulator diode as explained in Scenario 2. Continuous curves are $J(V)$ curves of the restored results of [102]. The inset figure shows the solid and dashed curves of the restored response for responsivity γ and nonlinearity χ , respectively.

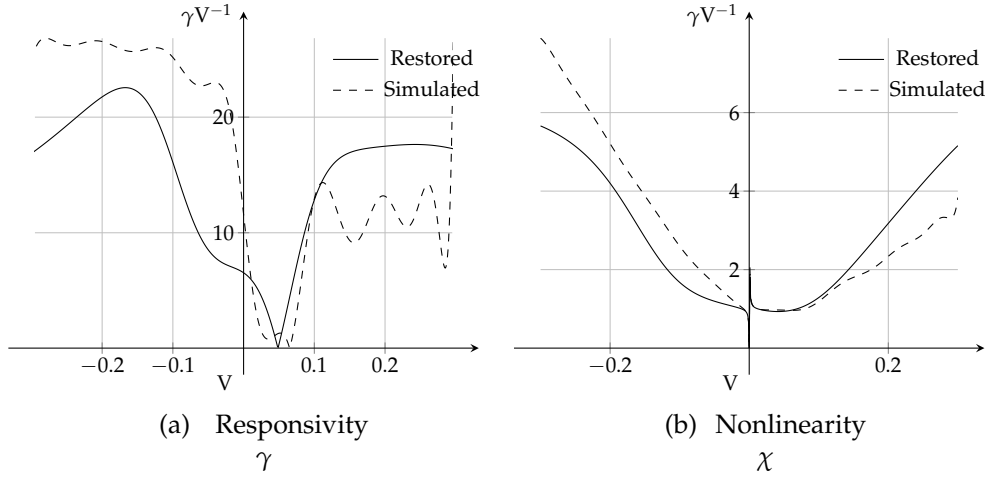


FIGURE 2.26: Responsivity γ and nonlinearity χ FOMs response of a Nb/Nb₂O₅/NbN single insulator diode as explained in Scenario 1. Restored γ and χ curves are reproduced from [37] while the simulated results are the output of the optimization process.

Table 2.6 also shows that the best available result of the optimization of Scenario 2 happens for Al/2.7 nmNb₂O₅/2 nmAl₂O₃/Al example structure taken from [102] which resulted in the curves shown in Figure 2.25. The γ and χ FOM figures show the restored and optimized results for both. For the optimized case, both χ and γ show significant ripples in the positive halfFigure 2.26. Responsivity of the restored curve and the optimized case are of the same order of magnitude.

Although the restored case shows noticeably higher γ in the positive half between 0.15 V and 0.25 V, the optimized case experiences ripples with a varying γ between 6 and 20 V⁻¹. Both γ and χ values of the optimized case are higher in the negative half.

It is worth noting that the high difference in current densities between Scenario 1 and 2 may be attributed to the suboptimum choice of materials and their thicknesses.

2.6 Conclusion

In this chapter the generic mathematical framework used to analyse the receiving part of the rectenna has been introduced together with a literature review of utilisable models for rectifying devices. According to the literature review the following is reported:

- It is important to treat rectifiers differently according to the operation frequency. For higher frequencies not only the rectification semiconductor physics are different, but also the propagation type in addition to the emitted radiation. For example, emission in THz range takes a spontaneous mode for frequency, phase and polarisation as opposed to the more controlled GHz transmission.
- Many theoretical models have been presented in the hope to explain the rectennas operation in the THz range. The variation of models leads to variation of expected results. Furthermore, the device operation may be explained by more than one theory as in the case of Fumeaux et al. experiment [18].
- Generally speaking, quantum models used to describe devices operation at higher frequencies are computer intensive, and a compromise is required between the model accuracy and its temporal performance. Some limitations may also apply to the valid model based on the type of the device to be simulated. Simmons model, for example, is applicable only to one-layer tunnelling diodes.

Based on the developed computer models and the literature review Simmons model seems to be a less complicated approach to analyse the quantum tunnelling current since it involves a much easier calculation method if compared against QTBM [68], NEGF, or [71]. However, the model undergoes instability and/or discontinuity issues when large voltage variation is imposed

by the solver and this will certainly make optimizing algorithms complain. Although the instability issue can be avoided by deploying the approach in (2.36), there is little benefit of doing so.

Back in the time, the WKB approach was an efficient way to understand tunnelling probability and the resulting current. In fact, the expected behaviour of the $I(V)$ curve found by Simmons goes along the lines of experiments but does not give similar or equal results. This has been confirmed by the findings of [58], [36], and [104] as they always perform a curve fitting to get equal results to theory.

Interestingly, Singh et al. [104] have found that the fitted values of ϕ_1 and ϕ_2 are different from what we get from measurements. However, the fitted and the measured barrier height difference, that is $\phi_1 - \phi_2$, remains constant. These findings suggest that the potential barrier model, in addition to the WKB approach, do not address the tunnelling mechanism perfectly. They also indicate the impact the barrier profile has on the device performance.

As noticed from the potential profile in Figure 2.12 that the continuity about the metal-junction interface is disputable. Technically, there has been some trials to improve the model accuracy by addressing a more rigorous potential barrier profile.

In his Master's thesis, Koppinen [105] tries a rigorous mathematical framework to improve the performance of this model, but the resulting model also needs curve fitting to experimental results. In which case, there is little point of optimising this model. The reason for this behaviour, as suggested by Koppinen, is the unphysical divergence of the barrier at the metal surface. Albeit the model he presents overcomes the discontinuity problem, it still needs curve fitting.

Grover & Modell [37] state that the WKB approach gives different results with respect to other approaches at lower barrier heights. In other words, the simplification of the potential barrier formula with just image lowering

effects included, does not reflect on a realisable tunnel in the real world as the impurities and/or oxide lattice imperfections would yield many potential barrier variations which can give rise to intermediate states within the barrier itself (i.e. Resonant Tunneling (RT), Step Tunneling (ST), etc.). And so, an amended and more flexible barrier modelling is beneficial.

The simulation results shown in Table 2.2 reveal the difficulty to deploy MIM diodes at high frequencies as the linear junction capacitor will be very large and will allow a linear current to flow much higher than the nonlinear current. The result is, clearly, a deteriorated performance. This justifies why using multi-insulator diodes would bring forward many benefits as discussed. In which case, the Simmons models will be incapable of modelling MIIM structures.

Although the model has many drawbacks and is kind of dated, it is still quite frequently cited in the literature. It is usually used as a reference model to compare to other more complicated models, in addition to its relative simplicity to understand how would the $I(V)$ response of a MIM diode look like.

With respect to Simmons model, the TMM model features great flexibility in terms of tolerance to potential profile variation, and so makes the performance of the model superior to that of Simmons which only accepts single barrier modelling. Moreover, the possibility to change the material effective mass m^* , slice thickness dx , and energy step dE_x opens up many degrees of freedom to the model.

However, it yields a try and error approach to choose the best coefficient values for the calculations. As a result, $T(E_x)$ is also changed as shown in Figure 2.21 where introducing larger slices makes the program run much faster at the expense of accuracy. The matrix singularity solutions are affected by this step sizing such that they are shifted on x axis. Therefore, there is a trade off between performance and accuracy to solve the TMM system.

In the optimization phase, as will be explained later, reaching a *good enough* solution has taken several days on a single machine to get the final result using MATLAB script. This necessitates reconstructing -at least the time consuming- scripts such that more care is taken about program profiling in order to minimize the time taken to do the computer-intensive calculations such as inverse complex matrix calculation.

In this work a software framework which can be useful for subsequent industrial steps has been presented. Although empirically expecting the value of responsivity for MIIM diode is possible based on estimated potential profile, taking account of many FOMs and the best decision making approach is difficult to reach using simplified approaches.

With the presented technique the user can set the desired FOM values and their respective weights and let the GA look for the qualified solutions. The double insulator would possibly offer better results with respect to single insulator structure when using proper materials and thicknesses. The obtained optimization results have shown significant improvements in the case of a MIM diode and limited ones in the multi-insulator case.

However, these results represent a first trial by just varying the insulator thicknesses with a limited set of metals and insulators. By increasing the number of these design parameters, reaching improved design and performance is more probable.

The program now looks for the maximum FOM value achieved in a specific voltage range: for future releases, the user might wish to be more specific and optimize a FOM at a specific voltage point, thus having a more agile analysis.

Chapter 3

Transmitting Part

3.1 Preface

As already demonstrated in chapter 1 there are many demanding requirements for the new generation of multi-sensor networks and the IoT due to rapid growth of their penetration rate, and the necessity to power up many devices ubiquitously in a feasible manner. In order to achieve this goal the necessity to design efficient power rectifiers has also been demonstrated. As shown in chapter 2, there is less control over natural thermal radiation sources as they are subject to black body radiation law. However, for lower frequencies, there are some novel techniques which have recently earned more attention and can be quite helpful in terms of saving transmitted energy without minimising the energy received at the receiver side.

In this chapter I will first justify why it is important to, also, optimize the energy harvesting problem from the transmitter side, laying out the relevant mathematical framework involved in the novel techniques. Therefore, the TMA mathematical formalism will be demonstrated in the next section to clarify the procedure that will take place in the co-simulation of a nonlinear tunnelling system designed at 28 GHz. Then, a comparison with an earlier experiment at a lower-frequency TMA system will be shown in order to draw conclusions on the aspects of this system. In the following chapter, a brief theoretical background of the FDA system will be also showcased to focus on

f GHz	Distance r m		
	2	4	8
2.4	-41.07	-47.07	-53.07
5	-47.45	-53.47	-59.49

TABLE 3.1: P_R/P_T in dB for various spaces and frequencies

the distance-dependent behaviour of the radiation pattern and how this may be deployed to maximize the beam efficiency ratios (3.2) as will be identified later.

3.2 RF Link Power Losses

The propagation problem between Tx and Rx in a real world example might be very complex to accurately analyze using typical ray-tracing or full-wave analysis [106]. However, the justification why it is important to look for more intelligent power transmitters is straightforward and can be based on the expected power loss in free space according to Friis formula shown in (3.1).

$$\frac{P_R}{P_T} = \cdot G_R G_T \left(\frac{c}{4\pi f r} \right)^2 \quad (3.1)$$

Where P_R , P_T refer to received and transmitted power, respectively, using antennas whose gains are indicated by G_R and G_T . The formula also shows the frequency-dependent behaviour of the received power.

As a simple example, assuming a scenario made of two dipole antennas working in the far field region with gains $G_T = G_R = 2.5$ dBi at frequencies $f = 2.4$ GHz and 5 GHz the Friis formula of (3.1) gives the P_R/P_T ratios shown in Table 3.1 when the space varies between 2 m and 8 m.

A rapid decrease in the received power level about ten thousand times happens just at two meters distance from the transmitter. The situation is even worse for larger distances or higher frequencies.

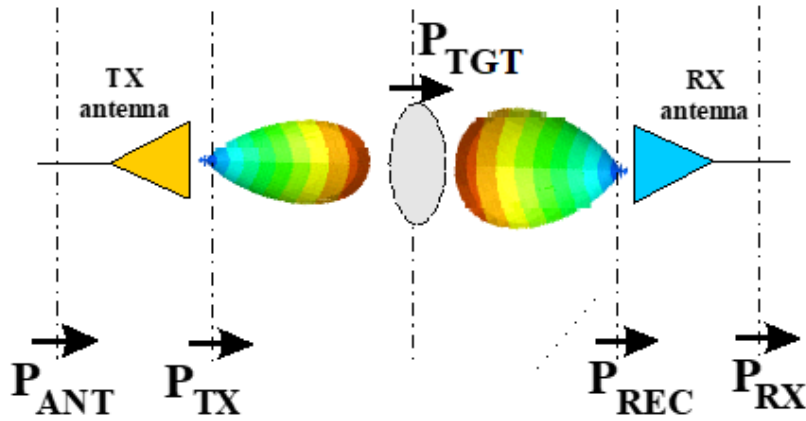


FIGURE 3.1: Details of the wireless link with the involved power contributions. (Reprinted by permission from John Wiley & Sons: [107].)

In other words, an energy harvesting system will lose an enormous amount of power at just two-meter-distance due to the free space loss. The problem happens because the transmitter *blindly* illuminates all the space between itself and the receiver where no deployment of energy occurs in between. Therefore, a system that overcomes this distance restriction is highly desirable. To address this issue some efficiency figures, based on the graphical representation in Figure 3.1 may be introduced.

As shown in Figure 3.1, the Tx and Rx antennas' capability to effectively radiate reduces the actual wirelessly-transmitted and received powers to P_{TX} and P_{RX} , respectively. This reduction is usually referred to *radiation efficiency* of the antenna and would remain out of the scope.

On the other hand the efficiencies shown in (3.2) focus only on the power flux in the radiation medium. The first one, named beam transmission efficiency, represents the capability of the radiating system to focus the power in the region where the target receiving rectenna is.

The *mediating* targeted power is referred to by P_{TGT} . The second factor, named beam reception efficiency, takes into account the aptitude of the receiving antenna/array to efficiently deploy the power made available by the RF source.

$$\begin{aligned}\eta_{TX,beam} &= \frac{P_{TGT}}{P_{TX}} \\ \eta_{RX,beam} &= \frac{P_{REC}}{P_{TGT}}\end{aligned}\tag{3.2}$$

A possible workaround for the issue is beam steering which can save a great portion of RF energy. However, the *linear* circuitry involved in the steering process is not easily designed and will suffer from considerable losses [108]. Therefore, a novel technology that can provide simple and less power-hungry solution is highly desirable for future applications.

The TMA and FDA novel solutions presented in this chapter address both issues. As it will be explained later, the TMA technique exploits a mathematical trick to control the array input signals in the time domain to produce a similar effect to that of typical phased arrays in a way that no losses occur in the input signal control circuitry. The FDA, controls the frequency and phase of the array input signal such that a *distance-dependent radiation pattern* of the antennas may be obtained.

In the following section, I will introduce the mathematical framework of the TMA system demonstrating the important equations that explain its behaviour and how it can be integrated with a circuit simulator to have a co-simulation for the linear and nonlinear parts of the system.

Focusing mainly on the 28 GHz case, I will demonstrate the output of some simulations and measurements done for the array.

In the subsequent section, I will explain the FDA theory and how the inclusion of this technique in a more realistic co-simulation scenario has led to promising results. In the end, I will focus on the possible future work areas and challenges to be addressed to realize such system.

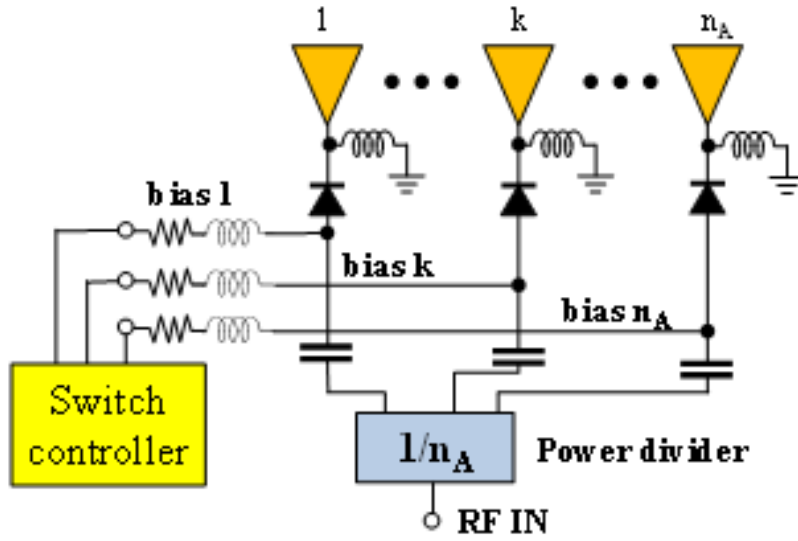


FIGURE 3.2: Schematic representation of a linear n_A element TMA. [109]©[2018] IEEE

3.3 Time-modulated Arrays

3.3.1 Mathematical Formalism

Let us consider the circuit described in Figure 3.2, where a linear TMA with n_A antennas is reported. This circuit can be described by its steady-state regime under sinusoidal excitation, by means of a set (say n_H) of harmonics of the fundamental angular frequency ω_0 .

The n_A -dimensional vector of the excitation currents at the feeding points of the n_A antennas can be represented in the form:

$$\mathbf{i}_A(t) = \text{Re} \left[\sum_{k=0}^{n_H} \mathbf{I}_{A,k} e^{jk\omega_0 t} \right] \quad (3.3)$$

It is known [110] that for an array with n_A antennas, the E far-field value at a point (r, θ, ϕ) given that the excitation signal has frequency ω_0 , can be given by (3.4). This result comes from the exploitation of both the linear behaviour of the array and the time-invariant vector $\mathbf{I}_{A,1}$ representing the currents at the fundamental frequency ω_0 (for which $k = 1$) entering the

antennas ports.

$$\mathbf{E}(r, \theta, \phi, \omega_0) = \frac{e^{-j\beta r}}{r} \sum_{i=1}^{n_A} \left[\hat{a}_\theta A_\theta^i(\theta, \phi, \omega_0) + \hat{a}_\phi A_\phi^i(\theta, \phi, \omega_0) \right] \mathbf{I}_{A,1}^i \quad (3.4)$$

where β is the free-space phase constant, $\mathbf{I}_{A,1}^i$ the excitation current at the generic i^{th} antenna port at the fundamental frequency ω_0 at $k = 1$, A_θ^i and A_ϕ^i are the scalar components of the normalized field. Such components are generated by full-wave simulation of the whole array with only the i^{th} antenna excited by a unit-current sinusoidal source of angular frequency ω_0 .

The implication of (3.4), is that the far field radiation pattern of the antenna need not to be created every time a new excitation current array $\mathbf{I}_{A,1}^i$ is available. Just one copy of the radiation pattern can be reused to obtain the new radiation pattern corresponding to new excitation currents. This justifies why an *offline* co-simulation for the linear part is valid.

In the case of a TMA radiating nonlinear system the regime is given by a modulated RF drive, because there is the superposition of the sinusoidal carrier ω_0 and the slow (with respect to the RF) modulation law of the switches, that are periodically (with period $T_M = 2\pi/\omega_M$) biased. In this case the currents feeding the antennas become time-dependent currents $\mathbf{I}_{A,1}^i(t_M)$ that can be given by (3.5).

$$\mathbf{I}_{A,k}(t_M) = \sum_{h=-\infty}^{+\infty} \mathbf{I}_{A,kh} e^{jh\omega_M t_M} \quad (3.5)$$

Where k is the harmonic order with respect to the carrier oscillation frequency, h^1 is the harmonic order of the modulated excitation current. The input current vector thus becomes dependent on two time-bases, the fast

¹ h in this chapter is, obviously, not the same as the h in the chapter 2 which refers to Planck's constant

carrier time t and the slow modulation time t_M , and assumes the expression given in Equation 3.6.

$$\mathbf{i}_A(t, t_M) = \text{Re} \left[\sum_{k=1}^{n_H} \mathbf{I}_{A,k}(t_M) e^{jk\omega_0 t} \right] \quad (3.6)$$

The modulation is obviously transferred from the driving currents to the radiated far field. The time-dependent far-field envelope may be now computed for any modulation speed by the general convolution algorithms [111]. However, based on the assumption of slow variation of the excitation, the resulting \mathbf{E} field radiated at the fundamental frequency $k = 1$ can be expressed as follows (3.7) [110].

$$\mathbf{E}(r, \theta, \phi, \omega_0) = \sum_{i=1}^{n_A} \mathcal{E}^i \mathbf{I}_{A,1}^i(t_M) - j \sum_{i=1}^{n_A} \left. \frac{\partial \mathcal{E}^i}{\partial \omega} \right|_{\omega=\omega_0} \frac{d\mathbf{I}_{A,1}^i(t_M)}{dt_M} \quad (3.7)$$

$$\text{Where: } \mathcal{E}^i = \hat{a}_\theta A_\theta^i(\theta, \phi, \omega_0) + \hat{a}_\phi A_\phi^i(\theta, \phi, \omega_0)$$

The field intensity shown in (3.7) represents the time waveform, which can be also introduced using the AF representation. By referring again to the TMA architecture of Figure 3.2 where the elements of the array are aligned along the direction $\hat{\mathbf{a}}$ ($\hat{\mathbf{a}} \cdot \hat{\mathbf{r}} = \cos(\chi)$), the far-field can be represented as in (3.8):

$$\begin{aligned} \mathbf{E}(r, \theta, \phi, t_M) &= \mathbf{E}_0(r, \theta, \phi) \sum_{i=1}^{n_A} \Lambda_i U_i(t_M) e^{j(i-1)\beta L \cos \chi} \\ &= \mathbf{E}_0(r, \theta, \phi) AF(\theta, \phi, t_M) \end{aligned} \quad (3.8)$$

where \mathbf{E}_0 represents the far-field radiated at the carrier frequency f_0 by the base-element of the array, and the RF switch at the i_{th} antenna port is driven by a periodical sequence of rectangular pulses of period $T_M = 1/f_M$ and normalized amplitude $U_i(t_M)$. In this way, the standard constant excitation coefficient Λ_i of standard arrays is replaced with the corresponding time-dependent version $\Lambda_i \cdot U_i(t)$.

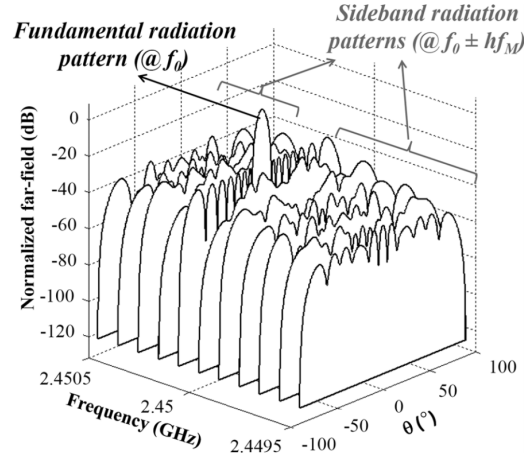


FIGURE 3.3: Frequency-dependent radiation pattern with harmonics $f_0 \pm hf_M$ for a 16-element linear TMA [112] © [2016] IEEE.

This leads to a time-dependent AF whose frequency-domain representation using Fourier transformation is shown in .

$$AF(\theta, \phi, t_M) = \sum_{h=-\infty}^{+\infty} e^{j2\pi(f_0+hf_M)t_M} \sum_{i=1}^{n_A} \Lambda_i u_{hi} e^{j(i-1)\beta L \cos \chi} \quad (3.9)$$

where u_{hi} is the h^{th} Fourier coefficient of the $U_i(t_M)$ pulse.

The direct consequence of the replacement of (3.9) in (3.8) is the multi-frequency radiation contribution: indeed, the TMA is able to radiate at the usual fundamental frequency f_0 ($h = 0$), but also at the near-carrier sideband harmonics $f_0 + hf_M$ with ($h = \pm 1, \pm 2, \dots$) as shown in Figure 3.3. This sideband radiation is efficiently transmitted/received due to the low value of the modulation frequency f_M with respect to the carrier f_0 (MHz vs. GHz), which allows the array elements to be still acceptably resonant.

3.3.2 Co-Simulation of TMA

The TMA simulation approaches available in literature typically focus on the goal of the control sequences optimization, but limit the analysis to the case

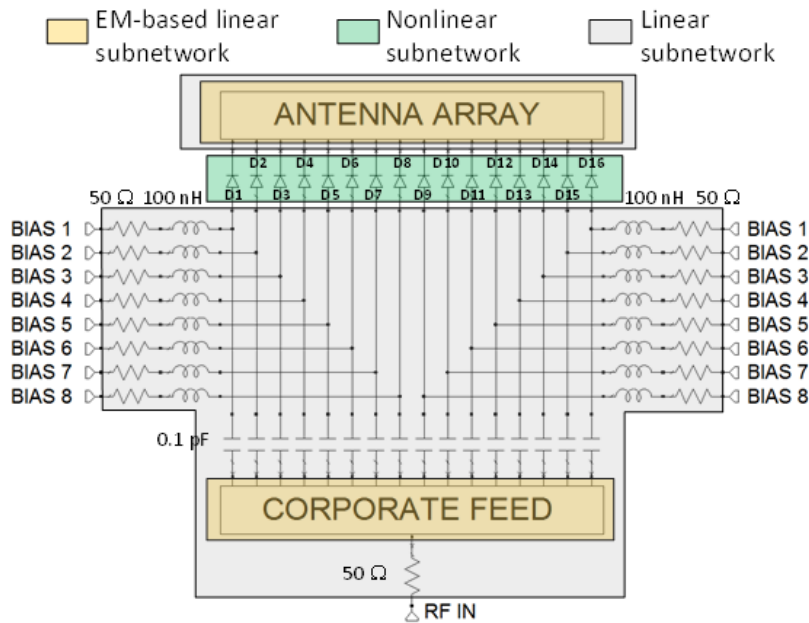


FIGURE 3.4: A system made of linear elements (shadowed in grey and yellow) and nonlinear diodes (shadowed in green)[110]©[2013] IEEE.

of both ideal radiators and ideal switches. As described in the previous section, the nonlinear behavior of TMA systems is quite complex, because of the bi-dimensional regime, the unavoidable presence of EM couplings among the radiating elements and the nonlinear nature of the driving switches: neglecting these effects can lead to highly inaccurate results. For this reason, a rigorous approach for the accurate modelling of the TMA regime accounting for all the non-idealities and the actual system dynamic is needed. In this section we adopt the simulation tool described in [110], so that it will be briefly recalled for the sake of completeness.

The approach consists of the nonlinear/EM analysis of the whole radiating system through the combination of HB technique [111], for the time-based description of the nonlinear switches, and the full-wave simulation of the array and its feeding network in the frequency domain. By referring again to the array with n_A ports of Figure 3.2, with an equal number of switches, the EM-based description of the system consists of a $n_A + 1$ -port

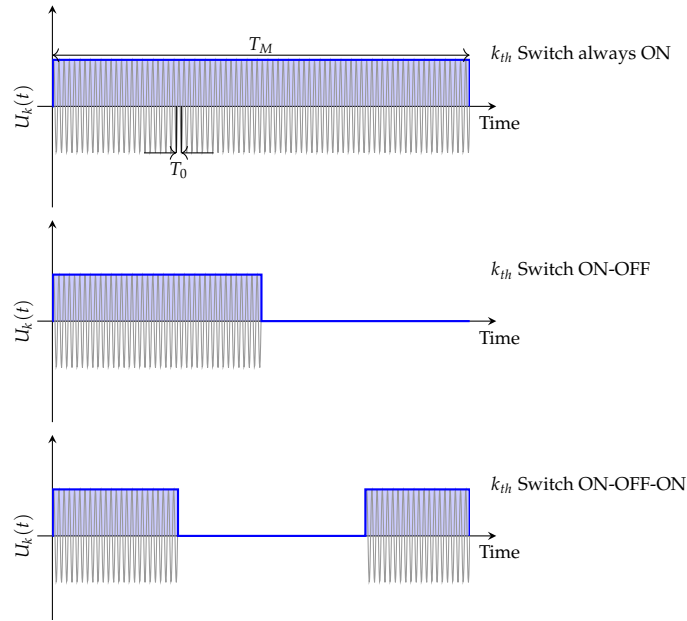


FIGURE 3.5: Examples of periodical switches excitation sequences (in blue), modulating the RF carrier waveforms (in gray), for three different switching patterns [112].

network (including the RF input port), with n_A internal ports for the inclusion of the switches circuit-model: each internal port consists of a couple of floating nodes directly connected to the mesh of the EM simulator. Figure 3.4 shows a similar case where the 16-element antenna array together with other linear elements for the linear part while the on/off diodes form the nonlinear part.

Figure 3.5 shows three possible periodic switch controls: the superposition of the slow switch modulation to the fast carrier frequency f_0 to be radiated, allows to resort to the modulation-oriented HB method [111] leading to (3.4) and (3.8) for the feeding currents and the radiated field, respectively. One can note that the condition $f_0 \gg f_M$ is always valid in practical TMA applications (GHz vs. a few MHz): hence, the modulated regime can always be seen as a sequence of slowly-changing unmodulated ones.

The direct application of (3.4) provides the field envelope at the desired harmonic (typically the fundamental, $k = 1$), in any direction of radiation.

Hence, from (3.4), the far-field harmonics of the bi-dimensional regime due to the intermodulation between f_0 and f_M are available, too, and the far-field can be also represented by their superposition as in (3.10).

$$\mathbf{E}(r, \theta, \phi, t_M) = \sum_{h=-\infty}^{h=+\infty} \mathbf{E}_h(r, \theta, \phi) e^{jh\omega_M t_M} \quad (3.10)$$

This approach allows to have any kind of result in terms of radiated far-field: by varying the harmonic number h in (3.10) and plotting the corresponding \mathbf{E}_h magnitude, the far-field spectrum around the carrier harmonic $k = 1$ is obtained, for a given distance/direction. Alternatively, by varying (θ, ϕ) and plotting again the \mathbf{E}_h magnitude, the radiation surface/pattern at a given distance r and for a given harmonic is available.

It is worth noting that this approach directly investigates the nonlinear nature of the TMA system while radiating.

3.3.3 Millimetre Wave Agile TMA System

As demonstrated in chapter 1 to meet the requirements of the evolution of 5G communication systems and IoT applications, the focus is not only on improving the information throughput, but also on power supply by these devices [113]. Today, the wireless power transfer in the high GHz band and Millimetre Wave (mm-wave) looks to draw a lot of attention thanks to the unlicensed GHz bands, which can be also used for power transfer [114]. However, moving up towards the mm-wave band places stringent constraints on the response time of the active devices used as well as on free-space loss. To provide all these requirements the circuitry should offer:

- fast response time to cater for the rapid oscillation of the mm-waves.
- the ability to direct the RF power into the required direction.

The proposed solution deploys a MIM tunnelling diode as the on/off switching device integrated in the structure together with the 16-element circular patch array. The whole system will be co-simulated using a HB simulation platform where the Simmons model as explained in section 2.3 is used together with specific amendments to facilitate and stabilize the solution finding process. The simulation output is explained and the obtained results are presented to analyse the system behaviour and find out possible areas of interest for future work. The use of this approach offers two benefits:

- it offers real-time response and requires less power, to drive the beam-forming circuit than the classical solution known in the literature [115].
- the proposed circuit is directly implemented as a built-in solution on the circuit board which can be realized as a System on Chip (SoC).

The Nonlinear Diode Device

The importance of integrating Simmons model [39] directly in the nonlinear HB platform comes from the possibility to reach an optimized nonlinear system which can perform much better than if each part has been optimized alone. The HB nonlinear simulator offers this possibility, hence it has been further amended to deploy Simmons model directly into the optimization iteration rather than using a curve fitted procedure. Using a tunnelling device instead of a Schottky diode is justified by their potentiality to work under much higher frequencies in addition to the significant $I(V)$ response offered by highly-nonlinear devices. Also, the good response time may overbalance the problem of MIM diode limited power when used with antenna arrays with many elements.

The diode used in this model is a Nb/Nb₂O₅/Pt MIM diode with a 3 nm niobium oxide insulator. The large difference for the barrier height at both sides of the insulator gives rise to high asymmetry $\alpha = \frac{I^+}{I^-} \Big|_{v=0.5} \approx 10^5$, which

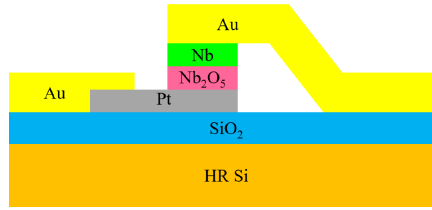


FIGURE 3.6: Schematic cross-section of the proposed Nb/Nb₂O₅/Pt MIM diode and its integration with the transmission line.

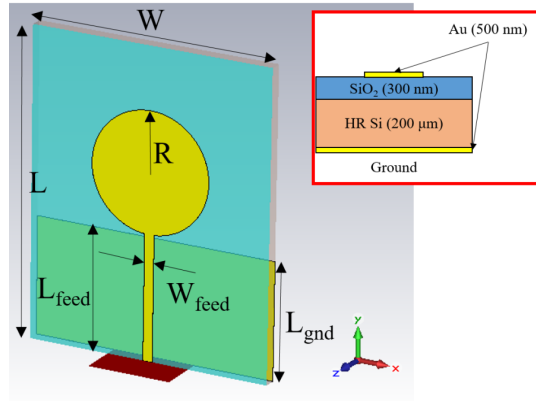


FIGURE 3.7: EM design of the 28 GHz single monopole as array element for the proposed TMA. In the inset, a cross-section of the structure is provided [109] © [2018] IEEE.

corresponds to the voltage level for a perfectly-matched circuit at 5 dBm level, hence approaching the behaviour of a Schottky diode. The $I(V)$ curve behaviour is generated based on the Simmons model using the curve fitted barrier heights found out by Chin et al. [39], and the proposed structure is shown in Figure 3.6.

From a technological point of view, the integration of the Nb/Nb₂O₅/Pt MIM diode can be achieved as depicted in Figure 3.6 such that the low-roughness (around 1 nm) Pt layer (with a thickness of about 20 nm) is deposited by sputtering directly on the SiO₂ layer and patterned to provide the MIM bottom electrode in the desired shape. The Nb/Nb₂O₅/Pt insulator film is, then, grown using an anodization process. Finally, the Nb top electrode (with an average surface roughness of 2 nm and a thickness of 90-100 nm), is deposited using lower sputtering powers and pressures. In the

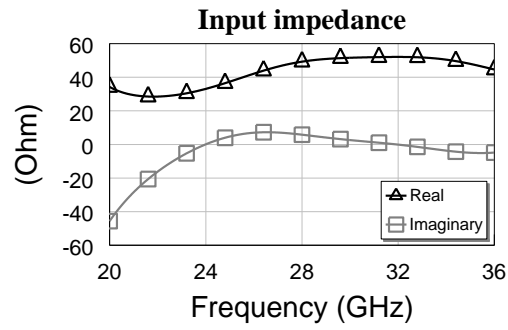


FIGURE 3.8: Simulated input impedance of the 28 GHz single monopole.

final step, MIM electrodes are connected to the gold metallization constituting the transmission line signal (deposited by sputtering), in order to provide the necessary electrical contact.

The Simmons model should be used under limited biasing levels to prevent the exponential terms from growing large as shown in subsection 2.3.3. Since the HB algorithm tries diverse and high voltage values during the search for solution, a retro-fitted amendment as demonstrated in (2.36) has been introduced to prevent the HB algorithm from directly imposing high voltage values on the $I(V)$ model.

16-Element Array for TMA

The proposed TMA is based upon a 16-element array of circular monopoles, designed in CST Microwave Studio[®], as it will be explained in the following. The substrate is made of 200- μm -thick high-resistivity Silicon layer (HR Si, with $\epsilon_r = 11.9$ and $\rho = 3000 \Omega \cdot \text{cm}$), on which a 300-nm-thick silicon dioxide SiO_2 thin film is thermally grown. On the front side of the substrate, a 500-nm gold monopole is printed, whereas on the back side a partial ground plane is deposited, so as to provide a balanced configuration for optimal antenna feeding without using any ad-hoc balun. The EM design of the single antenna is shown in Figure 3.7, with a schematic cross-section of the vertical layout in the inset. The main dimensions are listed in table Table 3.2.

Parameter	Value
R	0.979 mm
L_{feed}	2.024 mm
W_{feed}	0.158 mm
L_{gnd}	1.9 mm
L	5 mm
W	4 mm

TABLE 3.2: Design parameters of the circular patch array shown in Figure 3.7.

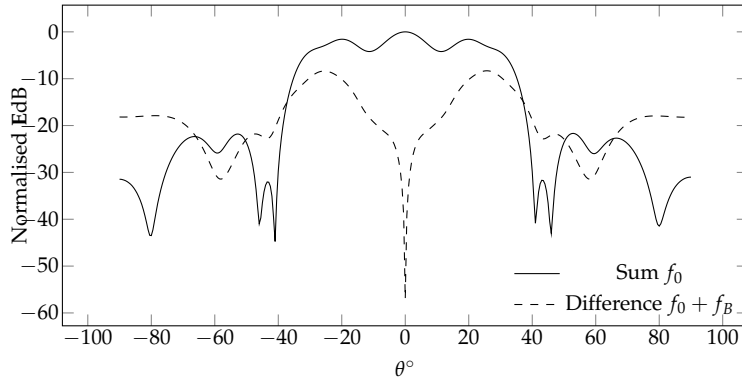
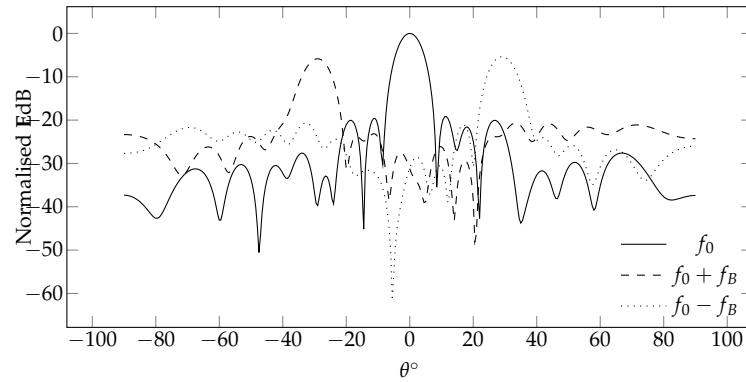
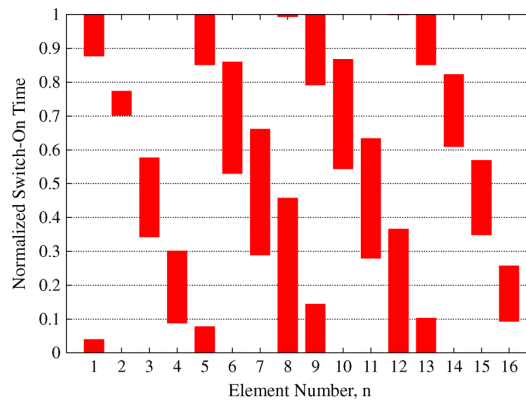


FIGURE 3.9: Radiation pattern of the excited array by excitation of the two central elements.

In Figure 3.8, the simulated antenna input impedance Z_{in} is provided: in this case, at 28 GHz $Z_{in} = 49.3 + j5.8\Omega$, which corresponds to a slight inductive reactance $L_{ind} \approx 33$ pH. This aspect could be beneficial for impedance matching to the integrated MIM diode, which is characterized by a capacitive impedance. As regards the radiating performance, the monopole clearly exhibits an omnidirectional radiation pattern with radiation efficiency of over 95% at 28 GHz. The whole array was simulated port-by-port in order to provide the full input impedance matrix and the normalized radiated far field necessary for the HB nonlinear simulation of the TMA. This way, all the EM coupling among array elements are taken into account rigorously.

(a) f -dependent radiation pattern

(b) Switch sequence

FIGURE 3.10: Radiation pattern of the proposed array by the excitation sequence shown in [116][©] [2011] IEEE.

Nonlinear/EM Co-Simulation Results

The exploitation of the nonlinear/EM co-simulation approach described in [110] is of strategic importance in order to fully account for the highly dynamic behaviour of both the switching circuit and the radiation mechanism. With respect to previous TMA designs in the microwave range [110], [112], this experiment turns out to be more delicate for the stronger EM couplings between the array elements and for the actual piloting of the MIM diodes.

The envisaged application refers to the smart WPT strategy described in [112]: in the first step, the sole inner couple of antennas is used to perform localization by taking advantage from the exploitation of the Sum and Difference radiation patterns, at the fundamental and the first sideband harmonic, respectively, according to the Radar Monopulse principle [117]; the second

step consists in precisely sending the power for the energization of the tags in correspondence of the sole directions where tags were previously detected.

In the simulation process a modulation frequency $f_B = 100$ kHz has been used, and 3 harmonics of the fundamental carrier f_0 are needed to take into account the MIM diode nonlinear behaviour.

By means of an antisymmetric biasing with on-period= 50% [112] of the two diodes of the two inner antennas (antennas no.8 and no.9 of the 16-element array) the radiation patterns shown in Figure 3.9 are obtained: it is worth noticing that these patterns are simultaneously produced by the TMA without any phase-shifter at the antenna ports, but simply providing an anti-phase time shift of the two switches control pulses. A neat negative peak is obtained, which is of primary importance in localization: in fact, the combination of the Sum and Difference patterns received from the tags produces an appropriate figure of merit exploited for this purpose, the Maximum Power Ratio ($\text{MPR} = \text{Sum}(\text{dB}) - \text{Difference}(\text{dB})$) [112].

For the second WPT phase, the whole 16-element TMA is deployed by considering an input power at each antenna port equal to -8 dB. The simulation of different power levels revealed some difficulties in terms of finding a solution for the co-simulation scenario for a larger range of transmitted power. Therefore, I restricted the work to the highest power level possible.

The adopted excitation sequence is taken from [116], and again exploits the sideband radiation phenomenon, achieving a simultaneous radiation in three different directions (i.e., -30° , 0° , 30°) for the first positive sideband, the fundamental, and the first negative sideband. The achieved performance (shown in Figure 3.10, together with the control sequences) is acceptable, but not as good as the ideal one expected from [116], where the time-dependent AF of isotropic radiators is considered, only. Here the strong EM couplings between the array elements, and most of all the non-ideal behavior of the MIM diodes are taken into account: this results in a lower amplitude of the

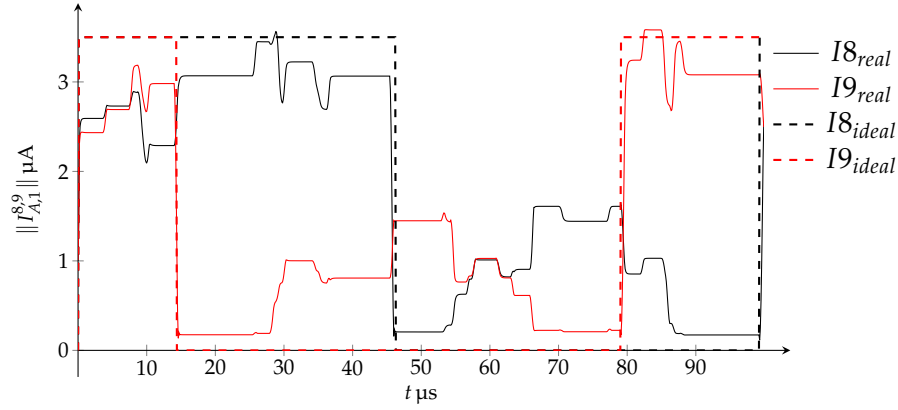


FIGURE 3.11: Current waveforms for ideal switches, and simulated nonlinear switches.

sideband lobes (more than 5 dB) and higher side-lobe levels of all the patterns.

The reason of the described behavior is easily inferred by the evaluation of the envelope waveforms (due to the switches modulation) at the fundamental harmonic of the currents feeding the antennas. Figure 3.11 reports, as an example, the waveforms of the current phasors of ports no.8 and no.9 (inner antennas of the array) with solid lines; the dashed lines correspond to the ideal behavior expected from the excitation pattern shown in Figure 3.10. From figure inspection it is clear that each switch behavior is highly influenced by the neighboring devices: unwanted rebounds of the diodes current significantly alter both the amplitude and the phase conditions imposed by the ideal optimization of [116]. This experiment stresses the importance of the adopted co-simulation strategy, already emphasized in [118]: the combination of this analysis approach with the design algorithm (as the one described in [116]) becomes of paramount importance if mm-wave architectures are envisaged.

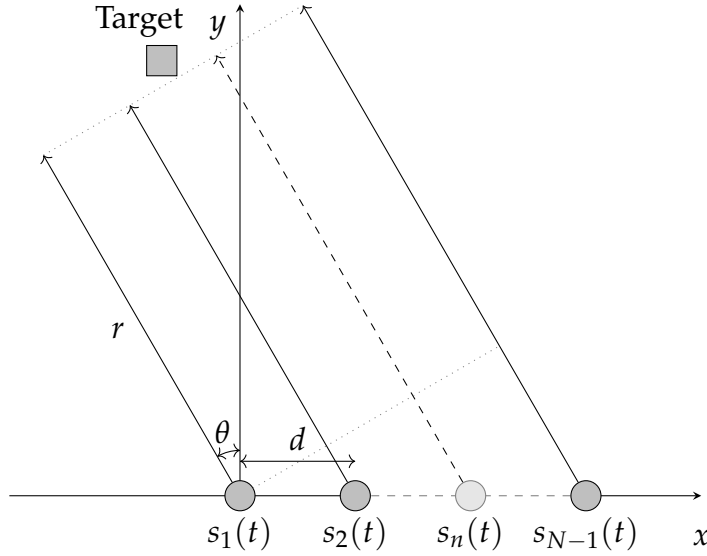


FIGURE 3.12: Schematic of a FDA antenna array system with respective elements, and variables.

3.4 Frequency-diverse Arrays

As denoted earlier in the introduction, the importance of FDA comes from the possibility to control the array radiation pattern such that it becomes distance-dependent. In the following I will demonstrate how this can be realised and will show the output of some simulations using the EM/nonlinear co-simulation technique explained in section 3.3.3. In the end, the possible realization techniques will be discussed.

3.4.1 Mathematical Concept

The FDA utilizes the simple antenna array structure just as frequently reported in the literature [115]. As shown in Figure 3.12, if maximum response (additive summation of all array signals) is desired at a distant target located at an azimuth angle θ , then a phase difference ψ as shown in (3.11) between the neighbouring elements will result in the desired steering.

$$\psi = \frac{2\pi f_0 d}{c_0} \sin(\theta) \quad (3.11)$$

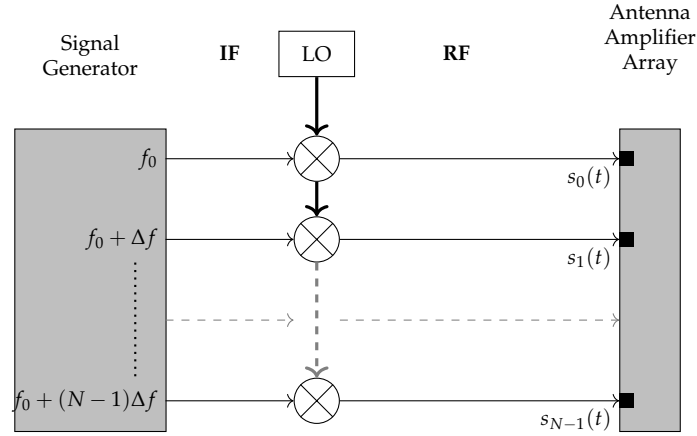


FIGURE 3.13: Suggested schematic for FDA system signal generation.

In the FDA system, however, a frequency difference between the excitation signals exists. And the resulting excitation signal is also frequency-dependent based on the element order n . Such signals might be obtained from the circuit shown in Figure 3.13. Under this assumption, a linear frequency *step* exists for the excitation signal as shown in (3.12).

$$s_n(t) = e^{j2\pi(f_0+n\Delta f)t-jn\psi} \quad (3.12)$$

In the suggested system, if the first array element is considered as the reference element, the phase difference between the n^{th} and the 1^{st} element may be given in (3.13) [119].

$$\Delta\Phi_{n-1} = \frac{2\pi(n-1)\Delta fr}{c_0} - \frac{2\pi(n-1)^2\Delta fd \sin(\theta)}{c_0} - \frac{2\pi(n-1)f_0 d \sin(\theta)}{c_0} \quad (3.13)$$

With respect to (3.11), Equation 3.13 shows in the first term dependence on the distance between the array and the target. The third term, however,

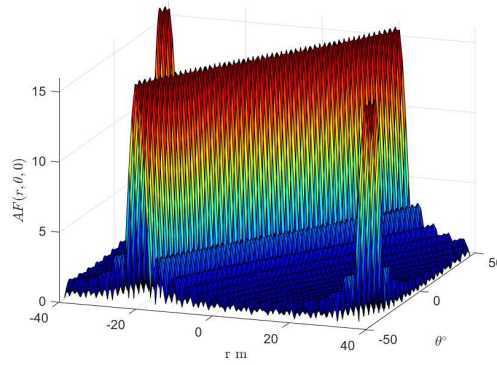


FIGURE 3.14: 3D plot of the FDA AF response as a function of azimuthal angle θ and distance r .

represents the steering angle of (3.11) at frequency $(n - 1)f_0$. As for the second term, Wang et al. [119] have found that it can be *empirically* approximated as shown in (3.14) as long as the condition in (3.15) is satisfied.

$$\frac{2\pi(n-1)^2\Delta fd \sin(\theta)}{c_0} \approx \frac{2\pi(n-1)\Delta fd \sin(\theta)}{c_0} \quad (3.14)$$

$$\frac{n^2\Delta f \sin(\theta)}{c_0} - \frac{n\Delta f \sin(\theta)}{c_0} \leq \frac{\pi}{4} \quad (3.15)$$

Furthermore, they argue that this approximation remains valid for FDA systems for arrays of many-hundred elements with frequency stepping reaching around 1 MHz. That is, the approximation remains valid for large FDA systems for many antenna types with regular bandwidth constraints. This approximation helps to reach a formula that describes the AF behaviour. Starting from (3.12) and replacing t with $(t - r_n/c)$ to account for phasor delay for the n_{th} element, the time-dependent AF may be reached (3.16) [119].

$$\begin{aligned} AF(r, \theta, t) &= \sum_{n=0}^{N-1} e^{j2\pi(f_0+n\Delta f)(t-r_n/c_0)-jn\psi} \\ &\approx e^{j\Phi_0} \frac{\sin \left[N\pi \left(\Delta ft - \frac{\Delta fr}{c_0} + \frac{f_0 d \sin(\theta)}{c_0} + \frac{\Delta fd \sin(\theta)}{c_0} \right) \right]}{\sin \left[\pi \left(\Delta ft - \frac{\Delta fr}{c_0} + \frac{f_0 d \sin(\theta)}{c_0} + \frac{\Delta fd \sin(\theta)}{c_0} \right) \right]} \end{aligned} \quad (3.16)$$

Where N is the number of array elements, f_0 is the reference carrier frequency used on the first element, Δf is the frequency spacing, r_n is the distance of the n_{th} element from the target, and ψ is the regular phase shift as identified in (3.11).

In fact, there is also a time dependency as shown in (3.16) that leads to a beam spanning all the (r, θ) combinations, for a time $1/(N\Delta f)$ and with period $1/(\Delta f)$ [119].

Assuming a transmitting system made of 16-element linear array, transmitting at $f_0 = 2.45$ GHz with $d = \lambda_0/2$ element spacing and $\Delta f = 5$ MHz the AF can be found from (3.16). In Figure 3.14 the 3D response is plotted with respect to r and θ . Instead of illuminating the entire space, the array shows a strong dependence on distance r giving maximum response $AF \approx N = 16$ at specific r values thanks to the excitation signal.

Therefore, *the FDA system in this example helps to minimize the illuminated space to very limited positions by using the frequency-dependent excitation signal.* This also means that large cut back on energy consumption would be expected as no illumination exists for unwanted positions if a rectenna is not present.

As shown from (3.16), the AF is also dependent on frequency spacing Δf which affects the curve slope as shown in Figure 3.15. Starting from a small frequency shift $\Delta f = 1$ MHz as shown in Figure 3.15a, the array shows a varying maximum location with respect to r , a very inclined maximum root locus is obtained for $\Delta f = 10$ MHz as in Figure 3.15c with many maxima within the scanned range. In a nutshell, this behaviour represents an evolution from the classical array situation with $\Delta f = 0$ that reveals a vertical maximum root locus as shown in [120] for all r values.

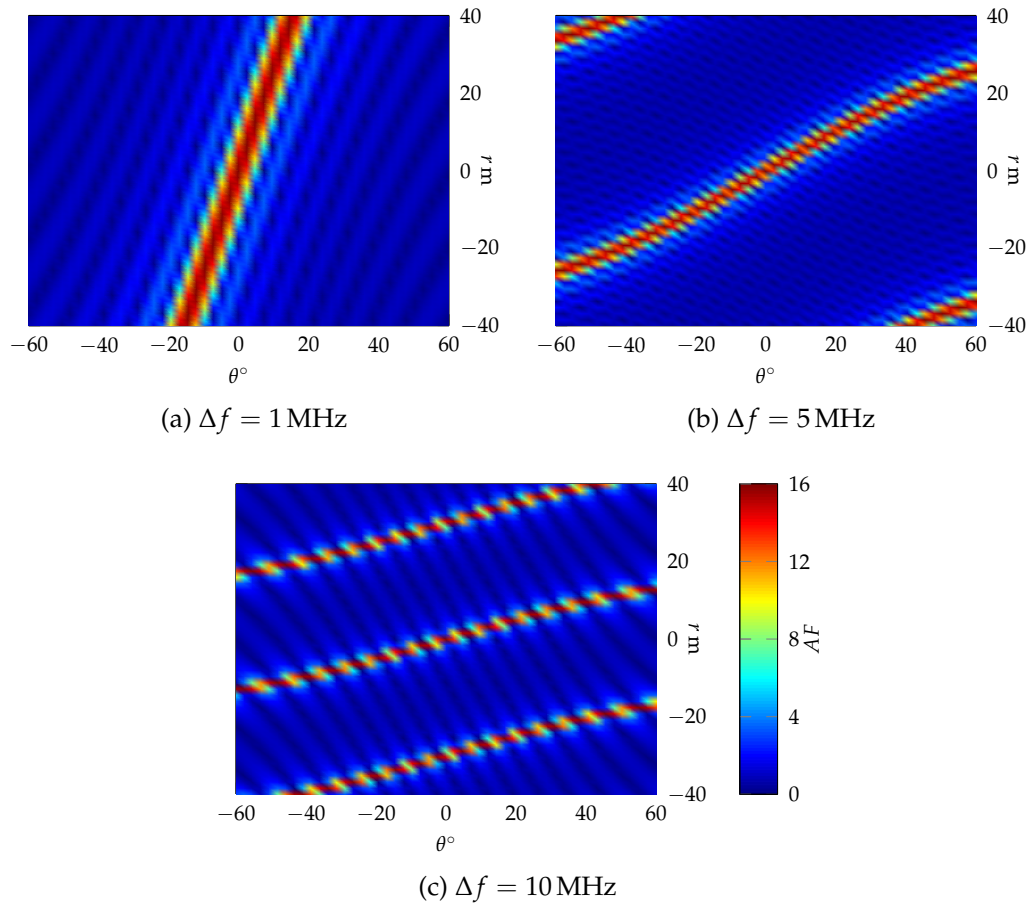


FIGURE 3.15: The FDA array factor for $\Delta f = 1$ MHz, 5 MHz and 10 MHz

Δf GHz	θ_{max}°		
	$r = 5$ m	$r = 10$ m	$r = 20$ m
5	9.8	19.2	42
10	19.35	41.85	-41.4

TABLE 3.3: Azimuth angles corresponding to maximum AF values for $\Delta f = 5$ MHz and 10 MHz.

3.4.2 Co-Simulation of FDA

Harmonics Generation

The simulation of FDA systems can result in a very demanding task, especially when a high number N of radiating elements is involved, as in the case of focusing power transfer. In fact, if each element feeding path manages its own frequency and has its own power amplifier, the correct manner for dealing with such a nonlinear radiating circuit is to resort to the co-simulation strategy presented in [110], where the full-wave frequency description of the linear array/feeding network is passed to the HB-based tool able to accurately manage the description of the nonlinearities in the time domain: the resulting nonlinear regime is then responsible for far-field radiation. In the FDA case, the problem arises from the N independent tones (with spacing Δf) needed in the analysis: if N is greater than 4, available commercial tools are not able to manage all the intermodulation products falling at frequencies:

$$F_m = m_0 f_0 + m_1 (f_0 + \Delta f) + \cdots + m_N (f_0 + N \Delta f) \quad (3.17)$$

if a proper maximum intermodulation order $M = |m_0| + |m_1| + \cdots + |m_N| : M \geq 3$ is considered.

A valid alternative to this approach is to assume that Δf is the Least Common Multiple (LCM) (since it represents the smallest frequency shift in this regime). In this case, the generic m_{th} harmonic of the spectrum is simply given by $f_m = m \Delta f : (m = 0, 1, 2, n_H)$, and the N exciting signals can be simply retrieved utilizing the formula:

$$m_k = \frac{f_0 + k \Delta f}{\Delta f} \quad (3.18)$$

$$k = 0, 2, \dots, N - 1$$

Excitation f	Excited element		
	GHz	$s_1(t)$	$s_N(t)$
f_0		$A_\theta^1(\omega_0), A_\phi^1(\omega_0)$	$A_\theta^N(\omega_0), A_\phi^N(\omega_0)$
f_1		$A_\theta^1(\omega_0 + \Delta\omega), A_\phi^1(\omega_0 + \Delta\omega)$	$A_\theta^N(\omega_0 + \Delta\omega), A_\phi^N(\omega_0 + \Delta\omega)$
\vdots		\vdots	\vdots
f_{N-1}		$A_\theta^1(\omega_0 + (N-1)\Delta\omega), A_\phi^1(\omega_0 + (N-1)\Delta\omega)$	$A_\theta^N(\omega_0 + (N-1)\Delta\omega), A_\phi^N(\omega_0 + (N-1)\Delta\omega)$

TABLE 3.4: Contents of the radiation pattern database generated for each $f_n = f_0 + (n-1)\Delta f$ and for each array element.

Far Field Database Organization

In this way, the mono-dimensional FFT and IFFT can be adopted to switch from the time to the frequency domain, and vice versa with a huge saving of processing time and memory; hence the FDA complex regime can be easily managed by a common pc. Being a radiating nonlinear circuit, the final output of the FDA analysis is the far-field radiated in a given direction at given distance. Because of the linearity of the antenna system, the far-field synthesised by the circuit nonlinear regime assumes an expression for the E field as shown in (3.4).

Instead of assuming a constant frequency response of the linear antenna systems, the [41] has been developed to account for reading the array radiation pattern database for each element excitation at a the corresponding excitation frequency as shown in Table 3.4. In fact, this involves a *nested* far field radiation pattern import where each each loop needs to read data N times². This export is better done in an automated way as there are N^2 files to export. So a VBA code has been written to automate the task on CST Microwave Studio[®] of which the nested exportation part is shown in Appendix A.

Simulation Procedure

In order to analyze how the system behaves in a more realistic scenario, a 16-element array as the one shown in Figure 3.16 is modelled on CST Microwave

²We have N elements and N frequencies.

Studio[®] together with single Field Effect Transistor (FET) amplifiers using the following steps:

- suitable choice of the array elements to guarantee an acceptable variation of S parameters values within the total frequency shift (i.e. $f_0 + (M - 1)\Delta f$).
- full wave simulation of the array is done; As each element will transmit a signal slightly shifted with respect to the original as shown in (3.12), each element in the array is excited accordingly and the array radiation pattern and S parameters are obtained.
- data export is done scanning all the frequency values for all the excited elements and frequencies using the database demonstrated in Table 3.4.
- Data is used into the HB nonlinear simulator [41] to reach a solution assuming a generic FET amplifier circuit at the input of each array element.

As an example of application, we consider the planar linear array of Figure 3.16, consisting of $N = 16$ monopoles realized on a Taconic RF60A substrate ($\epsilon_r = 6.15$, $\tan \delta = 0.0028$, $h_{thick} = 0.635$ mm) aligned along the x -axis, with inter-element spacing $d = \lambda/2$ at the resonance frequency of 2.45 GHz.

A single-FET amplifier with 15 dB gain is placed at each antenna port, and 16 ideal sinusoidal generators are placed in correspondence of the 16 circuit input ports to generate the frequency-diverse coherent signals, according to (3.18). We selected $f_0 = 2.45$ GHz as the *centre* frequency of the 8th monopole. Therefore, two scenarios have been co-simulated using the frequency spacing in (3.18), to observe where the maximum θ values occur with respect to the ideal model results shown in Table 3.3:

- Scenario. 1 for which $\Delta f = 5$ MHz and $f_0 = 2.415$ GHz.
- Scenario. 2 for which $\Delta f = 10$ MHz and $f_0 = 2.38$ GHz.

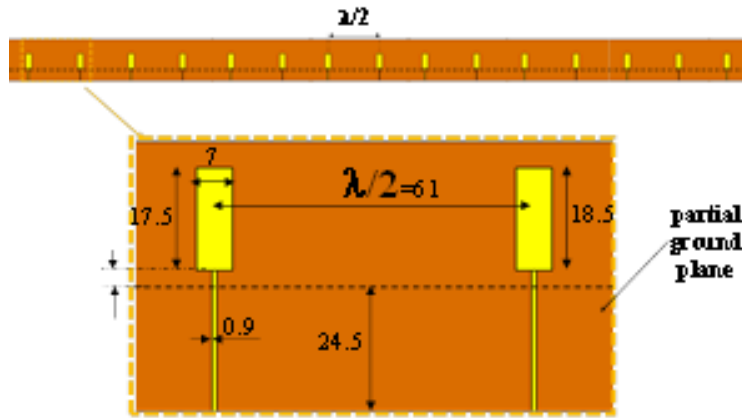


FIGURE 3.16: Geometric structure of the FDA array element spacing and a snapshot of the entire array[120]© [2019] IEEE.

3.4.3 Results

As a first trial, the RF sources have an available power of -10dBm each, thus not forcing the amplifiers into saturation: hence we focus our attention on the linear radiating phenomenon, only. In order to make all the elements operating in a sufficient wide identical frequency bandwidth a slight retuning of the external monopoles length (for $n = 1$ and 16) has been done. Hence, the corresponding nonlinear array results in a non-standard one that can be rigorously analysed by a combined full-wave/nonlinear approach [110], only.

The nonlinear FDA system is analysed under the scenarios mentioned as opposed to the theoretical case where ideal isotropic radiators are assumed without either electromagnetic couplings or dynamic effects. The HB analyses of the FDA architecture, includes the electromagnetic description of the array of Figure 3.16, and is carried out with a total number of spectral lines $n_H = 2000$. This corresponds to a total frequency band of 10 GHz and 20 GHz for scenarios 1 and 2, respectively. The $N = 16$ exciting tones are thus identified through (3.18) and correspond to the spectral lines from 483 to 498 in the first scenario, and to the spectral lines from 238 to 253 in the second scenario.

The simulations are performed for both scenarios and the E field amplitude is normalized with respect to the highest achieved amplitude (Boresight

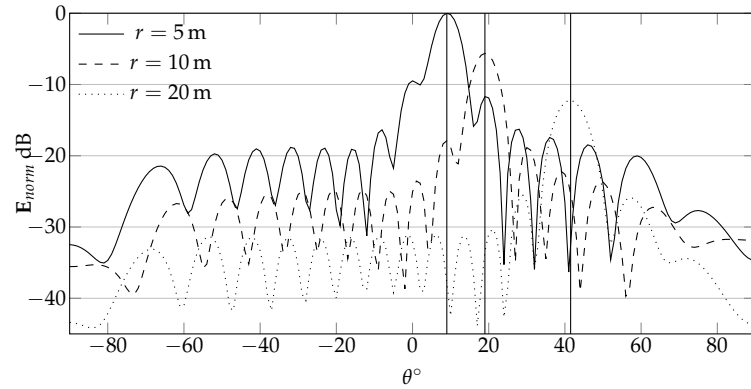


FIGURE 3.17: Simulation results for $\Delta f = 5$ MHz, and $P_{av} = 10$ dBm.

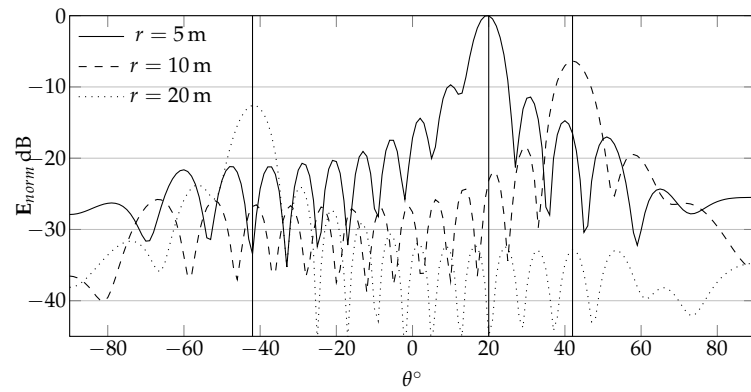


FIGURE 3.18: Simulation results for $\Delta f = 10$ MHz, and $P_{av} = 15$ dBm

radiation at the closest distance $r = 5$ m). Results are shown in Figure 3.17, Figure 3.18, and Figure 3.19.

Figure 3.17 shows the corresponding normalized radiation patterns in the azimuth xz plane using -10 dBm Tx power. The simulated patterns show a behavior quite close to the ideal one: the three maxima for the r values 5, 10, and 20 m occur at 9° , 19° , and 41° , respectively, for $\Delta f = 5$ MHz as in Scenario. 1. The situation is quite similar for Scenario. 2.

Table 3.5 shows comparison between θ values corresponding to maximum array factor for the modelled distances and those obtained from the theoretical model and shown in Table 3.3. The comparison is done in terms of absolute difference $\Delta\theta = \theta_{max,AF}^{sim} - \theta_{max,AF}^{mod}$ and relative difference $\epsilon_\theta = \Delta\theta / \theta_{max,AF}^{mod}$ as shown in Table 3.5.

Scenario	r	$\theta_{max,AF}^{sim}$	$\Delta\theta$	ϵ_θ
1	5 m	9°	-0.8°	-8.16%
	10 m	19°	-0.2°	-1.04%
	20 m	41°	-1°	-2.38%
2	5 m	20°	0.65°	3.36%
	10 m	42°	0.15°	0.36%
	20 m	-42°	-0.6°	1.45%

TABLE 3.5: Comparison between co-simulation, and modelling values of the azimuth angles θ corresponding to maximum AF .

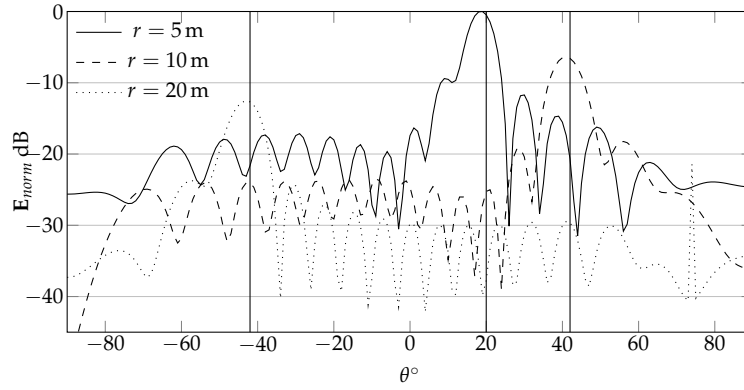


FIGURE 3.19: Simulation results for $\Delta f = 10$ MHz, and $P_{av} = 10$ dBm

The results reflect the correctness of the FDA concept in terms of focusing the power at specific distances. Furthermore, analysing the relative received field intensity $\|\mathbf{E}\|$ dB at different distances $r = 5, 10, 20$ m reveals an inverse relationship to the square of distances. This was revealed after normalizing the output radiation patterns at different distances where the boresight of each distance has a maximum depending on the focusing distance r . In fact, checking the maximum boresight level shows a behaviour inversely proportional to the square of the distance from the array as depicted in (3.19) in such that the following relation is satisfied for all the co-simulated scenarios demonstrated in Figure 3.17, Figure 3.19, and Figure 3.18.

$$\frac{\|\mathbf{E}_{r1}\|}{\|\mathbf{E}_{r2}\|} = \left(\frac{r2}{r1}\right)^2 \quad (3.19)$$

3.5 Conclusion

In this chapter the time-modulated array and the frequency-diverse array concepts have been demonstrated. Both techniques can potentially contribute to a next generation of wireless power transmitters such that the transmitter circuit in addition to the transmitted signal efficiency are the main focus of both approaches, respectively.

Based on the results obtained from the time-modulated array simulation, using MIM diodes seems to offer a good substitution to Schottky diodes paving the way for higher frequencies to be used in wireless power transfer applications. The results obtained here encourage the search for different and more realistic diode models. In particular, the MIIM tunnelling diodes due to the increased current levels compared to their single layer counterparts.

Having said that, the complex behaviour of nonlinear devices can significantly affect the performance of the whole system and thus the switching currents should be optimised to reduce the off-state leakage current. Equally importantly, the antenna array elements should have as minimum mutual coupling as possible to prevent feed back able to alter desired diodes dynamic. A unique Computer-aided Design (CAD) platform, combining the presented rigorous simulation approach with available optimization strategies, seems to be mandatory at mm-wave frequencies.

Furthermore, the first attempt to the accurate analysis of FDA arrays has been demonstrated, representing a potential candidate for wireless power focusing applications. Even in their simplest architecture, these nonlinear arrays represent a demanding simulation task, that cannot be faced with traditional numerical methods, because of the complex multi-tone regime to be

managed. The exploitation of a periodic regime within an HB-based framework, with the small frequency shift among the array elements as fundamental tone, allows a computationally light and, at the same time, accurate analysis.

The initial co-simulation analysis is quite encouraging to investigate the performance of this system more. However, the simulation has been done using ideal generators. For future versions of this system, it would be necessary to introduce some imperfections to make the system even more realistic. In real-world amplifiers, things like phase noise, thermal and other sources of noise are quite common. Furthermore, investigating a realistic source with some phase difference, and frequency deviations from the wanted values is important to analyse the impact of these factors on the FDA system performance.

This method has demonstrated its effectiveness in standard FDA analyses, and will be deployed in the future for advanced FDA-based architectures rigorous co-design. Having said that, the realization of a coherent generator that can guarantee, at the same time, accurate frequency and phase spacing among generated signals $s_n(t)$ will be a challenging task.

A possible solution might be to use a hybrid RF/computer-driven signal source to achieve high level of coherence. In light of this idea, the conceptual design given in Figure 3.13 might be a good starting point. In this design, a processor-generated output in the Intermediate Frequency (IF) range might be used to drive the input of a low noise and highly linear Local Oscillator (LO) array that is responsible to step up the frequency to the desired RF range. The RF output is, then, fed into an array of amplifiers that drive the FDA antenna array as shown in Figure 3.13.

Chapter 4

Low Frequency Energy Harvester Design

4.1 Introduction

For future sensor networks, IoT, and other wireless networking technology it is important to supply energy for many devices wirelessly to minimise dependence on batteries. In this case, sensors might be planted anywhere, work completely independently without batteries, and be responsible to read data like physical parameters to transmit the readings wirelessly to another device. A possible scenario for such near-future case might be to power up wireless sensors in harsh industrial environments using commercial substrates and elements within the unlicensed Industrial, Scientific, and Medical (ISM) transmission bands. At the University of Bologna, we have envisaged a WPT system that caters for these demands and complies with the mainstream regulations regardless of the region in which it will be used. For such system, the following design objectives have been put forward:

- The $f = 2.4$ GHz band has been chosen.
- In practice, the rectifier will be part of a rectenna device as shown in Figure 4.1. Therefore, the designed rectifier model will be optimized for operation with a real world antenna using its S Parameters.

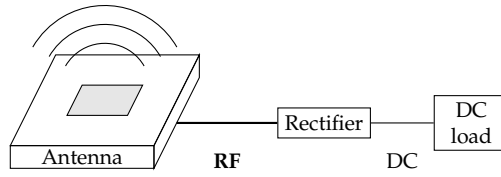


FIGURE 4.1: Conceptual design of the energy harvesting wireless solution.

- For mass production, it is much more preferred to avoid the costly low $\tan(\delta)$ substrates. And so, the rectifier should be designed on a commercial FR4 substrate. For the rest of this chapter the following parameters are assumed when modelling transmission lines on FR4: Thickness $H = 1$ mm, dielectric constant $\epsilon_r = 4.3$, losses $\tan(\delta) = 0.025$, and copper thickness $T = 17 \mu\text{m}$.
- The choice of FR4 substrate gives higher priority to use lumped elements than microstrip lines as the latter will have large dimensions and higher losses on FR4.
- The wireless link power budget evaluation -as will be explained later subsection 4.7.1- reveals a -10 dBm expected input power for the rectifier input. Therefore, the optimized rectifier should achieve $\eta_{-10 \text{ dBm}} \geq 40\%$ as a *minimum requirement*. This necessitates to use an efficient diode as demonstrated in section 4.2. As for the rectifier topology, the use of a single stage voltage doubler features more flexible design for the matching circuit, such that no DC shorting to ground is required.

Based on these objectives, the design process starts from the theoretical model of a double-diode rectifier to evaluate the rectifier input resistance for $P_{in} = -10$ dBm. Based on this value, a suitable matching circuit that meets the objectives and achieves matching with the antenna is used. Afterwards, an optimization process is carried out to increase the efficiency using real world components represented by their corresponding models. The final circuit layout is, then, produced and a physical prototype is fabricated. In the

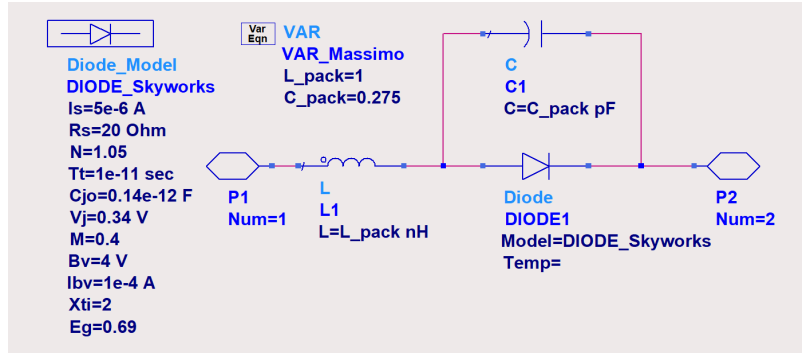


FIGURE 4.2: The adopted Schottky diode model with the parasitic components.

end, measurements are taken in a real world free space propagation scenario to compare the results to the theoretical evaluations.

4.2 Nonlinear Device Choice

Out of the many diode types available in the market, Schottky diodes feature low opening voltage and fast switching time as mentioned in subsection 2.2.1 in addition to a well-established fabrication process. In fact, there are many commercial models used in the literature such as the HSMS-2855 [48], HSMS-2850 [28], and HSMS-7630 [121].

Thanks to the HSMS-7630 diode high responsivity and low dynamic resistance values, it offers close-to-ideal efficiency figures that makes it preferable for low-power harvesting applications [122]. In fact, using the Keysight Technologies ADS[®] Schottky diode model shown in Figure 4.2, and scanning a small voltage range from -50 mV to 50 mV gives the $I(V)$ curve shown in Figure 4.3.

The responsivity $f_{RES}(V)$, and the dynamic resistance $R_D(V)$ are found from a polynomial curve-fitting process on the $I(V)$ curve and gives the curves shown in Figure 4.4a and Figure 4.4b, respectively.

The importance of the responsivity FOM as a measurable quantity, comes from its direct impact on the diode efficiency yield η_D . The latter quantity

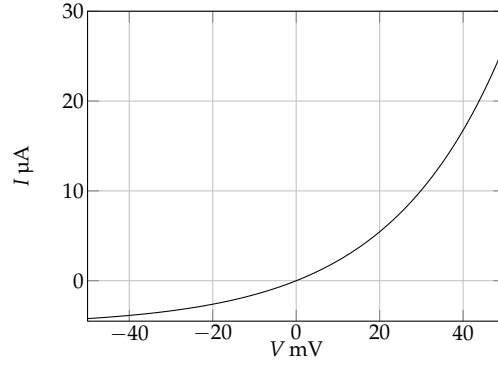


FIGURE 4.3: The responsivity f_{RES} , and dynamic resistance R_D FOM curves for the HSMS-7630 diode.

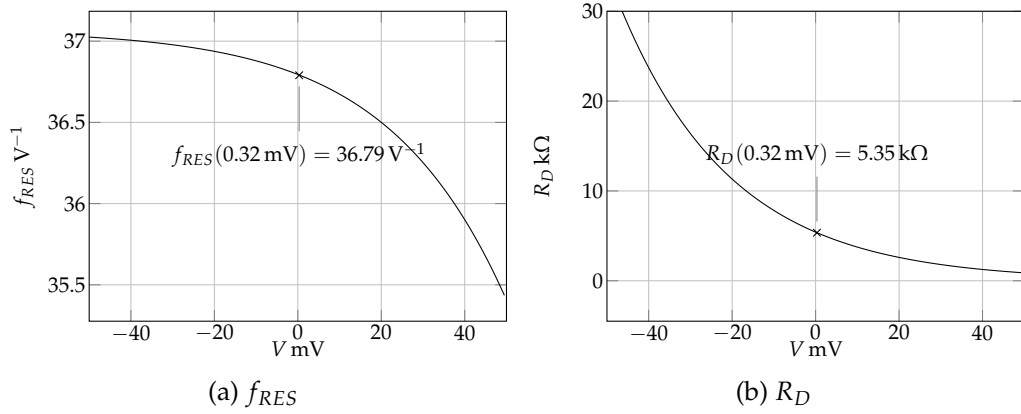


FIGURE 4.4: The responsivity f_{RES} , and dynamic resistance R_D FOM curves for the HSMS-7630 diode.

may be found from the responsivity f_{RES} as explained in [122] for a small RF signal variation and shown in (4.1).

$$\eta_D = f_{RES}^2 P_{in} \eta_{RF} \frac{R_D}{(2 + 2(\omega C_j)^2 R_D R_L)^2} \quad (4.1)$$

This equation is found assuming a structure similar to the one shown in Figure 4.5. In (4.1) f_{RES} is the diode responsivity, P_{in} is the input power of the rectifier circuit, η_{RF} is the RF matching efficiency between the RF generator and the rectifier circuit. This model takes into account the current that passes in the linear part of the parasitic components -mainly the junction capacitor C_j -, in addition to the optimum DC ohmic load R_L . The model assumes that $R_L = R_D$ to achieve the optimum efficiency.

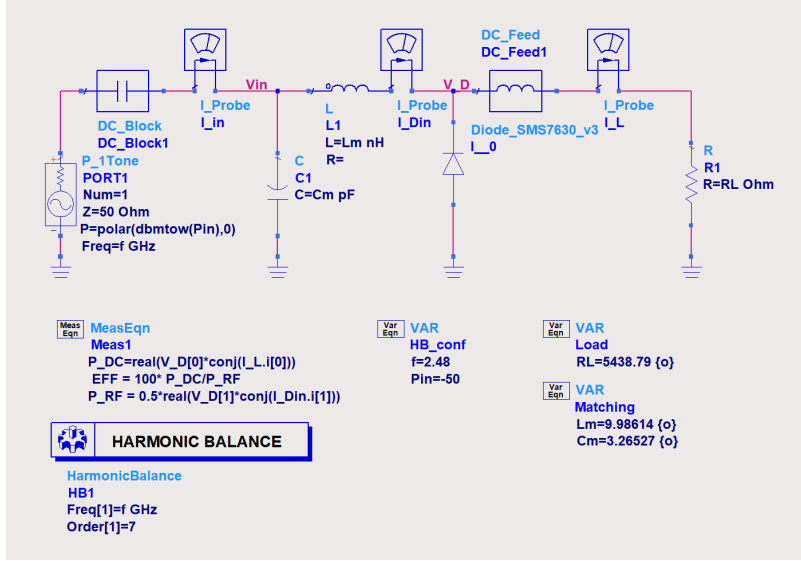


FIGURE 4.5: A single diode rectifier model to measure its performance.

Using $f = 2.48$ GHz, $P_{in} = -50$ dBm, and running an optimization of the RF matching circuit and the load R_L in the circuit shown in Figure 4.5 we get the optimum efficiency $\eta_{sim} = 0.196\%$ for a DC biasing voltage on the diode $V_D = 0.325$ mV, and $R_L = 5.4$ k Ω .

Of course, the diode is required to give much higher yield than 0.2%. However, the efficiency test model is valid for small signal variation around zero bias. Attempting higher biasing voltages and higher RF inputs results into more complicated equation than (4.1) and renders the validation process more complex.

From Figure 4.4, the corresponding responsivity and dynamic resistance values for a DC bias $V_D = 0.325$ mV are $f_{RES} = 36.79$ V $^{-1}$, and $R_D \approx 5350$ k Ω , respectively. Indeed, using these values, the values of R_L and V_D found from the optimization, C_J , R_S values taken from the Schottky model in Figure 4.2, and assuming $\eta_{RF} = 1$ gives $\eta_D = 0.206\% \approx \eta_{sim}$.

Parameter	Value	Description
C_{r1}	10 pF	Rectifier capacitor
C_{r2}	10 pF	Rectifier capacitor
D_1, D_2	SMS-7630*	Schottky diode model
R_L	$5 \times 10^3 \Omega$	Rectifier load resistor
f_0	2.48 GHz	Fundamental frequency
N_H	8	Number of simulated harmonics
R_0	50 Ω	Characteristic, generator and reference impedance
P_{in}	-10 dBm	Available input power

* Using the model from [124], with modified parasitic values based on previous experiments at the University of Bologna.

TABLE 4.1: Chosen simulation configuration, component values, and device models for the initial circuit model.

4.3 Initial Prototype Model

The proposed prototype is assumed to harvest energy and work interoperatively with an IoT application. Furthermore, for a harsh and short-range communication industrial environment the ISM communication band 2.4 GHz is considered to deploy the Long Range Wireless (LoRa) WAN protocol [123].

Although higher losses are expected for this high frequency as shown from the link budget calculations, the short-range losses for a one-meter link are acceptable and offers wider acceptance of this ISM frequency at the international scale [125].

The advantage of using LoRa protocol for this short-range scenario is the robust coding scheme that can survive most of the hostilities of an industrial environment. In order to ensure efficient interoperation with the proposed LoRa communication system, the operation frequency of the harvesting system has been chosen to be $f_0 = 2.48$ GHz.

The prototype shown in Figure 2.5 represents the starting point of the actual design with a suitable choice of the supporting elements and the load resistor as shown in Table 4.1.

The prototype of the circuit is developed on Keysight Technologies ADS[®]

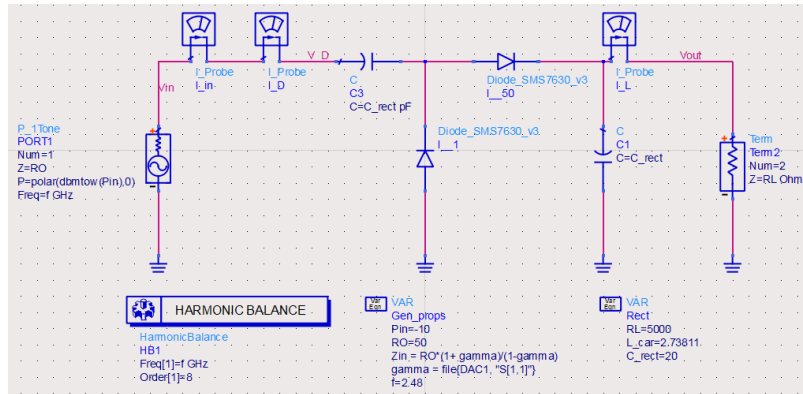


FIGURE 4.6: Schematic model of the simulated rectifier circuit using ADS.

simulation program, as shown in Figure 4.6, and is simulated using HB with the configurations shown in Table 4.1 to obtain the current i_1 and voltage v_1 values at the rectifier input¹. These values help out to evaluate the rectifier input impedance Z_{in} at the corresponding power level by simply using the following relation on the complex current and voltage values:

$$Z_{in} = \frac{v_1}{i_1} \quad (4.2)$$

Running this simulation with HB, the spectrum for 8 harmonics is obtained in terms of magnitudes and phases as shown in Figure 4.7. Using (4.2) the rectifier input impedance $Z_{in} = (5.83 - 79.79i) \Omega$ at $P_{in} = -10$ dBm. This value is used to evaluate the initial values of the subsequent matching circuit.

4.4 Matching Circuit Design

Theoretically, finding the optimum matching solution requires to solve a circuit that contains linear components such as the microstrip and other lumped

¹The subscript refers to the k^{th} harmonic resulting from HB simulation. In this case, we just consider the fundamental.

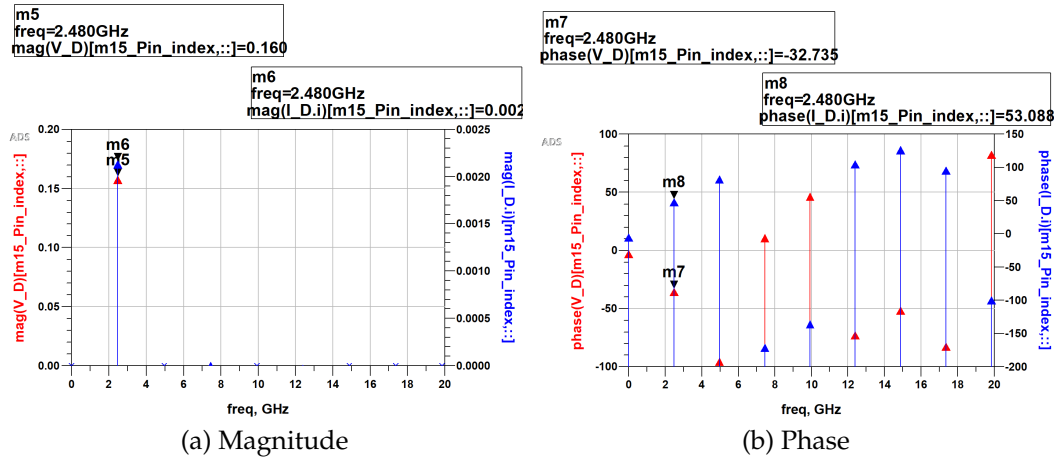


FIGURE 4.7: Spectral analysis of the input voltage v_{in} and current i_{in} signals of the initial rectifier design.

elements, in addition to the nonlinear Schottky diodes. Attempting this mathematical model will yield complicated self-consistent formulas of the form:

$$f_{nl}(x) - x = 0 \quad (4.3)$$

where $f_{nl}(x)$ is a nonlinear function. Instead, I have assumed a simplified linear diode model at $P_{in} = -10$ dBm to identify the linear matching circuit which will be considered the starting point of a subsequent optimization procedure.

In light of the requirements demonstrated earlier, a loaded L matching circuit is used such that the vertical branch is realized using a shorted microstrip on FR4 substrate instead of a lumped inductor. This approach features a more *continuous* solution space for the stub dimensions instead of the limited and discrete induction values available from commercial vendors. Using the classical Loaded-Q design methods [126], and using the Z_{in} value found earlier, the matching circuit solution is demonstrated in Figure 4.8 next to the corresponding S parameters response.

Figure 4.8b shows the S Parameters simulation from 0 GHz to 20 GHz.

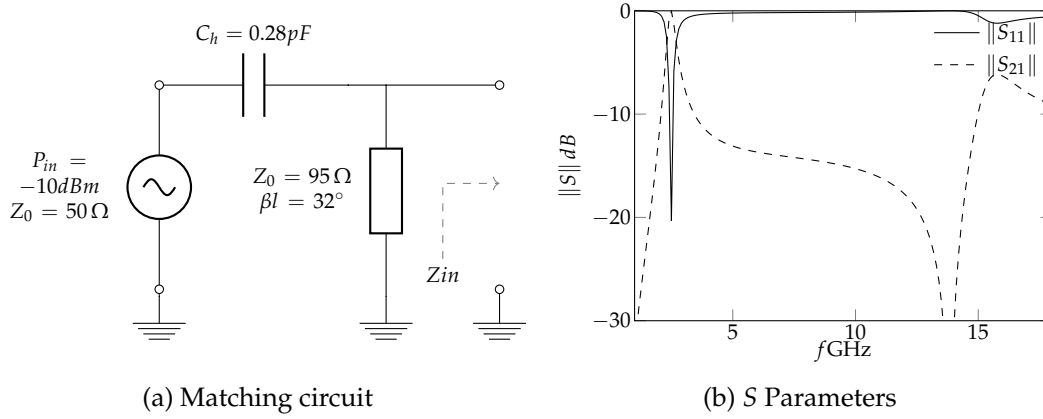


FIGURE 4.8: Rectifier matching circuit schematic and the corresponding S Parameters response.

Based on the S Parameters values, the matching circuit has a relatively narrow notch at the design frequency f_0 where the fundamental harmonic is passed and other harmonics are blocked. This design shows another resonating impact at $f = 13.8$ GHz where the circuit experiences high rejection. This behaviour helps to block the harmonics inside the rectifier circuit, thus helping to stimulate the nonlinearity inside the rectifier. This solution is the initial state to be optimized in a subsequent step.

It should be noted that the losses from this approach are acceptable as the stub is relatively short and so the solution smoothness outweighs the losses caused by the lossy material. To further minimise the losses, a thinner stub with higher characteristic impedance $Z_0 = 95 \Omega$ is assumed to realise the matching.

4.5 Efficiency Equation And Calculation

The efficiency yield of this rectifier system may be found based on Equation 2.12 given that the power source has a single frequency f_0 , so (2.12) becomes:

$$\eta = \frac{V_L^2}{0.5R_L \cdot v_{1,in} \cdot i_{1,in}^*} \quad (4.4)$$

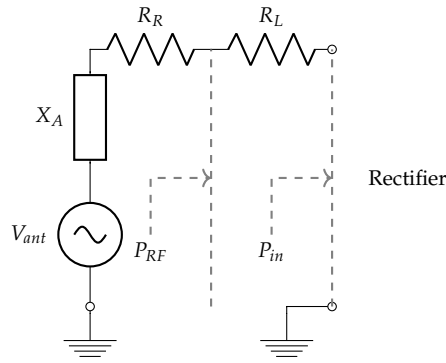


FIGURE 4.9: Real antenna equivalent circuit where the available power, together with the antenna internal impedance forms a whole block as shown in the dashed grey square.

the values of $v_{1,in}$ and $i_{1,in}^*$ are read from the simulation in addition to R_L , and V_L to calculate the efficiency.

For a real-world solution, the typical generator is replaced by a practical antenna which, in fact, has two impacts:

- the internal impedance has non standard values which can be calculated from S Parameters using the relation:

$$Z_A = R_A + jX_A = Z_0 \frac{1 + S}{1 - S} \quad (4.5)$$

- the real component of this impedance has also two parts: $R_A = R_R + R_L$

For the latter impact, a small modification is needed on the efficiency equation. Figure 4.9 shows the generic antenna equivalent circuit where the real component has two parts, the *useful* part R_R which represents the radiation impedance and is responsible for the transmission/reception of the EM signal, and the losses part R_L which has a zero value only in ideal antennas and represents the losses inside the antenna material. On the other hand, the reactive part X_A in this representation accounts for both the EM and the antenna material reactive contributions.

From an optimisation point of view, the imaginary part X_A is compensated for by the suitable choice of the subsequent reactive components. On



FIGURE 4.10: Photo of the utilized antenna for the harvester.

the other hand, the optimisation solution does not account for losses in the R_L and considers the whole R_A in the optimisation process. This would result in a best possible case that maximizes the efficiency output.

As for ideal antennas $R_L = 0 \Omega$ and the whole $R_A = R_R$ contributes to the radiation/reception process. Consequently, there are no losses in the antenna equivalent resistance. However, the power P_{RF} that is received by the antenna from the EM radiation experiences some loss due to the R_L contribution and becomes P_{in} at the rectifier input as shown in Figure 4.9. As the losses are purely ohmic and all other antenna material contribution is merely reactive, a simple correction factor $\alpha = P_{in}/P_{RF}$ may be suggested such that a coefficient (equal to the antenna radiation efficiency resulting from full wave EM simulations) is multiplied by the available EM power at the input P_{RF} and the efficiency (4.4) equation becomes:

$$\eta_{real} = \frac{P_{out}}{P_{RF}} = \alpha \frac{P_{out}}{P_{in}} = \alpha \frac{V_L^2}{0.5R_L \cdot v_{1,in} \cdot i_{1,in}^*} \quad (4.6)$$

Therefore, the efficiency calculation equation in the simulation program is simply multiplied by α to account for the antenna losses [127].

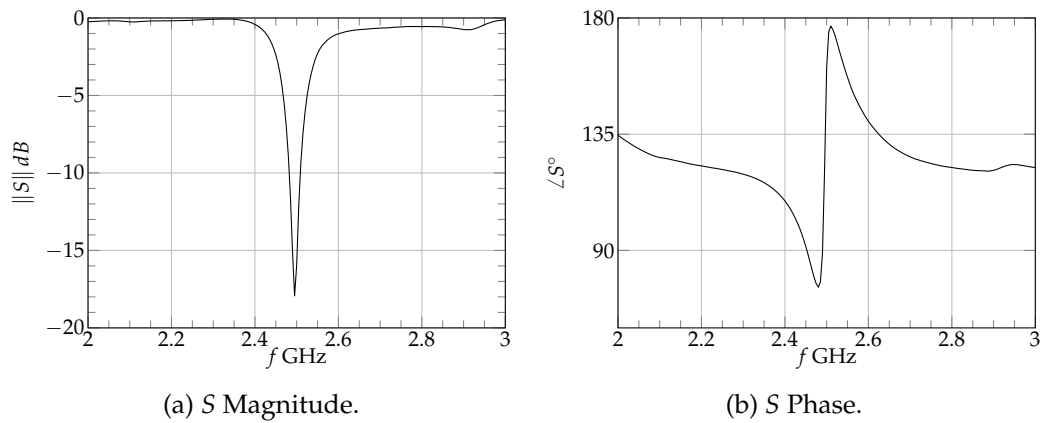


FIGURE 4.11: Magnitude and phase of the measured S Parameters.

4.6 Circuit Optimisation And Realisation

Using the component values shown in Table 4.1 and Figure 4.8a, the suitable components for the design have been searched in the market. The corresponding component models are placed into the circuit model and simulated to compare the efficiency values with the initial scenario using ideal components. The component selection process was carried out in a try-and-error approach to reach best possible efficiency given the following conditions:

- The realised circuit should be frequency-selective to ensure that the harmonics are well trapped within the rectifier section. That is, harmonics leaking to the generator or the load are negligible.
- The real components must be as lossless as possible to minimise overhead losses.
- The reactive components must preserve the same reactive behaviour for the entire frequency range. In other words, a capacitor should stay a capacitor for a large bandwidth before a self resonance frequency occurs and changes its reactance sign.

The ideal components have been replaced by practical ones as shown in Table 4.2. Also, the generator has been replaced by a shorted patch antenna

Component	Value	Real Component
$C_{r1} =$	20 pF	GJM1555C1H200GB01
$C_{r2} =$	2×10 pF	$2 \times$ GRM1885C1H100JA01
$C_h =$	0.3 pF	GRM1555C1HR30WA01

TABLE 4.2: Real components that replace the ideal ones to be included in the optimisation process.

[128], identified by its S Parameters response shown in Figure 4.11 and specifically designed for this application as shown in Figure 4.10. The antenna is represented in the simulation such that the voltage source stands for the received wireless radiation, and the antenna S Parameters shown in Figure 4.11 can be used to calculate this voltage source internal impedance $-Z_A$ as seen from the rectifier- at the corresponding frequency.

Empirically, it has been found that the most sensitive component in the rectifier is the matching circuit capacitor that needs to keep its capacitive behaviour up to $5f_0$ before the first self resonance frequency². Otherwise, the efficiency suffers large decrease if this capacitor has sub optimum performance. The second sensitive component is the rectifier first capacitor C_{r1} which also needs to feature good frequency characteristics to ensure good operation.

After placing these components in addition to the short circuit stub in the schematic shown in Figure 4.12, an optimisation process has taken place to optimise the dimensions of the stub in addition to the load resistor. The optimisation goal is to increase the efficiency using Equation 4.4 so that a minimum of 40% is achievable *using real components* assuming available power $P_{in} = -10$ dBm at the rectifier input (exiting the antenna in Figure 4.1 towards the rectifier). Table 4.3 shows the initial and final optimisation values for the corresponding components.

Due to the optimisation process, the dimensions of the matching stub

²The model of the matching circuit input capacitor GRM1555C1HR30WA01 offers very good frequency characteristics with respect to many other tried models even within the same model family [129].

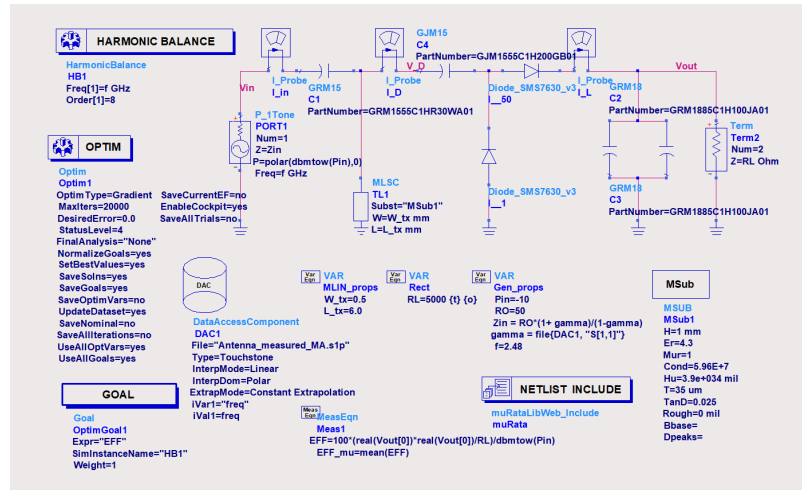


FIGURE 4.12: Schematic of the optimized circuit using the real components as modelled on ADS[®].

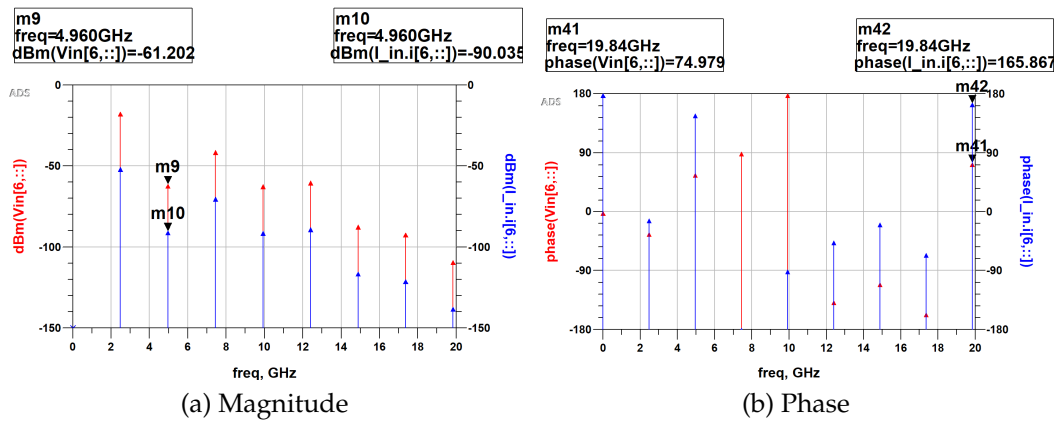


FIGURE 4.13: Spectral analysis of the v_{in} , and i_{in} signal to the optimised rectifier.

have been changed. The optimisation process has changed the role of the matching stub towards minimising the exchanged power at harmonics with $n \geq 2$. This has been revealed by investigating the input signal spectrum of the "matching" circuit v_{in} and i_{in} .

Figure 4.13 shows the magnitude and phase spectral analysis of the harmonics at the input of the capacitor GRM155C1HR30WA01. Except the fundamental frequency, all the higher harmonics have phase difference $\approx \pm 90^\circ$ although their magnitudes are relatively high with respect to the fundamental. This means that the dissipated or gained power from the generator at frequencies other than f_0 is almost zero as the exchanged power is mainly

Component	Initial	Final
L_{tx}	5.9 mm	5.7 mm
W_{tx}	0.52 mm	0.49 mm
R_L	5 k Ω	6.44 k Ω

TABLE 4.3: Initial and final values for the optimised components.

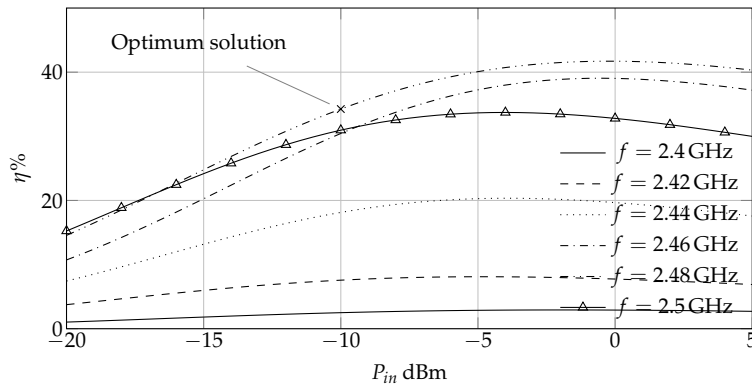


FIGURE 4.14: Analysis of the rectifier efficiency across $P_{in} = -20$ dBm to 0 dBm for a range of frequencies from $f = 2.4$ GHz to 2.5 GHz.

reactive.

As a result of the optimisation process, an efficiency increase is obtained at $P_{in} = -10$ dBm with respect to 3.75% if no matching circuit is used. Detailed curves are drawn together with measurements' results in Figure 4.19.

To, further, ensure that the optimizer has reached the optimum solution for f_0 , an efficiency analysis for a range of frequencies from 2.4 GHz to 2.5 GHz has been performed. Figure 4.14 shows evidently that the $f = 2.48$ GHz curve has superior performance over all other curves at $P_{in} = -10$ dBm.

The layout of the circuit is realised using the Keysight Technologies ADS[®] Layout Editor, and the layout has been exported to Gerber[®] files. Figure 4.15a shows an image of the ADS[®] Layout editor with the corresponding dimensions, and Figure 4.15b shows the realised circuit on a FR4 board.

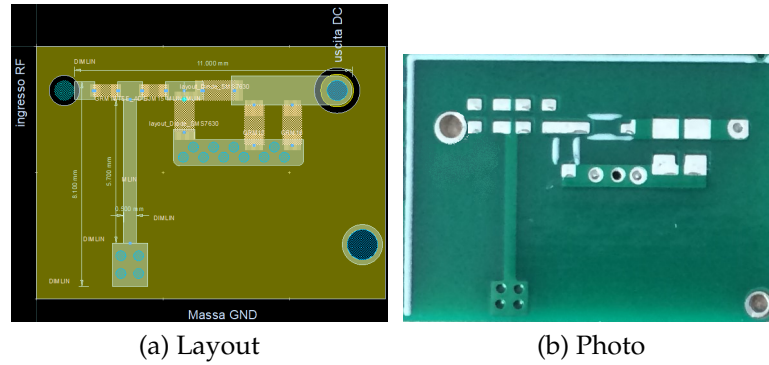


FIGURE 4.15: Image of the circuit layout and the realised circuit on FR4 board.

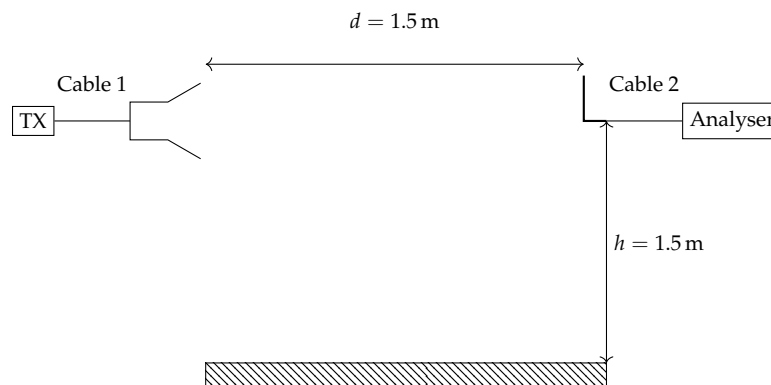


FIGURE 4.16: Sketch of the calibration and measurement scenario.

4.7 Measurements and Results

To measure the response of the rectenna in a real world environment, a calibration process was done to estimate the FSL losses so that a fairly accurate guess of the received power by the rectifier is possible. In this process a simple scenario that consists of a horn antenna transmitter and a short dipole receiver is assumed with the spacing shown in Figure 4.16. The estimated losses from this process will help to evaluate the available EM power when the dipole is replaced by the receiving antenna of Figure 4.10 when the bore-sights of the horn and the receiving energy harvesting antennas are aligned.

Parameter	Value	Description
$f_0 =$	2.48 GHz	Operation frequency
$G_H =$	10 dBi	Horn gain
$\eta_{H,rad} =$	-0.706 dB	Horn radiation efficiency
$G_D =$	2 dBi	Dipole gain
$\eta_{D,rad} =$	-0.706 dB	Dipole radiation efficiency
$L_{C1} =$	-2.25 dB	Cable 1 losses
$L_{C2} =$	-4.45 dB	Cable 2 losses
$d =$	1.5 m	Distance between Tx and Rx
$h =$	1.5 m	Height of both antennas from ground

TABLE 4.4: Parameters used to calculate the FSL of the measurement scenario

4.7.1 FSL Calculation And Link Budget

In the calibration process, the parameters shown in Table 4.4 are used to estimate the received power at the dipole.

The FSL in this scenario can be simply calculated using (3.1) so that $L_{FSL} = -31.85$ dB. This number, together with the values available from Table 4.4 will help to evaluate the received power at the dipole using the following power budget equation:

$$P_R = P_T + L_{FSL} + L_{C1} + L_{C2} + \eta_{H,rad} + \eta_{D,rad} = P_T - 39.96 \text{ dB} \quad (4.7)$$

Therefore, if the horn antenna transmits a single tone at f_0 with $P_T = 0$ dBm, the received power by the antenna is simply -39.96 dBm. This number is, in fact, not distant from the mean measured value where the received power is about $\langle R, meas \rangle = -39.5$ dB. Figure 4.17 shows the power received by the dipole at an instance of time for 0 dBm transmitted power.

To have -10 dBm EM power at the antenna side, (4.7) can be used to account for the patch antenna shown in Figure 4.10 whose gain is $G_{patch} = 2.0$ dBi without placing the radiation efficiency reduction factor as this will

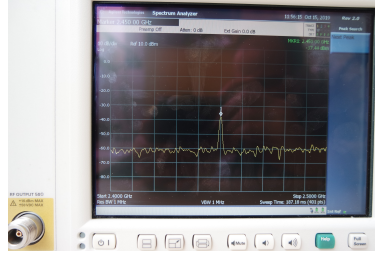


FIGURE 4.17: Spectrum analyzer reading of the received signal by the dipole antenna.



(a)



(b)

FIGURE 4.18: Rectenna measurement setting.

be included in the rectifier efficiency calculation. Therefore (4.7) becomes:

$$P_T = P_{RF} - L_{FSL} - L_{C1} - \eta_{H,rad} = -10 + 31.85 + 2.25 + 0.706 = 24.8 \text{ dBm} \quad (4.8)$$

4.7.2 Rectifier Measurement Settings And Results

The short dipole antenna shown in Figure 4.16 was replaced by the shorted patch antenna together with the rectifying circuit where both are placed on a card board and hooked on a short wooden mast as shown in Figure 4.18a, two thin wires exit from the rectifier towards a potentiometer calibrated to $R_L = 6.44 \text{ k}\Omega$ which represents the rectifier load. The resulting voltage on the potentiometer is measured by a multi meter as shown in Figure 4.18b.

The response of the rectifier in terms of efficiency and voltage output has been measured for a range of transmitted power from the maximum

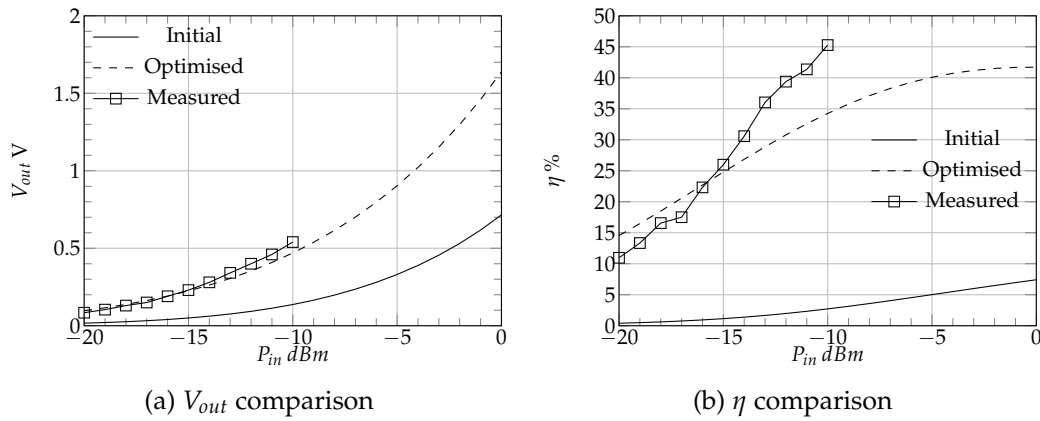


FIGURE 4.19: Efficiency and voltage output comparison as a function of input power between initial, optimised, and measured circuit.

achievable level $P_T = 24.8$ dBm (equivalent to $P_{RF} = -10$ dBm) down to $P_T = 14.8$ dBm. Trying higher power levels is not guaranteed to give accurate results because this would require to bring the shorted patch antenna closer to the horn outside the far field region and/or increasing the transmitted power level which already has maximum factory limits for the generator transmitted power.

In Figure 4.19a the voltage output as a function of the input power P_{in} for an optimally-loaded rectifier³ is shown for the initial circuit of Figure 4.6, the optimised solution shown in Figure 4.12, and the measurement of the realised circuit. Figure 4.19b, similarly, shows the efficiency comparison for the aforementioned circuits.

The results shown in Figure 4.19 show that a considerable increase has been achieved thanks to the matching circuit whose design has been altered by the optimisation process to maximise the efficiency of the rectifier. The voltage output is, generally speaking, in good accordance with the simulated value although the efficiency shows higher swinging behaviour of measurements with respect to simulations due to the squared proportionality to the voltage output as demonstrated in (4.4). Up to about -15 dBm the measured

³Using the value $R_L = 6.44$ k Ω

efficiency is slightly lower than the simulated response. After this point, behaviour is changed and the simulated becomes lower than the measured and the difference is about 10% in the worst difference case.

4.8 Conclusion

In this chapter, a rectifier design has been introduced. Instead of using purely lumped elements or purely distributed (microstrip) elements, a *hybrid* circuit design has been used, particularly, for the matching circuit. This hybrid style brings forward three benefits:

- Liberates the design from the restrictions of the available components values in the market and allows higher degrees of freedom for the optimisation process.
- Reduces the circuit size with respect to purely distributed solutions. At such frequency with a low-density board material such that of FR4, stub lengths used for matching would become a serious issue if integration with miniaturized circuits is to be considered.
- Losses in this case are acceptable and are potentially lower than the completely distributed solution case. In particular, if realised on a lossy substrate such as FR4 which has $\tan(\delta) = 0.025$. To the best of the writer knowledge, this is the first time a good efficiency figure reaching 45% at $P_{RF} = -10$ dBm is reached on a FR4 board using lumped components in the 2.4 GHz band.

As mentioned earlier, there is a slight discrepancy between the expected efficiency behaviour from simulations and the actual measured values. As a rule of thumb, this happens when a slight detuning of the elements exists. In this situation, there are some flaws which require further future investigation such as the close proximity of the short stub to the ground part right of the

stub as shown in Figure 4.18a. The fringing effect of the stub line has not been considered as only a simple transmission line model is used in ADS[®] instead of a full wave simulation. Another possible future work area may be to investigate the impact of the component footprints because they form a wave transition when the signal enters or exits the component. For all these issues, a co-simulation and optimisation approach is advised. Today, some commercial software are capable of doing such task so that the nonlinear part is simulated, and the linear part is optimized (e.g. by changing dimensions) using a planar form of full wave simulator -frequently called Two And A Half D (2.5D)-. This approach can quickly and efficiently give more accurate results for many planar structures.

Chapter 5

Efficient WPT Simulation

5.1 Preface

It has been mentioned in chapter 1 that the suitable choice of the modelling approach in the propagation medium is important to shorten simulation times and have a more accurate estimation of the received power by the harvesting antenna. In this part, I will introduce to a recent work that has been accepted for publishing [106], and shows a promising method developed on purpose for the accurate estimation of the available power used for the harvester design as the one introduced in chapter 4 to simulate propagation scenarios typically found in harsh industrial environments for potential future IoT applications.

5.2 Introduction

The importance of battery-less network sensors, and the future application of IoT has been highlighted in chapter 1. Therefore, Personal Area Network (PAN), and Body Area Network (BAN) network terminals, in addition to industrial network terminals utilising protocols such as LoRa and span a few centimetres should be easily powered up without battery. Therefore, for these terminals it is important to accurately estimate the available wireless power when they are placed in a real world scenario in operation.

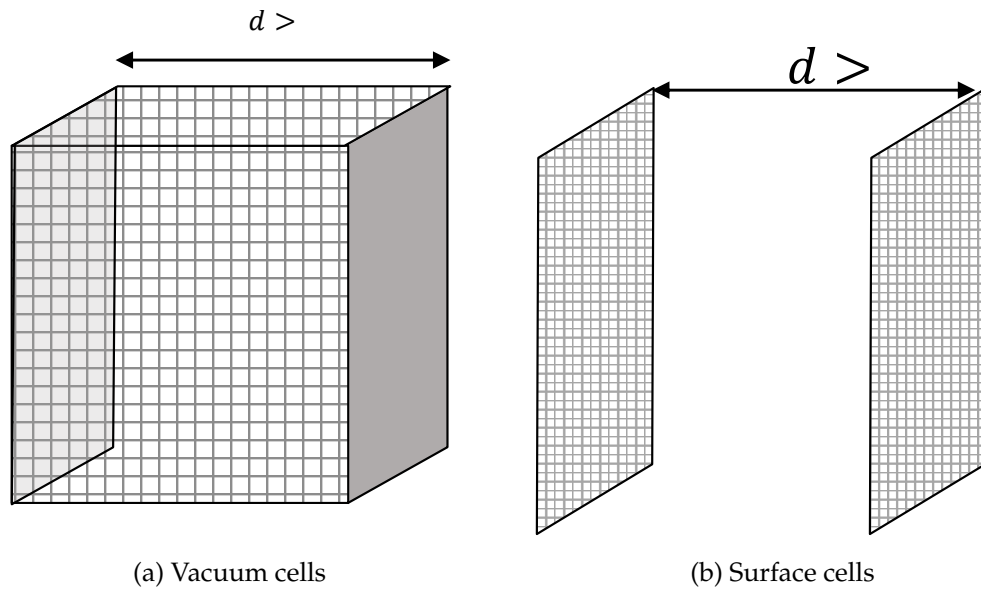


FIGURE 5.1: Conceptual comparison between the FD and IE meshing techniques.

In light of the previous scenario, we should be able to accurately estimate the available EM power to networks sensors (measuring a few cm^2) and placed in vicinity to the power transmitter (within a distance around, say, $5\lambda_0$). In practice, such scenario is very difficult to get solved accurately because:

- It may not always be a near field scenario and so applying the typical FD analysis (in particular when there are many metallic reflections) when the propagation dimensions exceed $5\lambda_0$. In which case, the solution mesh to such large problem would not always be time efficient or even accurately solved.
- It may not always be a far field scenario to switch to an efficient ray tracing approach.

Alternatively, we propose a method based on the reciprocity theorem concept and the IE technique [130] to propose a fast calculation approach to obtain more accurate simulation results. The strength of this approach comes from the fact that the solution mesh dimensions grow less quickly than the

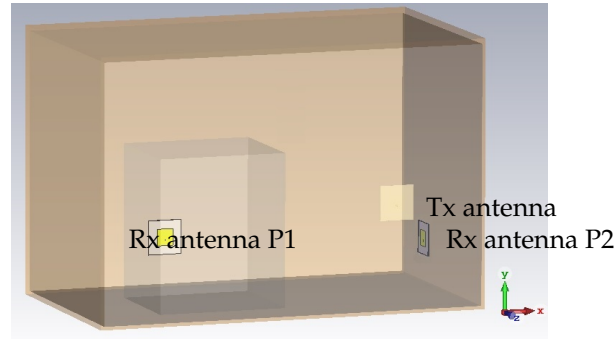


FIGURE 5.2: Snapshot of the simulated scenario. The Tx antenna is shown ahead of the propagation medium. There are two positions for the the receiving antenna points (P1) and (P2). Detailed spacing is shown in Table 5.1

typical vacuum 3D mesh when the dimensions are increased. To simplify the concept, a simple parallel plates scenario as shown in Figure 5.1. If the distance between them is increased, the typical FD techniques will suffer from a linear increase of the mesh cells, while the number of the surface cells as shown in Figure 5.1b will remain constant regardless of the distance.

The result is a much faster simulation time to obtain the superficial electric fields and deploy them in an equation found from the reciprocity theorem to find the transmitted power between Tx and Rx.

The rigorous approach proposed in [131] will be briefly revisited for the sake of clarity, and its adjustment to a real world propagation scenario will be discussed. The scenario consists of an illuminating Tx antenna which transmits the energy at a single frequency towards a semi closed metallic box as shown in Figure 5.2 that simplifies generic harsh electromagnetic environments such as a production line in an industrial ambience.

To model the impact of harsh industrial environment a metallic cuboid was placed in the box in addition to some sensors Rx antennas that are installed as shown in Figure 5.2. Using the IE solver of CST[®] Microwave studio [132], we will evaluate the electromagnetic fields on a virtual surface Σ as described later, use the obtained values in the proposed equation to obtain the value of the received power, and compare the results with those of the CST[®]

[132] time domain solver and practical measurements of a realized model.

5.3 Theoretical Background

Based on the reciprocity theorem concept, if a source is placed at port A to supply a linear electric circuit, and a meter is placed at port B to get readings, then one will obtain the same readings if the devices are swapped between points A and B. The same concept is generalised for EM propagation based on Maxwell's equations. This theorem, has many useful implications which can be used to facilitate real world problems. Based on [131], and [133], the generated current in a Rx antenna is given by (5.1).

$$J_{eq} = \frac{1 + Z_R Y(\omega)}{U} \cdot \hat{\mathbf{n}} \int_{\Sigma} [\mathbf{E}_S(P_{\Sigma}) \times \mathbf{H}_H(P_{\Sigma}) - \mathbf{E}_H(P_{\Sigma}) \times \mathbf{H}_S(P_{\Sigma})] d\Sigma \quad (5.1)$$

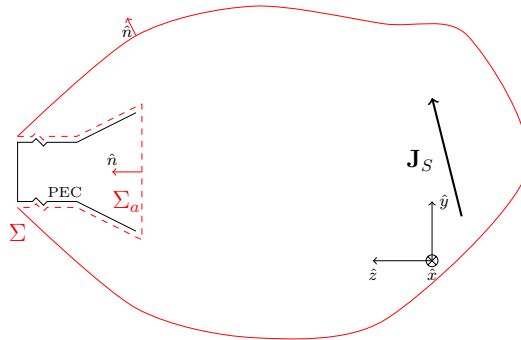


FIGURE 5.3: Conceptual representation of the chosen surface Σ , and the theoretical model used.

The equation shown in (5.1) has been found starting from the reciprocity theorem based on the choice of the closed surface Σ as shown in Figure 5.3. This surface includes a transmitter antenna represented by a current density vector \mathbf{J}_S located at a specific point in a space identified by the Cartesian unit

vectors $(\hat{x}, \hat{y}, \hat{z})$. The surface has been chosen such that it includes the Tx antenna and extends to $\|\mathbf{r}\| = +\infty$. However the receiver antenna, represented by a horn in Figure 5.3, is placed at a definite \mathbf{r} such that it is formulated as the dashed line shows.

Based on the reciprocity theory, the integral part in (5.1) approaches zero for $\|\mathbf{r}\| = +\infty$ because there will be no exchanged electromagnetic power between Rx and Tx antennas at distant points. The same applies for the integral over the perfect Perfect Electric Conductor (PEC) surface of the Rx antenna as they perfectly reflect the electric fields. The only remaining exception will be the Rx antenna aperture surface Σ_a as shown in the figure.

Hence, the integral problem is reduced to a finite space Σ_a to solve (5.1) by knowing the integral part over Σ_a . It is worthwhile noting that *no* far field approximation is involved in this treatment and this simple approach will also work for near field problems if the Tx antenna can be approximated by a point current density source \mathbf{J}_S as shown in Figure 5.3. The calculation of (5.1) is done on two steps as imposed by the reciprocity theorem:

- A suitable surface was chosen to read the \mathbf{E} and \mathbf{H} values from and deploy them in (5.1). In the studied case this suitable surface may be planar box aperture. In the CST[®] model, this has been set by assuming a thin cuboid of vacuum located at the box aperture and collect the values from the large outer surface.
- The Rx antenna works in reception mode and the electric and magnetic fields impressed on surface Σ_a by the transmitter \mathbf{J}_S are \mathbf{E}_S and \mathbf{H}_S , respectively. These fields cause the Rx antenna to work as a current source with value J_{eq} whose internal admittance is given by $Y(\omega)$. When the load of the antenna in this mode is completely matched, the

output power maybe obtained from (5.2).

$$P_{out} = \frac{\|J_{eq}\|^2}{8\text{Re}(Y(\omega))} \quad (5.2)$$

- The role of the Rx antenna is flipped and works as a transmitter. In order to maximize its transmitted power it should be matched at the transmission frequency to the generator whose internal resistance is R_g and its voltage source is U . In this case this antenna will generate the impressed electric and magnetic fields $\mathbf{E}_H, \mathbf{H}_H$ on the surface Σ_a , respectively. Similar to the case above, complete matching guarantees maximum power transfer which happens when $Z_R = R_g = 50\Omega$ in the present case.

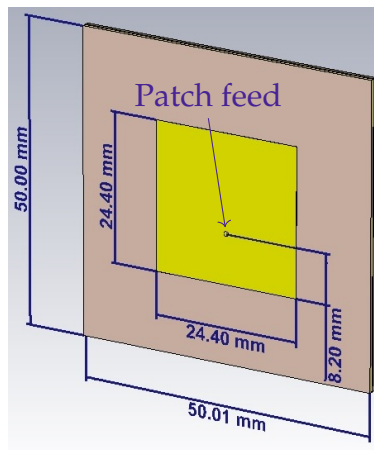
In (5.1) J_{eq} is the equivalent current source of the Rx antenna in reception mode. J_{eq} generates a current response inside the antenna load.

5.4 Simulated Prototype

5.4.1 Model Description

Figure 5.2 shows the simulated scenario. It is made of a carton box where inner side is illuminated by a transmitting antenna Tx located at a distance 36 cm from the box aperture. Inside it there is a smaller metallic cuboid which blocks the line of sight between Tx and Rx (P1). All of the surfaces inside the box, except for the antennas, are metallized with aluminium foil.

The Rx antenna at P1 has been tried with co and cross polar position where it has been rotated 90° around its axis. Another location P2 as defined in Table 5.1 has also been tried in the simulation. The inner dimensions of the carton box are $57.5\text{ cm} \times 37.5\text{ cm} \times 33.5\text{ cm}$ assuming that $\epsilon_r = 1.77$ and $\tan\delta = 0.023$ as measured in [134], for the electromagnetic wave solver.



(a) Patch

Parameter	Value
f	2.4 GHz
Gain	2.05 dB
HPBW ^a	97.7°
SLL ^b	-9.8 dB
$Y(\omega)$	(0.025 + 0.0011i) S
P_{rad}	0.207 W
η	41.5%

^a HPBW: halfpower beamwidth.

^b SLL: side lobe level.

(b) Characteristics

FIGURE 5.4: Snapshot of the patch antenna used for the Tx and Rx antennas, and the corresponding parameters.

It is also assumed that the lining aluminium thickness is 100 μm with the default electric properties in CST[®] used in the simulation. The smaller box inside measures 19 cm \times 22.5 cm \times 16.3 cm and is completely covered with foil.

The Tx antenna has been set such that it is axially aligned with the box at distance 36 cm from the box aperture. The Rx antenna in the first case is put at height 6.9 cm from the box bottom behind the obstruction and was tried with two orientations. The third case was tried with the same Rx antenna at a different location (P2) inside the box as shown in Figure 5.2.

Both the Tx and Rx antennas have been realized using patch antenna structure shown in Figure 5.4 with ROGERS4360 substrate with $\epsilon_r = 6.15$ and $\tan\delta = 0.0038$. They have been designed to radiate at $f = 2.4\text{ GHz}$, and they measure 2.5 cm \times 2.5 cm each. Table 5.1 lists the exact locations for all the objects in the simulated scenario, while in Figure 5.4b the simulation output of the electric parameters of the utilized patch antenna are listed.

The TD solver runs as usual, whereas the following steps have been done to obtain the results using the IE solver approach :

- Discrete simulation for both the Tx and Rx antennas is made to identify

Object	Location	
Tx	Distance 36 cm from box aperture	axis aligned with box's axis
Rx(P1)	Height 6.9 cm from bottom	Displacement 20.7 cm from inner left
Rx(P2)	Height 6.9 cm from bottom	Displacement 9.5 cm from box inner face
Obstruction	Depth 15.5 cm towards inside from box aperture	Displacement 20.5 cm from inner left

TABLE 5.1: location of objects and antennas in the simulated scenario, and patch antenna characteristics

their internal impedance Z_R and admittance $Y(\omega)$. Using the \mathbf{E} and \mathbf{H} fields values exported from CST[®], we can directly use the Tx antenna radiation pattern into the IE solver and so we can flexibly locate and direct the Tx antenna.

- For a propagation scenario, we identify a surface Σ between the Tx and Rx antennas. In theory, this surface contains the Tx antenna and extends in the manner explained in Section 5.3. In practice, the IE solver gives results just for the defined surfaces. Therefore, we define a suitably-enclosed air surface that extends over the aperture and utilize the results of just one surface (i.e. the tangential surface to the box aperture and we consider this surface as Σ_a).
- The Tx antenna, is located in the desired location and directed as required, the simulation is run and both the electric \mathbf{E}_S and magnetic \mathbf{H}_S fields values for each point of the surface points P_Σ are evaluated.
- The same is repeated for the Rx antenna and the \mathbf{E}_H and \mathbf{H}_H values over Σ_a are saved.
- A post-processing script is used to read the results from the exported \mathbf{E} and \mathbf{H} fields, and apply the equation in (5.1) to obtain the value of J_{eq} .

- The current value obtained is used to calculate the received power assuming a matched load to find the ratio P_{out}/P_{rad} between received and radiated power, and compare this value against S_{21} obtained from TD solver.

The excitation signal of the Tx antenna is assumed to be equal to 0.5 W such that for efficiency $\eta = 41.5\%$ the radiated power $P_{rad} = 0.207$ W as shown in Figure 5.4b This yields a voltage source value $U = 9.052$ V, to generate the corresponding radiated power.

5.4.2 Simulation Results

The described scenario has been prototyped on CST[®] and simulated using the TD solver, and the IE solver to benchmark the accuracy and performance results. The scenario comprises three cases:

- Co-polar orientation at P1.
- Cross-polar orientation at P1.
- Co-polar orientation at P2.

Table 5.2 shows the results of the IE and TD simulation comparing their results. The time taken to perform each type of simulation is mentioned in Table 5.3 on an 2 GHz-intel[®]Xeon[®] processor on a machine with 32GB of RAM.

Case	IE		TD	
	$\ J_{eq}\ $ mA	P_{out} μ W	$\frac{P_{out}}{P_{rad}}$ dB	$\ S_{21}\ ^2$ dB
a)	1.65	41.93	-35.33	-39.18
b)	0.402	2.48	-47.60	-46.43
c)	0.874	11.73	-40.86	-48.32

TABLE 5.2: Comparison between calculated values by IE and TD methods.

Case	Suggested method		
	Patch Simulation	IE	TD
a)		29 min	17 h, 28 min
b)	20 min	26 min	17 h 46 min
c)		28 min	16 h 34 min

TABLE 5.3: Comparison between simulation time taken by IE and TD methods.

From Table 5.3 it is evident that while the IE solver takes much shorter time than the TD solver, there is no significant change in the amount of received power calculated by IE as demonstrated in Table 5.2. The difference between these results may be attributed to the mathematical difference between the two approaches where the solving domain is much larger in the case of TD solver compared to the case of IE.

With reference to Figure 5.1 as a vacuum-based problem the modelled scenario requires more than 18 million cells for the TD simulation, while just less than 29500 triangular cells are required for the surface-based IE solver. This huge difference between the two approaches positively impacts on both the required solution time and accuracy.

5.5 Measurements

Using a Hittite[®] HMC-T210 the Tx antenna has been fed to generate the transmission signal to illuminate the box shown in Figure 5.5. Inside this box, the Rx antenna has been placed in the positions shown in Table 5.1 and connected to Agilent Technologies[®] N1996A spectrum analyzer to measure the received power for the aforementioned cases.

A scan from $-10dBm$ to $20dBm$ range for the transmitted power has been performed for each of the three cases and the corresponding received power has been registered for a 30-sample-sliding-window average-based marker

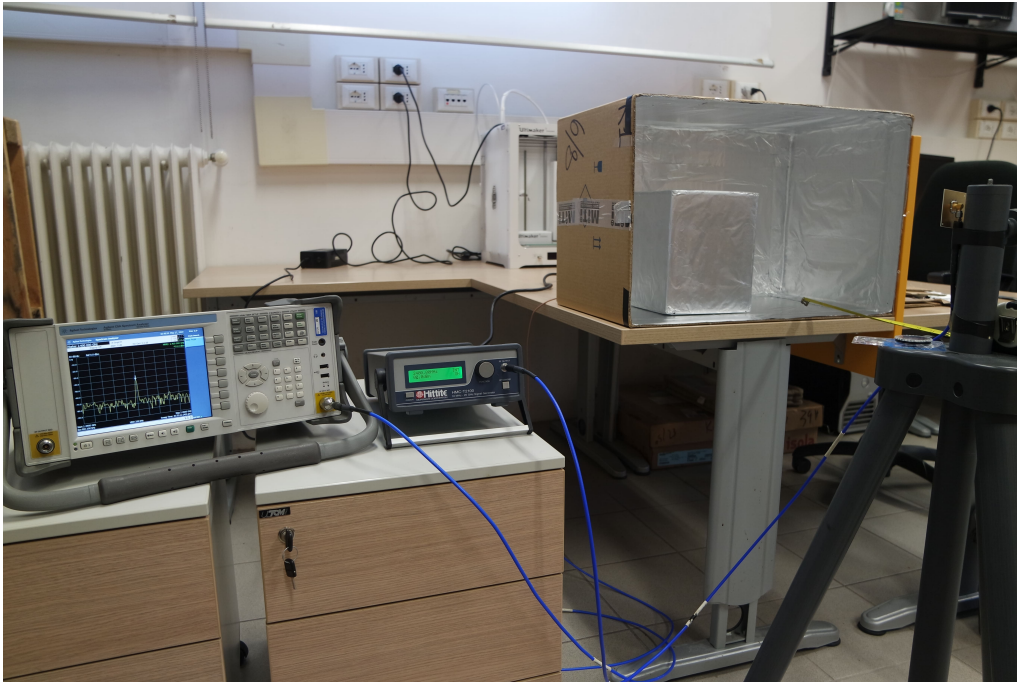


FIGURE 5.5: Snapshot of the realized testbed.

for sweep time 187.18 ms to average the impact of surrounding wireless devices working at the same frequency.

In order to quantify the difference between simulations and measurements, the cables' losses have been excluded from the received power using (4.7). Also, the mean P_{out}^{meas} for the aforementioned power range is calculated.

The bar chart shown in Figure 5.6 compares P_{out}^{sim} values for both TD simulation and the IE-based model with the received measured power in the prototype shown in Figure 5.5. The IE-based model evidently gives closer results to real world measurements than the TD solver.

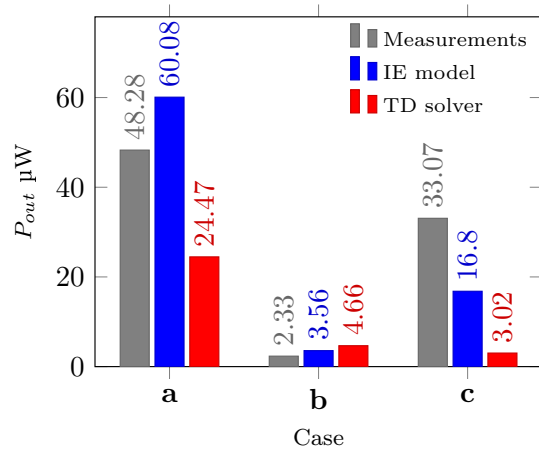


FIGURE 5.6: Comparison of the received power P_{out} between measurements (MEasurements), IE-based model (IE model), and the TD solver results (TD solver).

5.6 Conclusion

Using the reciprocity theorem, a formula that can benefit from the IE solver has been utilised to deploy this efficient solver, and hence allowing very efficient and fast calculation about twentynety times shorter than regular FD approach. This is potentially useful for WPT applications in semi reverberation metallic environments where the major concern is how much energy is transferred to the network terminals rather than a detailed EM problem diagnosis. Although it does not help to obtain other detailed information about coupling and de-tuning of elements due to nearby metallic structures, the results are closer to measurements than the other approach. The significant save of the simulation time makes it a worthwhile substitution of FD solver.

Although the FD solver is more rigorous and provides much more detail for full-wave simulations, it renders diminishing performance when the problem size exceeds, empirically, $5\lambda_0$.

The results reported here are interesting to investigate more pronounced scenarios with more complicated structure and aperture forms that can give

rise to a resonant cavity or surface wave behaviour. In addition to that, multi-frequency and ultra wide band energy harvesting applications can potentially benefit from a more developed version of this framework to foster the development of other future sensor networks types.

Chapter 6

Conculsion

The presented thesis summarises a three-year work period for the PhD programme on "Terahertz and Millimetric Rectennas." As explained and categorized in the text: the optimized energy harvesting system is based on the assumption of optimizing all of the receiver, the transmitter, and the link between the two.

The optimization of the receiver, which mainly comprises the nonlinear diode rectifier, is better approached by two categories. That is; low frequency and high frequency rectifier design. For the former, an explanation of the theory of operation and the design steps have been presented in subsection 2.2.1 and chapter 4, respectively. The literature review of this part reveals a well converged theoretical background among different authors.

On the other hand, the high frequency rectifier design reveals a more *individual* approach for the adopted models and the resulting output. As the oscillation frequency increases, the necessity arises to adopt quantum models for the rectifier device. With quantum models, there is merely a consensus among authors on the best model that describes the tunnelling rectifier operation. A brief recap of the frequently-utilized models is depicted in Figure 2.8 to help to order the models in terms of their theoretical basis, accuracy, etc. As shown in Figure 2.21 even for the same model, the adaptive mesh option leaves space for a try-and-error approach for the accuracy of the transmission

probability calculation. For all of the above, it is important to define a framework to treat these issues and industrialise the fabrication of these quantum tunnelling devices in any future trial.

The transmitter part, on the other hand, shows a very strong space-dependent behaviour between the Tx and Rx so that the transmitted power drops sharply within a very small distance as shown in Table 3.1. This is due to the well-known FSL and reflects how important it is to minimise the propagation and circuit losses. As discussed in the corresponding chapter, the TMA technique aims at minimising the circuit losses. Although the concept shows good and positive results for the lower GHz band, the co-simulation reveals some challenges for the 28 GHz band due to the corresponding nonlinear behaviour of the MIM diode in addition to the reasons explained in chapter 3. It might be said that a metric which measures the *similarity* between an ideal and a realistic diode can help estimate the performance of the TMA system.

The FDA strongly shows good development potentiality thanks to the space-dependent radiation pattern as shown in Figure 3.14. This is a very important aspect to treat the natural obstruction posed by the FSL law to focus the radiated power just at interested areas.

The propagation problem seems quite important for the next generation of distributed sensors. As the very soon application will be for middle-range applications, it is important to adopt the methods that take into account the near field behaviour without losing accuracy due to rounding and precision errors. Starting from a theorem to reach a relationship of the power transmitted from Tx to Rx using their electromagnetic fields gives a well-established framework to calculate the transmitted power towards the receiver. The initial work done in chapter 5 reveals good and encouraging results for planar interfacing surfaces. Therefore, more complicated surface forms may be studied in future research to make the findings more generalisable for structures of different shapes.

In the end, I would like to emphasise, apart from the scientific discussion, that a very important aspect of the research strategy is to respect the subjectivity of the presented material during the literature review. In other words, it is always difficult to balance between *positivism* which imposes repeatability of results and *phenomenology* which recognises the *individuality* of each experiment. I shall note that, particularly for the quantum part, it has been difficult to frequently obtain the same results from multiple papers given the same input parameters. A possible way to treat this problem is to consider using machine learning and artificial intelligence for industrial production instead of adopting a single theoretical framework. This concept is still at the beginning but seems to offer higher flexibility for mass production of devices that experience high level of subjectivity.

Appendix A

Source Codes

A.1 MATLAB Codes

```

1 %% ----- TUNNEL CONSTRUCTION
  -----
2 M={'M1','M2'}; % Step (transition) names.
3 xs = -2; %Start coordinates of the observation window
4 xe = 4; %End coordinates of the observation window
5 dx = 0.005; %Step size between subsequent calculations
6 xt = [0, 1]; % Steps x coordinates
7 Ep = [0, 0.8, 0]; %potential energy values before the first
  , between and after the last step.
8 m = 1; % Effective mass for the particle
9 E = linspace(1,5, 100); % particle energy
10
11 %% ----- TUNNEL MODELLING
  -----
12 [sys, E] = Epot(M, xt, Ep, m, E); % Wavevector system
  construction
13 TES = matrix(sys); % T matrix system construction
14 [x,psi,rho]=psirho(sys,dx,xs,xe,TES, E); % Calculation of
  wave function & prob

```

LISTING A.1: Wave function calculation for $U = 0.8\text{eV}$

```

1
2 %% ----- MODEL CONSTRUCTION
  -----
3 clear all
4 V = -3:0.05:3;
5 phis = 0.275;
6 phil = 0.75;
7 x_stp = 0.01;
8 L = 5;
9 K = 8;
10 T = 300;
11 Jtunm=Simmons(phis, phil, x_stp, V, L, K);
12 [~, Phix, x_zero, phiav] = Simpot(phis, phil, x_stp, V, L,
  K);
13 phim = max(Phix');
14 Jthm = 1.201e2*T^2*exp(-1.16e4*phim/T).*(1-exp(-1.16e4*abs(
  V)/T));

```

15 J = Jtunm + Jthm;

LISTING A.2: Main script to calculate Simmons tunnelling current

```

1 %% *****Simmons model for a tunneling diode
  *****
2 % This file is based on the original Simmons model
  suggested by Simmons in
3 % his paper "Generalized Formula for the Electric Tunnel
  Effect
4 % between Similar Electrodes Separated by a Thin Insulating
  Film" in the
5 % Journal of Applied Physics Vol.34, No. 6 (1963).
6 % Created on 20/02/2017
7 %
  *****
8 %The input arguments are shown below
9 function J=Simmons(phis, phil, x_stp, V, L, K)
10 %Where V in [v], Phis & phil 're in [eV] correspond to the
  lower (cathode) and upper (anode) barrier hights L in [
  nm], and K is the relative dielectric permittivity to
  account for the image potential effect
11 % The subsequent constants are the results of my
  calculations to facilitate computation on the machine
12 %***** CONSTANTS ALONG THE CODE
  *****
13 J0 = 6.2e10; % is in [A*Angestrom2/(V.cm2)]
14
15 %***** Approximations *****
16 B =1; %integral correction coefficient and is considered =1
  for ease;
17 %s = L; %Barrier thickness in [nm]is considered to be
  approximately equal to the physical one disregarding the
  image potential effect
18
19 %***** RUN *****
20 switch nargin
21 case 6
22 % Get barrier function, zeros crossing, and average over
  higher Fermi:
23 [x, Phix, x_zero, phiav] = Simpot(phis, phil, x_stp, V, L,
  K);
24 dels = 10*(x_zero(:, 2) - x_zero(:, 1))'; % Now delta s is
  in Angestrom units
25 phiav = phiav'; %Transpose the averaged phi matrix
26 S1 = phiav.*exp(-1.025*dels.*sqrt(phiav));
27 S2 = (phiav + abs(V)).*exp(-1.025*dels.*sqrt(phiav + abs(V)
  ));
28 J = J0*(S1 - S2)./(B*dels).^2;
29 %The 1.025 constant results from multiplying several
  constants
30
31 case 5
32 % Get barrier function, zeros crossing, and average over
  higher Fermi:
33 [x, Phix, x_zero, phiav] = Simpot(phis, phil, x_stp, V, L);
34 dels = 10*(x_zero(:, 2) - x_zero(:, 1))'; % Now delta s is
  in Angestrom units
35 phiav = phiav'; %Transpose the averaged phi matrix
36 S1 = phiav.*exp(-1.025*dels.*sqrt(phiav));

```

```

37 S2 = (phiav + abs(V)).*exp(-1.025*dels.*sqrt(phiav + abs(V)
    ));
38 J = J0*(S1 - S2)./(B*dels).^2;
39 %The 1.025 constant results from multiplying several
    constants
40 otherwise
41 disp('Invalid entry, please try again');
42 end;

```

LISTING A.3: Tunneling current calculation based on Simmons model [34]

```

1 %% ***** Potential barrier function *****
2 %Mazen Shanawani 17/02/2017
3 function [x, Phix, x_zero, phiav] = Simpot(phis, phil,
    x_stp, v, L, K) %Phix = Simpot(phis, phil, x, L, K, v)
4 % ***** Where *****
5 % phis is the smaller barrier height (cathode) %phil is the
    larger barrier height (anode)
6 % x_stp is the x axis step in [nm]
7 % L is the insulator thickness in [nm]
8 % v is the voltage range matrix (user defined)
9 % K is the relative dielectricity constant AT HIGH
    FREQUENCIES
10 % Phix is a 2D matrix with rows representing Phi(x) values
    WRT x coordinates entered above.
11 % The function can calculate with/without image potential
    included based on nargin.
12 x_zero= zeros(length(v), 2); %declare x_zero
13 phiav = zeros(length(v), 1); %declare phiav
14 switch nargin
15 case 6
16 % ***** Attnetion *****
17 % The hyperbolic term is just an approximation, DON'T PASS
    ZERO VALUES FOR
18 % X. Sugg: start from 0.05 [nm].
19 x = 0.05:x_stp:L-0.05;
20 Phix = zeros(length(v), length(x)); %declare Phix for speed
21 fun = @(xi, ph1, ph2, vlt, thick, dielec) ph1-(ph1 - ph2 +
    vlt).*xi/thick - 0.288*thick./(dielec*xi.*(thick -xi));
22 for l = 1: length(v)
23 if v(l)>=0 % Forward bias & phis has the lower voltage
24 %The following finds the phi(x) function
25 Phix(l, :) = fun(x, phis, phil, v(l), L, K);
26 %The following finds the intersection points with the upper
    Fermi level
27 x_zero(l, :) = insecphi(phis, phil, v(l), L, K);
28 %The following integrates the phi(x) over the range from s1
    to s2 as stated by Simmons. The integral results has
    been found by integrating the potential equation.
29 phiav(l, 1) = (phis*(x_zero(l, 2) - x_zero(l, 1)) - ...
30 (phis - phil + v(l))*(x_zero(l, 2)^2 - x_zero(l, 1)^2)/(2*L
    ) - ...
31 0.288*log(x_zero(l, 2)/x_zero(l, 1))/K +...
32 0.288*log((L - x_zero(l, 2))/(L - x_zero(l, 1)))/K)...
33 /(x_zero(l, 2) - x_zero(l, 1));
34 else % Reverse bias & phil has the lower voltage
35 %Everything is repeated here for the negative v
36 Phix(l, :) = fun(x, phil, phis, -v(l), L, K);
37 % The insecphi function NEEDS the negative voltage to know
38 % how to calculate

```

```

39 x_zero(1, :) = insecphi(phis, phil, v(1), L, K);
40 phiav(1, 1) = (phil*(x_zero(1, 2) - x_zero(1, 1)) - ...
41 (phil - phis - v(1))*(x_zero(1, 2)^2 - x_zero(1, 1)^2)/(2*L
    ) - ...
42 0.288*log(x_zero(1, 2)/x_zero(1, 1))/K +...
43 0.288*log((L - x_zero(1, 2))/(L - x_zero(1, 1)))/K)...
44 /(x_zero(1, 2) - x_zero(1, 1));
45 end;
46 end;
47 case 5
48 x = 0:x_stp:L; % Calculation will be done without image
    potential
49 Phix = zeros(length(v), length(x)); %declare Phix for speed
50 fun = @(xi, ph1, ph2, vlt, thick) ph1-(ph1 - ph2 + vlt).*xi
    /thick ;
51 for l = 1: length(v)
52 if v(l)>=0 % Forward bias & phis has the lower voltage
53 %The following finds the phi(x) function
54 Phix(l, :) = fun(x, phis, phil, v(1), L);
55 %Phix(l, :) = phis -(phis - phil +v(1)).*x/L -0.288*L/(K*x
    .*(L-x));
56 %The following finds the intersection points with the upper
    Fermi level
57 x_zero(1, :) = insecphi(phis, phil, v(1), L);
58 %The following integrates the phi(x) over the range from s1
    to s2
59 %as stated by Simmons
60 phiav(1, 1) = (phis*(x_zero(1, 2) - x_zero(1, 1)) - ...
61 (phis - phil + v(1))*(x_zero(1, 2)^2 - x_zero(1, 1)^2)/(2*L
    ))...
62 /(x_zero(1, 2) - x_zero(1, 1));
63 else % Reverse bias & phil has the lower voltage
64 %Everything is repeated here for the negative v
65 Phix(l, :) = fun(x, phil, phis, -v(1), L);
66 % The insecphi function NEEDS the negative voltage to know
67 % how to calculate
68 x_zero(1, :) = insecphi(phis, phil, v(1), L);
69 phiav(1, 1) = (phil*(x_zero(1, 2) - x_zero(1, 1)) - ...
70 (phil - phis + v(1))*(x_zero(1, 2)^2 - x_zero(1, 1)^2)/(2*L
    ))...
71 /(x_zero(1, 2) - x_zero(1, 1));
72 end;
73 end;
74 otherwise
75 disp('Invalid input, please try again');
76 end;

```

LISTING A.4: Potential barrier calculation function

```

1 function out = calc_V(in, x_grd, K_LRS, L_LRS, V_bias)
2 %This function will calculate the potential energy profile
    across the whole system structure using the work
    function and affinity values provided through the matrix
    (in).
3 %Where in: Is the work function and affinities matrix
4 out = zeros(1, length(x_grd)+1);
5 %
    #####
6 %
    VOLTAGE PROFILE FINDING STEPS

```

```

7 %
  #####

8 %A) VOLTAGE DROP ACROSS DIFFERENT INSULATORS:
9 %Find the voltage drop across each layer taking into
  account the electric
10 %displacement continuity condition.
11 Vj = zeros(size(K_LRS));
12 SUM = sum(L_LRS./K_LRS);
13 Vj = (V_bias -in(end) + in(1))*(L_LRS./K_LRS)/SUM ;
14 clear SUM
15
16 %B)Find the border points between different layers and
  their indices
17 x_brd = find_bord(x_grd, L_LRS);
18 x_brd_ind = zeros(size(x_brd));
19 for i = 1:length(x_brd)
20 x_brd_ind(i) = find(x_grd == x_brd(i));
21 end;
22
23 %C)Find the cumulative matrix of voltage drop across the
  layers
24 cum_Vj = [0 cumsum(Vj)]; %We pad the voltage drop matrix
  with 0 from the
25 %left because we have no accumulative voltage drop in the
  first layer
26
27 %D)Loop through to build the potential energy profile
28 j = 0; %Index for the layer order
29 %The first element out(1)= 0 is obviously zero
30 %The middle elements are calculated as follows
31 for i=2:(length(x_grd))
32 if sum(find(i-1 == x_brd_ind)) > 0 %If we are at a border
  point, then
33 j = j+1;
34 end
35 out(i) = in(1) ;
36 out(i) = out(i) - in(j+1) ;
37 out(i) = out(i) - cum_Vj(j) ;
38 out(i) = out(i) -Vj(j)*(x_grd(i)-x_brd(j))/L_LRS(j);
39 end
40 %The last element is calculated according to the following
  equation
41 out(end) = in(1) - in(end) - cum_Vj(end) ;

```

LISTING A.5: Potential profile calculation for multi-insulatore structures

```

1
2 '-----List of variables used
  in this script-----
3 Public mcr_freq As Double 'Multiples of GHz
4 Public mcr_freq_step As Double 'Steps of MHz for the FDA
  array
5 Public mcr_freq_var As Double 'Inner frequency variable
  inside the DO loop
6 Public mcr_port_num As Integer 'Number of ports for FDA
  array
7 Public F_folder As String 'Destination folder name
8
9 Dim i As Integer 'Variable for the DOI loop

```

```

10 Dim k As Integer 'Variable for the inner FOR loop
11
12 DialogFunc% = True 'do not exit the dialog
13
14 mcr_freq = CDBl(DlgText("freq"))
15 mcr_freq_step = CDBl(DlgText("freq_step"))
16 mcr_port_num = CInt(DlgText("port_num"))
17
18 i = 0
19 'Open myFile For Output As #1
20 Do While i <= mcr_port_num - 1
21 mcr_freq_var = mcr_freq + i*mcr_freq_step
22 F_folder = "..\..\..\F"&Replace(CStr(mcr_freq_var), ".", "_")
23 MkDir(F_folder)
24
25 'Write #1, "Folder Created for F" , mcr_freq_Int, "_" ,
    mcr_freq_var
26 For k = 1 To mcr_port_num STEP 1
27
28 SelectTreeItem("Farfields\farfield (f="&CStr(mcr_freq_var)&
    ") ["&CStr(k)&"]")
29 'Write #1, "file farfield (f=", mcr_freq_Int, ".",
    mcr_freq_var, ") [" , k, "]", "Selected!"
30 With ASCIIExport
31 .Reset
32 .FileName(F_folder & "\E1_"&CStr(k)&".txt")
33 .Execute
34 End With
35 'Write #1, "E1_", k, ".txt Created inside F", mcr_freq_Int,
    "_", mcr_freq_var
36 Next
37 i = i + 1
38 Loop
39 'Close #1

```

LISTING A.6: Nested loops for radiation pattern exportation
from CST Microwave Studio®

Bibliography

- [1] F. Landis, O. Schenker, M Tovar Reaños, C. Vonnahme, and S. Zitzelsberger, “An overview on current climate policies in the european union and its member states”, *ENTRACTE Project Report*, no. 1, 2013.
- [2] D. Evans, “The internet of things: How the next evolution of the internet is changing everything”, *CISCO white paper*, vol. 1, no. 2011, pp. 1–11, 2011.
- [3] J. Mulins, “Breaking the noise barrier: Enter the phonon computer”, *NewScientist*, 2010. [Online]. Available: <https://www.newscientist.com/article/mg20827801-500-breaking-the-noise-barrier-enter-the-phonon-computer/>.
- [4] B. Zaghari, E. Rustighi, and M. G. Tehrani, “Phase dependent nonlinear parametrically excited systems”, *Journal of Vibration and Control*, vol. 25, no. 3, pp. 497–505, 2019. DOI: [10.1177/1077546318783566](https://doi.org/10.1177/1077546318783566). [Online]. Available: <https://doi.org/10.1177/1077546318783566>.
- [5] F. Cottone, H. Vocca, and L. Gammaitoni, “Nonlinear energy harvesting”, *Phys. Rev. Lett.*, vol. 102, p. 080 601, 8 2009. DOI: [10.1103/PhysRevLett.102.080601](https://doi.org/10.1103/PhysRevLett.102.080601). [Online]. Available: <https://link.aps.org/doi/10.1103/PhysRevLett.102.080601>.
- [6] M. Shanawani, D. Masotti, and A. Costanzo, “Thz rectennas and their design rules”, *Electronics*, vol. 6, no. 4, p. 99, 2017.

- [7] Y.-S. Chen and C.-W. Chiu, "Maximum achievable power conversion efficiency obtained through an optimized rectenna structure for rf energy harvesting", *IEEE Transactions on Antennas and Propagation*, vol. 65, no. 5, pp. 2305–2317, 2017.
- [8] Wikipedia. (2017). Edmond becquerel — wikipedia, the free encyclopedia. [Online; accessed 7-August-2017], [Online]. Available: https://en.wikipedia.org/w/index.php?title=Edmond_Becquerel&oldid=791838776.
- [9] n.a., "April 25, 1954: Bell labs demonstrates the first practical silicon solar cell", *APS Physics*, 2009. [Online]. Available: <https://www.aps.org/publications/apsnews/200904/physicshistory.cfm>.
- [10] W. Shockley and H. J. Queisser, "Detailed balance limit of efficiency of p-n junction solar cells", *Journal of applied physics*, vol. 32, no. 3, pp. 510–519, 1961.
- [11] F. Sohrabi, A. Nikniazi, and H. Movla, "Optimization of third generation nanostructured silicon- based solar cells", in *Solar Cells - Research and Application Perspectives*, A. Morales-Acevedo, Ed., Rijeka: InTech, 2013, ch. 01. DOI: [10.5772/51616](https://doi.org/10.5772/51616). [Online]. Available: <http://dx.doi.org/10.5772/51616>.
- [12] G. Moddel and S. Grover, *Rectenna solar cells*. New York: Springer, 2013, vi, 399 p. 2013945873 Garret Moddel, Sachit Grover, editors. ill. (some col.) ; 24 cm. Includes bibliographical references and index., ISBN: 9781461437154 1461437156. DOI: [10.1007/978-1-4614-3716-1](https://doi.org/10.1007/978-1-4614-3716-1). [Online]. Available: <http://www.springer.com/it/book/9781461437154>.
- [13] L. Kazmerski, D Gwinner, and A Hicks, "Best research cell efficiencies", *National Renewable Energy Laboratory*, vol. 2, 2010.

- [14] R. King, D. Law, K. Edmondson, C. Fetzer, G. Kinsey, H Yoon, R. Sherif, and N. Karam, "40% efficient metamorphic gainp/ gainas/ ge multijunction solar cells", *Applied physics letters*, vol. 90, no. 18, p. 183516, 2007.
- [15] G. Michael and G. Alan, "A manufacturing cost analysis relevant to single- and dual-junction photovoltaic cells fabricated with iii-vs and iii- vs grown on czochralski silicon", NREL, Report, 2013. [Online]. Available: <http://www.nrel.gov/docs/fy14osti/60126.pdf>.
- [16] Y. Yang and J. You, "Make perovskite solar cells stable.", *Nature*, vol. 544, no. 7649, pp. 155–156, 2017.
- [17] F. Habbal, W. C. Danchi, and M. Tinkham, "Photon-assisted tunneling at 246 and 604 ghz in small-area superconducting tunnel junctions", *Applied Physics Letters*, vol. 42, no. 3, pp. 296–298, 1983. DOI: [10.1063/1.93885](https://doi.org/10.1063/1.93885). eprint: <http://dx.doi.org/10.1063/1.93885>. [Online]. Available: <http://dx.doi.org/10.1063/1.93885>.
- [18] C. Fumeaux, W. Herrmann, F. K. Kneubühl, and H. Rothuizen, "Nanometer thin-film ni–nio–ni diodes for detection and mixing of 30 thz radiation", *Infrared Physics & Technology*, vol. 39, no. 3, pp. 123–183, 1998, ISSN: 1350-4495. DOI: [https://doi.org/10.1016/S1350-4495\(98\)00004-8](https://doi.org/10.1016/S1350-4495(98)00004-8). [Online]. Available: <http://www.sciencedirect.com/science/article/pii/S1350449598000048>.
- [19] G. Moddel, "Will rectenna solar cells be practical?", in *Rectenna Solar Cells*. Springer, 2013, pp. 3–24.
- [20] W. C. Brown, "The microwave powered helicopter", *Journal of Microwave Power*, vol. 1, no. 1, pp. 1–20, 1966, ISSN: 0022-2739. DOI: [10.1080/00222739.1966.11688626](https://doi.org/10.1080/00222739.1966.11688626). [Online]. Available: <http://dx.doi.org/10.1080/00222739.1966.11688626>.

- [21] W. C. Brown, "Optimization of the efficiency and other properties of the rectenna element", in *IEEE-MTT-S International Microwave Symposium*, 1976, pp. 142–144. DOI: [10.1109/MWSYM.1976.1123673](https://doi.org/10.1109/MWSYM.1976.1123673).
- [22] P Koert, J Cha, and M Machina, "35 and 94 ghz rectifying antenna systems", in *SPS 91-Power from Space*, 1991, pp. 541–547.
- [23] H.-K. Chiou and I.-S. Chen, "High-efficiency dual-band on-chip rectenna for 35-and 94-ghz wireless power transmission in 0.13- μ m cmos technology", *IEEE Transactions on Microwave Theory and Techniques*, vol. 58, no. 12, pp. 3598–3606, 2010.
- [24] E. Donchev, J. S. Pang, P. M. Gammon, A. Centeno, F. Xie, P. K. Petrov, J. D. Breeze, M. P. Ryan, D. J. Riley, and N. M. Alford, "The rectenna device: From theory to practice (a review)", *MRS Energy & Sustainability-A Review Journal*, vol. 1, 2014.
- [25] D. A. Bandurin, D. Svintsov, I. Gayduchenko, S. G. Xu, A. Principi, M. Moskotin, I. Tretyakov, D. Yagodkin, S. Zhukov, T. Taniguchi, *et al.*, "Resonant terahertz detection using graphene plasmons", *Nature Communications*, vol. 9, no. 1, p. 5392, 2018.
- [26] E. Javadi, A. Lisauskas, M. Shahabadi, N. Masoumi, J. Zhang, J. Matukas, and H. G. Roskos, "Terahertz Detection With a Low-Cost Packaged GaAs High-Electron-Mobility Transistor", *IEEE Transactions on Terahertz Science and Technology*, vol. 9, no. 1, pp. 27–37, 2019, ISSN: 2156-342X. DOI: [10.1109/TTHZ.2018.2877908](https://doi.org/10.1109/TTHZ.2018.2877908).
- [27] M. Dragoman and M. Aldrigo, "Graphene rectenna for efficient energy harvesting at terahertz frequencies", *Applied Physics Letters*, vol. 109, no. 11, p. 113 105, 2016, ISSN: 0003-6951.

- [28] Q. Awais, Y. Jin, H. T. Chattha, M. Jamil, H. Qiang, and B. A. Khawaja, "A compact rectenna system with high conversion efficiency for wireless energy harvesting", *IEEE Access*, vol. 6, pp. 35 857–35 866, 2018. DOI: [10.1109/ACCESS.2018.2848907](https://doi.org/10.1109/ACCESS.2018.2848907).
- [29] R Corkish, M. Green, and T Puzzer, "Solar energy collection by antennas", *Solar Energy*, vol. 73, no. 6, pp. 395–401, 2002.
- [30] S. J. Byrnes, R. Blanchard, and F. Capasso, "Harvesting renewable energy from earth's mid-infrared emissions", *Proceedings of the National Academy of Sciences*, vol. 111, no. 11, pp. 3927–3932, 2014.
- [31] A. Natarajan, S. K. Reynolds, M. Tsai, S. T. Nicolson, J. C. Zhan, D. G. Kam, D. Liu, Y. O. Huang, A. Valdes-Garcia, and B. A. Floyd, "A fully-integrated 16-element phased-array receiver in SiGe BiCMOS for 60-GHz communications", *IEEE Journal of Solid-State Circuits*, vol. 46, no. 5, pp. 1059–1075, May 2011, ISSN: 0018-9200. DOI: [10.1109/JSSC.2011.2118110](https://doi.org/10.1109/JSSC.2011.2118110).
- [32] X. Gu, A. Valdes-Garcia, A. Natarajan, B. Sadhu, D. Liu, and S. K. Reynolds, "W-band scalable phased arrays for imaging and communications", *IEEE Communications Magazine*, vol. 53, no. 4, pp. 196–204, Apr. 2015, ISSN: 0163-6804. DOI: [10.1109/MCOM.2015.7081095](https://doi.org/10.1109/MCOM.2015.7081095).
- [33] J. G. Simmons, "Potential barriers and emission-limited current flow between closely spaced parallel metal electrodes", *Journal of Applied Physics*, vol. 35, no. 8, pp. 2472–2481, 1964.
- [34] J. G. Simmons, "Generalized formula for the electric tunnel effect between similar electrodes separated by a thin insulating film", *Journal of applied physics*, vol. 34, no. 6, pp. 1793–1803, 1963.
- [35] H. Torrey and C. Whitmer, "Crystal rectifiers", *McGraw-Hill New York*, vol. 948, 1948.

- [36] S. Krishnan, E. Stefanakos, and S. Bhansali, "Effects of dielectric thickness and contact area on current–voltage characteristics of thin film metal–insulator–metal diodes", *Thin Solid Films*, vol. 516, no. 8, pp. 2244–2250, 2008.
- [37] S. Grover and G. Moddel, "Engineering the current–voltage characteristics of metal–insulator–metal diodes using double-insulator tunnel barriers", *Solid-State Electronics*, vol. 67, no. 1, pp. 94–99, 2012.
- [38] P. Periasamy, H. L. Guthrey, A. I. Abdulagatov, P. F. Ndione, J. J. Berry, D. S. Ginley, S. M. George, P. A. Parilla, and R. P. O'Hayre, "Metal–insulator–metal diodes: Role of the insulator layer on the rectification performance", *Advanced Materials*, vol. 25, no. 9, pp. 1301–1308, 2013.
- [39] M. L. Chin, P. Periasamy, T. P. O'Regan, M. Amani, C. Tan, R. P. O'Hayre, J. J. Berry, R. M. Osgood III, P. A. Parilla, and D. S. Ginley, "Planar metal–insulator–metal diodes based on the nb/nb₂o₅/x material system", *Journal of Vacuum Science & Technology B, Nanotechnology and Microelectronics: Materials, Processing, Measurement, and Phenomena*, vol. 31, no. 5, p. 051 204, 2013, ISSN: 2166-2746.
- [40] V. Rizzoli, A. Lipparini, A. Costanzo, F. Mastri, C. Cecchetti, A. Neri, and D. Masotti, "State-of-the-art harmonic-balance simulation of forced nonlinear microwave circuits by the piecewise technique", *IEEE transactions on microwave theory and techniques*, vol. 40, no. 1, pp. 12–28, 1992, ISSN: 0018-9480.
- [41] University of Bologna. (Sep. 27, 2019). NONLIN, Program for Analysis and Optimization of Nonlinear Microwave Circuits Operating in a Periodic or Quasi-Periodic Steady-State Regime. version 9. Proprietary program.
- [42] D. J. Griffiths and D. F. Schroeter, *Introduction to quantum mechanics*. Cambridge University Press, 2018.

- [43] Wikipedia. (2017). Floquet theory — wikipedia, the free encyclopedia. [Online; accessed 21-August-2017], [Online]. Available: https://en.wikipedia.org/w/index.php?title=Floquet_theory&oldid=790708503.
- [44] W. Truscott, "Wave functions in the presence of a time-dependent field: Exact solutions and their application to tunneling", *Physical review letters*, vol. 70, no. 13, p. 1900, 1993.
- [45] T. Swirbel, "Zero-defect sputter deposition metallization method for high volume manufacturing of grafted multilayer thin film modules", *and Manufacturing Technology IEEE Transactions on Components, Hybrids*, vol. 16, no. 1, pp. 1–5, Feb. 1993. DOI: [10.1109/33.214853](https://doi.org/10.1109/33.214853).
- [46] O. Pujol, R. Carles, and J.-P. Pérez, "Quantum propagation and confinement in 1d systems using the transfer-matrix method", *European Journal of Physics*, vol. 35, no. 3, p. 035 025, 2014.
- [47] O. Pujol. (Feb. 12, 2014). Quantum propagation and confinement in 1d systems using the transfer-matrix method, [Online]. Available: https://www-loa.univ-lille1.fr/profil/u/Olivier_Pujol.html.
- [48] B. R. Franciscatto, V. Freitas, J. Duchamp, C. Defay, and T. P. Vuong, "High-efficiency rectifier circuit at 2.45 GHz for low-input-power RF energy harvesting", in *Proc. European Microwave Conf*, Oct. 2013, pp. 507–510. DOI: [10.23919/EuMC.2013.6686703](https://doi.org/10.23919/EuMC.2013.6686703).
- [49] A. S. Boaventura and N. B. Carvalho, "Maximizing DC power in energy harvesting circuits using multisine excitation", in *Proc. IEEE MTT-S Int. Microwave Symp*, Jun. 2011, pp. 1–4. DOI: [10.1109/MWSYM.2011.5972612](https://doi.org/10.1109/MWSYM.2011.5972612).
- [50] P. Spadoni, "Nonlinear /electromagnetic co-simulation of microwaves and millimeter-waves links", PhD thesis, University of Bologna, 2008.

- [51] V. Rizzoli, A. Costanzo, D. Masotti, P. Spadoni, and A. Neri, "Prediction of the end-to-end performance of a microwave/RF link by means of nonlinear/electromagnetic co-simulation", *IEEE Transactions on Microwave Theory and Techniques*, vol. 54, no. 12, pp. 4149–4160, Dec. 2006. DOI: [10.1109/TMTT.2006.885566](https://doi.org/10.1109/TMTT.2006.885566).
- [52] D. Masotti, A. Costanzo, P. Rocca, and A. Massa, "The importance of nonlinear/electromagnetic co-simulation on time-modulated array synthesis", in *Proc. IEEE Int. Symp. Antennas and Propagation (APSURSI)*, Jun. 2016, pp. 701–702. DOI: [10.1109/APS.2016.7696059](https://doi.org/10.1109/APS.2016.7696059).
- [53] F. E. Curtis, O. Schenk, and A. Wächter, "An interior-point algorithm for large-scale nonlinear optimization with inexact step computations", *SIAM Journal on Scientific Computing*, vol. 32, no. 6, pp. 3447–3475, 2010.
- [54] Skyworks, "A level detector design for dual-band gsm-pcs handsets", Skyworks, Report, 2014. [Online]. Available: http://www.skyworksinc.com/uploads/documents/APN1014_200324B.pdf.
- [55] A. Cuevas, D. Macdonald, and R. A. Sinton, "Characterization and diagnosis of silicon wafers, ingots, and solar cells", in *McEvoy's Handbook of Photovoltaics*, Elsevier, 2018, pp. 1119–1154.
- [56] G Ariño-Estrada, M Chmeissani, G de Lorenzo, M Kolstein, C Puigdemonges, J García, and E Cabruja, "Measurement of mobility and lifetime of electrons and holes in a schottky CdTe diode", *Journal of Instrumentation*, vol. 9, no. 12032, pp. 1–6, 2014. DOI: [10.1088/1748-0221/9/12/c12032](https://doi.org/10.1088/1748-0221/9/12/c12032). [Online]. Available: <https://doi.org/10.1088/1748-0221/9/12/c12032>.
- [57] HyperPhysics, *Wien's displacement law*, [Online; accessed 14-August-2017], 2006. [Online]. Available: <http://ef.engr.utk.edu/hyperphysics/hbase/wien.html>.

- [58] T. O'Regan, M. Chin, C. Tan, and A. Birdwell, "Modeling, fabrication, and electrical testing of metal-insulator-metal diode", Army Research Lab Adelphi MD Sensors And Electron Devices Directorate, Tech. Rep., 2011.
- [59] M. Hathaikarn, "Electrical properties of niobium based oxides-ceramics and single crystal fibers grown by the laser-heated pedestal growth (lhpg) technique", *A thesis in materials of dissertation for the degree of doctor of philosophy. The Pennsylvania State University, The Graduate School Intercollege Graduate Program in Materials*, vol. 319, 2003.
- [60] M. N. Polyanskiy. (). Refractive index database, [Online]. Available: <https://refractiveindex.info> (visited on 08/30/2017).
- [61] H. Mashaal and J. M. Gordon, "Solar and thermal aperture antenna coherence performance limits", in *Rectenna Solar Cells*. Springer, 2013, pp. 69–86.
- [62] S. Divitt and L. Novotny, "Spatial coherence of sunlight and its implications for light management in photovoltaics", *Optica*, vol. 2, no. 2, pp. 95–103, 2015.
- [63] M Büttiker and R Landauer, "Traversal time for tunneling", *Physical Review Letters*, vol. 49, no. 23, p. 1739, 1982.
- [64] H. Liu, "Time-dependent approach to double-barrier quantum well oscillators", *Applied physics letters*, vol. 52, no. 6, pp. 453–455, 1988.
- [65] J. R. Tucker and M. J. Feldman, "Quantum detection at millimeter wavelengths", *Reviews of Modern Physics*, vol. 57, no. 4, p. 1055, 1985.
- [66] A Sanchez, C. Davis Jr, K. Liu, and A Javan, "The mom tunneling diode: Theoretical estimate of its performance at microwave and infrared frequencies", *Journal of Applied Physics*, vol. 49, no. 10, pp. 5270–5277, 1978, ISSN: 0021-8979.

- [67] B. Jonsson and S. T. Eng, "Solving the schrodinger equation in arbitrary quantum-well potential profiles using the transfer matrix method", *IEEE journal of quantum electronics*, vol. 26, no. 11, pp. 2025–2035, 1990.
- [68] C. S. Lent and D. J. Kirkner, "The quantum transmitting boundary method", *Journal of Applied Physics*, vol. 67, no. 10, pp. 6353–6359, 1990. DOI: 10.1063/1.345156. eprint: <http://dx.doi.org/10.1063/1.345156>. [Online]. Available: <http://dx.doi.org/10.1063/1.345156>.
- [69] P. Tien and J. Gordon, "Multiphoton process observed in the interaction of microwave fields with the tunneling between superconductor films", *Physical Review*, vol. 129, no. 2, p. 647, 1963.
- [70] A Mayer, M. Chung, B. Weiss, N. Miskovsky, and P. Cutler, "Three-dimensional analysis of the rectifying properties of geometrically asymmetric metal-vacuum-metal junctions treated as an oscillating barrier", *Physical Review B*, vol. 78, no. 20, p. 205 404, 2008.
- [71] S. Datta and M. Anantram, "Steady-state transport in mesoscopic systems illuminated by alternating fields", *Physical Review B*, vol. 45, no. 23, p. 13761, 1992.
- [72] Wikipedia. (2017). Dirac equation — wikipedia, the free encyclopedia. [Online; accessed 21-August-2017], [Online]. Available: https://en.wikipedia.org/w/index.php?title=Dirac_equation&oldid=796044311.
- [73] Z. J. Zhu, "Graphene geometric diodes for optical rectennas", PhD thesis, University of Colorado at Boulder, 2014.
- [74] S. E. Laux, A. Kumar, and M. V. Fischetti, "Analysis of quantum ballistic electron transport in ultrasmall silicon devices including space-charge and geometric effects", *Journal of Applied Physics*, vol. 95, no. 10, pp. 5545–5582, 2004. DOI: 10.1063/1.1695597. [Online]. Available: <https://doi.org/10.1063/1.1695597>.

- [75] W Schottky, "Abweichungen vom ohmschen gesetz in halbleitern", *Phys. Zeitschr*, vol. 41, pp. 570–573, 1940.
- [76] M. Heiblum, S. Wang, J Whinnery, and T Gustafson, "Characteristics of integrated mom junctions at dc and at optical frequencies", *IEEE Journal of Quantum Electronics*, vol. 14, no. 3, pp. 159–169, 1978.
- [77] Z. Zhu, S. Joshi, S. Grover, and G. Moddel, "Geometric diodes for optical rectennas", in *Rectenna Solar Cells*. Springer, 2013, pp. 209–227.
- [78] D. Dragoman and M. Dragoman, "Geometrically induced rectification in two-dimensional ballistic nanodevices", *Journal of Physics D: Applied Physics*, vol. 46, no. 5, p. 055 306, 2013.
- [79] M. Y. Han, B. Özyilmaz, Y. Zhang, and P. Kim, "Energy band-gap engineering of graphene nanoribbons", *Physical review letters*, vol. 98, no. 20, p. 206 805, 2007.
- [80] M. Dragoman, A. Dinescu, and D. Dragoman, "On-wafer graphene diodes for high-frequency applications", in *Solid-State Device Research Conference (ESSDERC), 2013 Proceedings of the European, IEEE, 2013*, pp. 322–325.
- [81] S. A. Stellingwerff, "Solar energy harvesting using graphene rectennas: A proof-of-concept study", Master's thesis, University of Twente, 2015.
- [82] S. Tongay, M Lemaitre, X Miao, B Gila, B. Appleton, and A. Hebard, "Rectification at graphene–semiconductor interfaces: Zero–gap semiconductor–based diodes", *Physical Review X*, vol. 2, no. 1, p. 011 002, 2012.
- [83] M. Paulsson, "Non equilibrium green's functions for dummies: Introduction to the one particle negf equations", *arXiv preprint cond-mat/0210519*, 2002.

- [84] Wikipedia. (2017). Perturbation theory (quantum mechanics) – wikipedia, the free encyclopedia. [Online; accessed 19-August-2017], [Online]. Available: [https://en.wikipedia.org/w/index.php?title=Perturbation_theory_\(quantum_mechanics\)&oldid=793439215](https://en.wikipedia.org/w/index.php?title=Perturbation_theory_(quantum_mechanics)&oldid=793439215).
- [85] I. E. Hashem, N. H. Rafat, and E. A. Soliman, "Theoretical study of metal-insulator-metal tunneling diode figures of merit", *IEEE Journal of Quantum Electronics*, vol. 49, no. 1, pp. 72–79, 2013.
- [86] S. Grover and G. Moddel, "Metal single-insulator and multi-insulator diodes for rectenna solar cells", in *Rectenna Solar Cells*. Springer, 2013, pp. 89–109.
- [87] N. Miskovsky, P. Cutler, P. Lerner, A. Mayer, B. Willis, D. Zimmerman, G. Weisel, and T. Sullivan, "Nanoscale rectennas with sharp tips for absorption and rectification of optical radiation", English (US), in *Rectenna Solar Cells*. United States: Springer New York, Feb. 2014, vol. 9781461437161, pp. 135–161, ISBN: 1461437156. DOI: [10.1007/978-1-4614-3716-1_7](https://doi.org/10.1007/978-1-4614-3716-1_7).
- [88] S. Joshi and G. Moddel, "Efficiency limits of rectenna solar cells: Theory of broadband photon-assisted tunneling", *Applied Physics Letters*, vol. 102, no. 8, p. 083 901, 2013.
- [89] J. Tucker, "Quantum limited detection in tunnel junction mixers", *IEEE Journal of Quantum Electronics*, vol. 15, no. 11, pp. 1234–1258, Nov. 1979. DOI: [10.1109/JQE.1979.1069931](https://doi.org/10.1109/JQE.1979.1069931).
- [90] W. R. Smythe, *Static and Dynamic Electricity*. McGraw-Hill Book Company, Inc., New York, 1950.
- [91] S. C. Miller Jr and R. Good Jr, "A wkb-type approximation to the schrödinger equation", *Physical Review*, vol. 91, no. 1, p. 174, 1953.

- [92] W. H. Hayt and J. A. Buck, *Engineering electromagnetics*. McGraw-Hill New York, 2001, vol. 6.
- [93] C. Jirauschek, "Accuracy of transfer matrix approaches for solving the effective mass schrödinger equation", *IEEE Journal of Quantum Electronics*, vol. 45, no. 9, pp. 1059–1067, 2009.
- [94] A. K. Ghatak, K. Thyagarajan, and M. R. Shenoy, "A novel numerical technique for solving the one-dimensional schroedinger equation using matrix approach-application to quantum well structures", *IEEE Journal of Quantum Electronics*, vol. 24, no. 8, pp. 1524–1531, Aug. 1988. DOI: [10.1109/3.7079](https://doi.org/10.1109/3.7079).
- [95] M Kleefstra and G. Herman, "Influence of the image force on the band gap in semiconductors and insulators", *Journal of Applied Physics*, vol. 51, no. 9, pp. 4923–4926, 1980.
- [96] L. Wang and S. Rokhlin, "Stable reformulation of transfer matrix method for wave propagation in layered anisotropic media", *Ultrasonics*, vol. 39, no. 6, pp. 413–424, 2001, ISSN: 0041-624X. DOI: [https://doi.org/10.1016/S0041-624X\(01\)00082-8](https://doi.org/10.1016/S0041-624X(01)00082-8). [Online]. Available: <http://www.sciencedirect.com/science/article/pii/S0041624X01000828>.
- [97] A. Mayer and J.-P. Vigneron, "Transfer-matrix quantum-mechanical theory of electronic field emission from nanotips", *Journal of Vacuum Science & Technology B: Microelectronics and Nanometer Structures Processing, Measurement, and Phenomena*, vol. 17, no. 2, pp. 506–514, 1999. DOI: [10.1116/1.590586](https://doi.org/10.1116/1.590586). [Online]. Available: <https://avs.scitation.org/doi/abs/10.1116/1.590586>.
- [98] S. Grover. (Oct. 27, 2013). Metal-insulator diode simulator, University of Colorado, [Online]. Available: <http://ecee.colorado.edu/~moddel/QEL/MIMDiodeSim.zip>.

- [99] O. M. Probst, "Tunneling through arbitrary potential barriers and the apparent barrier height", *American Journal of Physics*, vol. 70, no. 11, pp. 1110–1116, 2002.
- [100] J. C. Slater, "Atomic radii in crystals", *The Journal of Chemical Physics*, vol. 41, no. 10, pp. 3199–3204, 1964.
- [101] The MathWorks, Inc. (Sep. 12, 2018). MATLAB R2018b Optimization Toolbox 8.1. version 2018b-8.1, [Online]. Available: <https://uk.mathworks.com/help/gads/genetic-algorithm.html>.
- [102] I. Z. Mitrovic, A. D. Weerakkody, N. Sedghi, S. Hall, J. F. Ralph, J. S. Wrench, P. R. Chalker, Z. Luo, and S. Beeby, "(invited) tunnel-barrier rectifiers for optical nantennas", *ECS Transactions*, vol. 72, no. 2, pp. 287–299, 2016, ISSN: 1938-6737.
- [103] M. Aldrigo, M. Dragoman, M. Modreanu, I. Povey, S. Iordanescu, D. Vasilache, A. Dinescu, M. Shanawani, and D. Masotti, "Harvesting Electromagnetic Energy in the V-Band Using a Rectenna Formed by a Bow Tie Integrated With a 6-nm-Thick Au/HfO₂/Pt Metal–Insulator–Metal Diode", *IEEE Transactions on Electron Devices*, vol. 65, no. 7, pp. 2973–2980, 2018, ISSN: 0018–9383. DOI: [10.1109/TED.2018.2835138](https://doi.org/10.1109/TED.2018.2835138).
- [104] A. Singh, R. Ratnadurai, R. Kumar, S. Krishnan, Y. Emirov, and S. Bhansali, "Fabrication and current–voltage characteristics of niox/zno based miim tunnel diode", *Applied Surface Science*, vol. 334, pp. 197–204, 2015.
- [105] P. Koppinen, "Bias and temperature dependence analysis of the tunneling current of normal metal-insulator-normal metal tunnel junctions", Master's thesis, Department of Physics, University of Jyväskylä, 2003.

- [106] M. Shanawani, D. Masotti, G. Paolini, F. Benassi, and A. Costanzo, "Efficient simulation method for wireless power transfer", in *IEEE-RFID-TA*, Accepted Paper, 2019.
- [107] N. Carvalho and A. Georgiadis, *Wireless Power Transmission for Sustainable Electronics: COST WiPE - IC1301*. Wiley, 2020, In print, ISBN: 9781119578543. [Online]. Available: https://books.google.it/books?id=_eAPvgEACAAJ.
- [108] D. Parker and D. C. Zimmermann, "Phased arrays-part ii: Implementations, applications, and future trends", *IEEE Transactions on Microwave Theory and Techniques*, vol. 50, no. 3, pp. 688–698, Mar. 2002. DOI: [10.1109/22.989954](https://doi.org/10.1109/22.989954).
- [109] M. Shanawani, D. Masotti, M. Aldrigo, F. Mastri, and A. Costanzo, "Millimeter wave agile transmitter for iot operations", in *Proc. IEEE Wireless Power Transfer Conf. (WPTC)*, Jun. 2018, pp. 1–4. DOI: [10.1109/WPT.2018.8639322](https://doi.org/10.1109/WPT.2018.8639322).
- [110] D. Masotti, P. Francia, A. Costanzo, and V. Rizzoli, "Rigorous Electromagnetic/Circuit-Level Analysis of Time-Modulated Linear Arrays", *IEEE Transactions on Antennas and Propagation*, vol. 61, no. 11, pp. 5465–5474, Nov. 2013. DOI: [10.1109/TAP.2013.2279217](https://doi.org/10.1109/TAP.2013.2279217).
- [111] V. Rizzoli, D. Masotti, F. Mastri, and E. Montanari, "System-oriented harmonic-balance algorithms for circuit-level simulation", *IEEE Transactions on Computer-Aided Design of Integrated Circuits and Systems*, vol. 30, no. 2, pp. 256–269, Feb. 2011. DOI: [10.1109/TCAD.2010.2092250](https://doi.org/10.1109/TCAD.2010.2092250).
- [112] D. Masotti, A. Costanzo, M. Del Prete, and V. Rizzoli, "Time-modulation of linear arrays for real-time reconfigurable wireless power transmission", *IEEE Transactions on Microwave Theory and Techniques*, vol. 64, no. 2, pp. 331–342, Feb. 2016. DOI: [10.1109/TMTT.2015.2512275](https://doi.org/10.1109/TMTT.2015.2512275).

- [113] H. J. Visser, "Rectenna realization: A practical step by step procedure", in *EuMW2017 workshop on Far-Field and Near-Field Techniques for Wireless Energy Transfer*, Presentation, 2017.
- [114] D. Brenner and Y. Wei. (Mar. 2018). "what can we do with 5g nr spectrum sharing that isn't possible today?", Qualcomm Technologies, Inc., [Online]. Available: <https://www.qualcomm.com/videos/webinar-what-can-we-do-5g-nr-spectrum-sharing-isnt-possible-today>.
- [115] C. A. Balanis, *Antenna theory, Analysis and design*, Description based upon print version of record, [s.l.], 2012.
- [116] L. Poli, P. Rocca, G. Oliveri, and A. Massa, "Harmonic beamforming in time-modulated linear arrays", *IEEE Transactions on Antennas and Propagation*, vol. 59, no. 7, pp. 2538–2545, 2011.
- [117] M. Del Prete, D. Masotti, N. Arbizzani, and A. Costanzo, "Remotely identify and detect by a compact reader with mono-pulse scanning capabilities", *IEEE Transactions on Microwave Theory and Techniques*, vol. 61, no. 1, pp. 641–650, 2013.
- [118] P. Rocca, D. Masotti, A. Costanzo, M. Salucci, and L. Poli, "The role of accurate dynamic analysis for evaluating time-modulated arrays performance", *IEEE Antennas and Wireless Propagation Letters*, vol. 16, pp. 2663–2666, 2017.
- [119] W. Wang, H. C. So, and A. Farina, "An overview on time/frequency modulated array processing", *IEEE Journal of Selected Topics in Signal Processing*, vol. 11, no. 2, pp. 228–246, Mar. 2017. DOI: [10.1109/JSTSP.2016.2627182](https://doi.org/10.1109/JSTSP.2016.2627182).
- [120] D. Masotti, M. Shanawani, and A. Costanzo, "Smart beamforming for energy-aware wireless power transmission", in *IEEE MTT-S*, 2019.

- [121] M. Fantuzzi, "Design and modelling of wireless power transfer and energy harvesting systems", PhD thesis, Electrical, Electronic, and Information Engineering Department, University of Bologna, 2018.
- [122] S. Hemour and K. Wu, "Radio-frequency rectifier for electromagnetic energy harvesting: Development path and future outlook", *Proceedings of the IEEE*, vol. 102, no. 11, pp. 1667–1691, Nov. 2014, ISSN: 1558-2256. DOI: [10.1109/JPROC.2014.2358691](https://doi.org/10.1109/JPROC.2014.2358691).
- [123] B. Ray, "What is lora? a technical breakdown", *Link Labs*, Jun. 2018, Online Article. [Online]. Available: <https://www.link-labs.com/blog/what-is-lora>.
- [124] , "SMS7630 Surface-Mount Mixer and Detector Schottky Diodes", Skyworks, Tech. Rep. 200041AD, Jun. 2018, Datasheet.
- [125] , "Lora network protocol and long range wireless iot", *Postscapes*, Oct. 2019, Online article. [Online]. Available: <https://www.postscapes.com/long-range-wireless-iot-protocol-lora/>.
- [126] D. M. Pozar, "Microwave engineering", *Wiley*, 2012.
- [127] G. Paolini, F. Benassi, M. Shanawani, D. Masotti, and A. Costanzo, "An em-based circuit model for loosely efficient rectennas", in *Proceedings of IMS 2020*, Submitted paper, 2020.
- [128] W. Ng, E. Lim, F. Bong, and B. Chung, "Folded patch antenna with tunable inductive slots and stubs for UHF tag design", *IEEE Transactions on Antennas and Propagation*, vol. 66, no. 6, pp. 2799–2806, Jun. 2018. DOI: [10.1109/TAP.2018.2821702](https://doi.org/10.1109/TAP.2018.2821702).
- [129] . (). Simsurfing online. Accessed 23/11/2019, Murata, [Online]. Available: <https://ds.murata.co.jp/simsurfing/mlcc.html?lcid=en-us>.

- [130] T. Weiland, "Time domain electromagnetic field computation with finite difference methods", *International Journal of Numerical Modelling: Electronic Networks, Devices and Fields*, vol. 9, no. 4, pp. 295–319, 1996.
- [131] V. Rizzoli, D. Masotti, N. Arbizzani, and A. Costanzo, "CAD procedure for predicting the energy received by wireless scavenging systems in the near- and far-field regions", in *2010 IEEE MTT-S International Microwave Symposium*, 2010, pp. 1768–1771. DOI: [10.1109/MWSYM.2010.5517916](https://doi.org/10.1109/MWSYM.2010.5517916).
- [132] CST. (Jan. 2018). Cst studio suite, [Online]. Available: <https://www.cst.com>.
- [133] A. Costanzo, A. Romani, D. Masotti, N. Arbizzani, and V. Rizzoli, "RF/baseband co-design of switching receivers for multiband microwave energy harvesting", *Sensors and Actuators A: Physical*, vol. 179, pp. 158–168, 2012, ISSN: 0924–4247. DOI: <https://doi.org/10.1016/j.sna.2012.02.005>. [Online]. Available: <http://www.sciencedirect.com/science/article/pii/S092442471200091X>.
- [134] H. Saghlatoon, L. Sydänheimo, L. Ukkonen, and M. Tentzeris, "Optimization of inkjet printing of patch antennas on low-cost fibrous substrates", *IEEE Antennas and Wireless Propagation Letters*, vol. 13, pp. 915–918, 2014, ISSN: 1536–1225. DOI: [10.1109/LAWP.2014.2322572](https://doi.org/10.1109/LAWP.2014.2322572).